

Ocean wave measurements using complex synthetic aperture radar data

Dissertation
zur Erlangung des Doktorgrades
der Naturwissenschaften im Fachbereich
Geowissenschaften
der Universität Hamburg

vorgelegt von

Johannes Schulz-Stellenfleth

aus

Hamburg

Hamburg 2003

Als Dissertation angenommen vom Fachbereich Geowissenschaften der Universität
Hamburg

aufgrund der Gutachten von

und

Hamburg, den

Professor Dr.

CONTENTS

1. <i>INTRODUCTION</i>	1
2. <i>OCEAN WAVES</i>	6
2.1 Linear wave theory	6
2.2 Statistical description of ocean waves	8
2.3 Parametric models	9
2.4 The numerical ocean wave model WAM	12
3. <i>SYNTHETIC APERTURE RADAR</i>	15
3.1 Imaging principle and data processing	15
3.1.1 Range processing	16
3.1.2 Azimuth processing	18
3.2 Multilooking	19
3.3 SAR cross spectra	21
3.3.1 Cross spectra estimation	22
3.3.2 SAR cross spectra coherence	24
3.4 Speckle noise	24
4. <i>SAR OCEAN WAVE IMAGING THEORY</i>	27
4.1 Backscattering model for the sea surface	28
4.1.1 Bragg scattering	28
4.1.2 Two-scale model	29
4.1.3 A nonlinear RAR model	31
4.2 Motion related SAR imaging mechanisms	33
4.2.1 Scanning distortion	33
4.2.2 Velocity bunching	33
4.3 Cross spectra integral transform	35
4.3.1 Integral transform derived by Engen & Johnson	36
4.3.2 New integral transform for high resolution SAR systems	38
4.3.3 Azimuthal cut-off	40
4.4 Linear inversion	40
5. <i>DESCRIPTION OF DATA</i>	43
5.1 ERS SAR data	43
5.1.1 ERS-2 SAR wave mode	44
5.1.2 ERS SAR full swath mode	47
5.2 Wave model data	48

6. <i>DISTRIBUTION OF THE ESTIMATED LOOK CROSS SPECTRUM</i> . . .	51
6.1 A statistical model for the estimated cross spectrum	52
6.2 A product model for the cross spectrum coherence	54
6.3 Dependence of coherence on the ocean wave spectrum	55
6.4 Optimal look separation time	58
6.5 Distribution of the cross spectrum real and imaginary part	59
7. <i>SAR OBSERVATIONS OF OCEAN WAVES TRAVELLING INTO SEA ICE</i>	61
7.1 Ocean wave attenuation by sea ice	62
7.2 SAR imaging of ocean waves in ice	64
7.2.1 Real aperture radar modulation in ice	65
7.2.2 Higher harmonics	66
7.2.3 Impact of sea ice on the orbital velocity variance	67
7.3 Azimuthal cut-off estimation	69
7.4 Case studies	71
7.4.1 Case study in the Weddell Sea	71
7.4.2 Case study in the Greenland Sea	76
7.5 A SAR ocean wave inversion scheme for the MIZ	78
8. <i>STATISTICAL ANALYSIS OF COMPLEX ERS-2 WAVE MODE DATA</i> .	83
8.1 Detection of inhomogeneous images	84
8.2 Comparison of linear SAR measurements with wave model output . .	87
8.3 Comparison of cross spectra phase with linear wave theory	90
9. <i>AN OCEAN WAVE RETRIEVAL SCHEME FOR SAR CROSS SPECTRA</i>	93
9.1 Retrieval strategy	95
9.2 Error models	96
9.2.1 Measurement errors	96
9.2.2 Uncertainties in the forward model	97
9.2.3 Statistical model for the ocean wave model spectrum	99
9.3 Numerical inversion procedure	102
9.3.1 Levenberg Marquardt Method	102
9.3.2 Termination Criteria	105
9.4 Test of retrieval using synthetic data	106
9.5 Application to reprocessed ERS-2 data	110
10. <i>SUMMARY AND CONCLUSIONS</i>	115
10.1 Theoretical investigations	115
10.2 Ocean wave damping by sea ice	116
10.3 Statistical analysis of complex imageries	117
10.4 PARSA wave retrieval scheme	117
11. <i>OUTLOOK</i>	119
12. <i>APPENDIX</i>	121
13. <i>DANKSAGUNG</i>	126

<i>Bibliography</i>	127
-------------------------------	-----

LIST OF FIGURES

2.1	Diagram showing significant wave height $H_s = \xi_{1/3}$ as a function of wind duration t_W , fetch distance x_f and wind speed U_{10} . T_{max} indicates the maximum wave period observed for fully developed wind seas (FDS) [Adapted from Van Dorn, W.G, Oceanography and Seamanship, 1974].	10
2.2	(A) Two-dimensional JONSWAP wavenumber spectrum (fully developed) with a \cos^2 directional distribution and 145 m peak wavelength. The unit of the isoline labels is m^4 . (B) JONSWAP frequency spectra with two peak frequencies $\omega_p = 0.95 \text{ s}^{-1}$ and $\omega_p = 0.65 \text{ s}^{-1}$ assuming fully developed sea state (dashed line) and developing sea state (solid line) respectively. The dashed curve for the lower peak frequency corresponds to the wavenumber spectrum shown in (A) in the case of deep water.	12
2.3	(Left) Map showing significant wave heights H_s computed with the WAM model for the Atlantic on May 27, 1997, 6:00 UTC (Right) Corresponding friction velocity u^* used as input for the model.	13
3.1	ERS-2 SAR imagette acquired at 54.86°S 55.48°W on Oct 6, 1996, 13:03 UTC. The corresponding complex data were processed with the DLR processor BSAR.	15
3.2	SAR imaging geometry in two dimensions (left) and three dimensions (right). In the standard reference system the SAR sensor is moving in the positive x -direction with velocity V , looking in the positive (left looking) or negative (right looking) y -direction. The left plot shows a squinted imaging geometry, i.e. the scatterer are not in the centre of the antenna beam at the time of closest approach (Doppler zero). . . .	16
3.3	(A) Azimuth spectrum with Doppler centroid frequency f_{dc} of the ERS-2 imagette shown in Fig. 3.1. (B) Azimuth spectrum with antenna weighting removed and filter functions used to extract looks, which are separated in time by 0.33 s.	19
3.4	(A,B) Two looks processed from the complex ERS-2 wave mode data. The looks are separated in time by 0.33 s, with the left look (A) followed by the right one. The corresponding single look intensity image is shown in Fig. 3.1. (C,D) Symmetric real part (C) and anti-symmetric imaginary part (D) of the corresponding look cross spectrum as defined in eq. 3.22, indicating a wave system of about 300 m wavelength propagating to the lower left. Dashed isolines indicate negative values.	20

3.5	(A) Shift of waves patterns taking place between look acquisition as a function of ocean wavelength assuming look separation times of $\Delta t = 0.33$ s and $\Delta t = 0.66$ s. The dashed line indicates the ERS-2 azimuth resolution for looks with half azimuth bandwidth. (B) The same as (A) for the cross spectrum phase.	22
3.6	(A) Two-dimensional wave spectrum computed with the WAM model collocated with the cross spectrum shown in Fig. 3.4. (B) Coherence estimate of the respective cross spectrum.	23
3.7	(A) Azimuth auto-correlation function of the intensity image shown in Fig. 3.1. (B) Respective cross-correlation function of two looks with non-overlapping frequency bands. The dashed lines are fitted Gaussian functions.	26
4.1	Illustration of the real aperture radar (RAR) tilt modulation mechanism. Due to the modulation of the local incidence angle by the long waves (longer than twice the resolution cell) the cross section pattern is shifted by 90° towards the radar with respect to the sea surface elevation.	28
4.2	Modulus (left) and absolute phase values (right) of theoretical RAR transfer function (compare eq. 4.5). A right looking SAR (looking in negative k_y direction) with VV polarisation and 23.5° incidence angle is assumed.	30
4.3	(A) Probability density functions of the normalised RAR image using the linear model eq. 4.4 (Gaussian curves) and the exponential model as given in eq. 4.10 for range resolutions of $\rho_r=25$ m (dashed curves) and $\rho_r=2$ m (solid curves). (B) Respective functional dependence of the RAR image on the zero mean process I^{RL} for the exponential model (solid and dashed curve) and the linear model (dashed dotted curve). (C) JONSWAP spectrum representing a fully developed wind sea with 200 m wavelength and 4.5 m significant wave height. (D) Percentage of negative RAR image points predicted by the linear model as a function of wavelength for fully developed wind seas assuming different range resolutions.	32
4.4	Illustration of the velocity bunching mechanism. Water particles performing a circular motion (compare Chapter 2) have a velocity component in slant range direction of the radar. The resulting Doppler shift leads to shifts of the corresponding image points in the azimuth direction.	34
4.5	Simulation of the SAR ocean wave imaging mechanism based on the nonlinear transform given by eq. 4.25 with wave spectrum (A) representing a fully developed wind sea of 200 m wavelength and 4.5 m wave height used as input, and resulting real part (C) and imaginary part (D) of the look cross spectrum. The imaging parameters of the ERS-2 SAR (compare table 5.1) were used for the simulation. The respective real part obtained with the quasi-linear model eq. 4.31 is shown in (B). Dashed isolines indicate negative values.	37

4.6	(A) Modulus of cross spectrum simulated with the transform eq. 4.25, which is based on the linear model for the RAR image, using the JON-SWAP spectrum shown in Fig. 4.3 (C) as input. (B) The same as (A), but using the modified integral transform eq. 4.33, which avoids the occurrence of negative NRCS values.	39
4.7	Theoretical cut-off wavelength λ_{cut} (compare eq. 4.46) depending on coherence time τ_s and orbital velocity variance $\rho^u(0)$. The dashed lines represent coherence times for different wind speeds as given in <i>Milman et al.</i> [1993] for C-band radar.	41
4.8	Illustration of the sign condition $F_k \geq 0$ to be taken into account in the linear cross spectra inversion. In case the measured cross spectrum lies outside the feasible regime the free solution for the wave spectrum \bar{F} (compare eq. 4.49) has negative energy values. A least square solution is then found by the projection of the observation onto the set of feasible cross spectra components. The transfer function \bar{T} is defined in eq. 4.51.	42
5.1	Imaging geometry of the ERS-2 SAR in wave mode and full swath mode.	43
5.2	Base band estimates of the Doppler centroid frequency f_{dc} for a global ERS-2 imagette data set acquired on June 1, 1997, reprocessed with the DLR BSAR processor.	45
5.3	Test of wave mode processing using an imagette acquired over land. The variance spectra in range and azimuth are shown in (A) and (B). The corresponding cross spectra phases are given in (C) and (D). The dashed lines indicate the expected phases for ocean waves (in deep water).	46
5.4	Cut in range (C) and azimuth (D) direction through the speckle variance spectrum of the homogeneous ERS-2 wave mode imagette (SLC) shown in (A) acquired over continental ice in Antarctica. The horizontal line represents the speckle noise level calculated according to eq. 3.40. The image shown in (B) was acquired over Australia.	48
5.5	(A) ERS-2 wave mode imagette (intensity) acquired on Sep 1, 1996 at 34.71°N, 22.92°W showing ocean waves. (B) Standard ERS-2 UWA spectrum computed from the imagette shown in (A). (C,D) Real part (C) and imaginary part (D) of the look cross spectrum computed from the respective complex imagette, which was processed with the DLR BSAR processor. The cross spectrum is shown on the polar grid, which is used for the standard ENVISAT wave mode product.	49
6.1	Diagram illustrating the relationship between the sea surface elevation field η , the SAR looks L^1, L^2 , the estimated cross spectrum $\hat{\Phi}$, the ocean wave spectrum F , the expected cross spectrum Φ , the coherence γ , and the SAR speckle noise.	51

6.2	(A) Standard deviation of the cross spectrum phase estimated by averaging $N=1,4,9,16$ complex samples. (B) The same as (A) for the normalised cross spectrum magnitude. (C,D) Theoretical signal to noise ratio of the cross spectrum phase as a function of wavelength for a coherence of $\gamma = 0.95$ (C) and $\gamma = 0.5$ (D). Deep water and a look separation time of $\Delta t = 0.33$ s is assumed.	52
6.3	(A) Dependence of the coherence γ^{SNR} on the signal to noise ratio (SNR) of the look variance spectrum SNR_k^{II} . (B) Coherence γ^{waves} in the case of standing waves as a function of wave period for two different look separation times.	54
6.4	(A) JONSWAP ocean wave spectrum representing a fully developed wind sea of 100 m length. (B) Simulated cross spectrum coherence γ^{waves} associated with the nonlinear SAR wave imaging mechanism.	55
6.5	Estimated coherence γ as a function of the signal to noise ratio of the look variance spectrum (compare eq. 6.17) derived from 1000 reprocessed ERS-2 wave mode images. The dashed line represents the expected look decorrelation γ^{SNR} associated with speckle noise (compare eq. 6.7).	56
6.6	(A) Azimuth cut through the peak of the coherence of the cross spectrum shown in Fig. 3.4 for look separation times of $\Delta t = 0.33$ s and $\Delta t = 0.45$ s. (B) The same as (A) for the imaginary part of the cross spectrum.	57
6.7	(A) Illustration of the parameter Δt in the look extraction process. (B) Theoretical signal to noise ratios of the cross spectrum phase as a function of look separation time for different signal to noise ratios in the look variance spectrum.	58
6.8	(A) Correlation of real and imaginary part of the cross spectrum as a function of coherence for expected cross spectrum phases of $\varphi_0 = 10^\circ$ and $\varphi_0 = 15^\circ$ (B) Expected deviation from the exact cross spectrum for $N = 1$ (no smoothing), $\gamma = 0.7$, and expected phase $\varphi_0 = 15^\circ$	60
7.1	Attenuation rates ρ_D of ocean waves damped by sea ice as reported in <i>Wadhams et al.</i> [1988] (compare eq. 7.1). The estimates were obtained under various ice conditions in the Greenland Sea and the Bering Sea.	63
7.2	The minimum wavelength λ_{ice} of wave components, which are able to propagate from the open water into the sea ice according to the mass-load-model (compare eq. 7.3). The ice cut-off wavelength is shown as a function of the product of ice thickness h and ice concentration c_I	65
7.3	Modulus of (normalised) tilt, range bunching and hydrodynamic modulation transfer functions. VV polarisation and 23° incidence angle are assumed. The tilt transfer function for ice was derived by extrapolating measurements reported in , 232 [3] <i>Vachon and Krogstad</i> [1994].	66
7.4	Simulated azimuthal SAR image auto-correlation function assuming a harmonic swell system of 400 m wavelength with 1.5 (solid line) and 3 m significant wave height (dashed line) propagating in the exact azimuth direction. The dashed dotted line results if an additional wind sea system (7 ms^{-1} wind speed) is assumed.	68

7.5	Orbital velocity variance $\rho^u(0)$ for a fully developed wind sea as a function of wind speed U_{10} and ice cut-off wavelength λ_{ice} . The dashed line indicates the peak wavelength for a given wind speed. The unit of the isoline labels is m^2s^{-2}	69
7.6	Orbital velocity variance $\rho^u(0)$ caused by swell as a function of wavelength and significant wave height H_s . The unit of the isoline labels is m^2s^{-2}	70
7.7	(A) Empirical cut-off wavelength λ_{3dB} measured according to eq. 7.13 versus theoretical cut-off wavelength defined by eq. 4.46. The plot is based on simulations using a global data set of 3000 ECMWF wave model spectra. (B) Resulting relationship between λ_{3dB} and the orbital velocity variance assuming coherence times τ_s of 0.03 s, 0.05 s and infinity. The error bars refer to the curve for $\tau_s = 0.05$ s.	71
7.8	(left) 5×10 km subimage of an ERS-2 SAR full swath scene acquired over the Weddell Sea on July, 18, 1992 at 12:41 UTC. The image is centred at 58.98° S 52.9° W with flight direction (205°) upwards. The bright region at the bottom is open water followed by two darker regions, which are covered by two different types of sea ice. (Right) Image spectra calculated for regions A,B and C (from bottom to top).	72
7.9	Simulation showing that refraction phenomena at the ice boundary observed on SAR images can be explained by imaging artefacts associated with the damping of short ocean waves. (A) Parameterised ocean wave spectrum (JONSWAP) representing a 150 m ocean wave system. (B) Schematic illustration of refraction mechanism (compare eq. 7.4). (C) Simulated SAR image spectrum in open water. (D) SAR image spectrum in sea ice, simulated by removing ocean wave components shorter than 80 m.	73
7.10	Azimuthal look cross-correlation functions calculated in regions A, B and C as indicated in Fig. 7.8.	74
7.11	100×130 km ERS-2 SAR scene acquired over the Greenland Sea on Feb 1, 1992, 23:32 UTC, showing the marginal ice zone. The image is centred at $66^\circ 45' 0''$ N, $28^\circ 47' 49''$ W. The bright region is open water, while the darker areas are covered with sea ice.	75
7.12	(Top) 5 km by 5 km subimages extracted from locations A,B,C indicated in Fig. 7.11. Grey values correspond to the SAR image modulation (compare eq. 3.36). (Bottom) Modulus of corresponding SAR cross spectra with identical scaling of grey values. The isolines are logarithmically spaced with 5 isolines per decade and labels given in m^2	76
7.13	One-dimensional SAR image variance wave number spectra for locations (A) (solid) and (C) (dashed) indicated in Fig. 7.11.	77
7.14	Azimuthal look cross-correlation functions with fitted Gaussians calculated from subimages shown in Fig. 7.12. Cut-Off wavelengths were estimated using the model given by eq. 7.13.	78

7.15	(A) Inverted ocean wave spectrum in open water. (B) Simulated SAR image spectrum in open water. (C) SAR image spectrum observed in open water. (D) Inverted ocean wave spectrum in sea ice. (E) Simulated SAR image spectrum in sea ice region. (F) SAR image spectrum observed in sea ice. (G) First guess ocean wave spectrum computed with the WAM model. (H) Comparison of simulated and observed cut-off in open water and sea ice. (I) Calculated Butterworth filter with $\gamma = 10$ and $\tilde{k} = 0.036 \text{ rad m}^{-1}$	79
8.1	(A) Boxes used to estimate the inhomogeneity parameter from wave mode imagettes. (B) Histogram of the inhomogeneity parameter estimated from a global data set of 30000 imagettes including land and sea ice.	84
8.2	(Top) Global map with inhomogeneity parameter ξ_H derived from ERS-2 wave mode imagettes acquired on Sep 5, 1996. (Bottom) Examples of ERS-2 imagettes, which failed the homogeneity test (i.e. $\xi_H > 1.05$) due to atmospheric and sea ice features as well as land structures.	85
8.3	(A) Scatterplot of the inhomogeneity parameter ξ_H versus ECMWF wind speeds. The horizontal line was used as a classification threshold. (B) Percentage of inhomogeneous imagettes as a function of ECMWF wind speed (solid line). The dashed line is the respective percentage of flagged ERS scatterometer measurements.	86
8.4	(A) Scatterplot of wave height H_{10}^{SAR} derived from SAR cross spectra using a linear inversion technique without prior information and respective wave height H_{10}^{WAM} calculated with the WAM model. (B) Scatterplot of the function W defined in eq. 8.6. The distance to the origin indicates the wave height H_{10}^{SAR} derived from SAR, whereas the direction gives the difference of the mean wave propagation directions as derived from SAR and WAM. The difference is zero for points on the positive part of the horizontal axis.	88
8.5	Global map showing mean propagation directions (red arrows) derived from complex ERS-2 wave mode imagettes acquired on Sep 5, 1996. The black arrows indicated the respective direction derived from collocated WAM model data. For the computation of the mean direction only waves with periods longer than 10 s were taken into account. The arrow length corresponds to the waveheight H_{10} defined in eq. 8.4.	89
8.6	(A) Distribution of cross spectrum energy as defined in eq. 8.7 derived from 1000 ERS-2 imagettes. (B) Respective average of the collocated ECMWF ocean wave spectra.	90
8.7	Distribution of cross spectrum energy in the wavenumber/phase plane for range travelling waves (A) and azimuth travelling waves (B) respectively (compare eq. 8.8 and eq. 8.9). The distribution was estimated from a global data set of 10000 cross spectra with a look separation time of $\Delta t = 0.33 \text{ s}$. The dashed curves represent the theoretical phase for ocean waves propagating in deep water (compare eq. 2.10).	91

9.1	Flowchart of the PARSA retrieval scheme	94
9.2	(A) Polar grid used in the PARSA retrieval scheme with 10° directional resolution and wavenumber spacing equivalent to the frequency grid used in the WAM model (for deep water). (B) Relevant spectral regimes in the frequency domain. The maximum frequencies in the WAM model and the PARSA scheme are denoted by f_{max}^{PARSA} and f_{max}^{WAM} respectively. For the computation of the orbital velocity variance $\rho^u(\mathbf{0})$ spectral energy above f_{max}^{PARSA} is taken into account.	96
9.3	(A) Average number N of cartesian grid points contained in the wavenumber bins used in the PARSA scheme (compare eq. 9.4). An image size of 10 by 5 km was assumed corresponding to the ERS wave mode. (B) Respective range of wavelength for each bin.	97
9.4	Transformations of wave systems used in the PARSA retrieval scheme (compare eq. 9.9). (A) Prior wave system with 250 m peak wavelength. (B-D) Transformed wave spectra with wavenumbers rescaled (B), directional spreading changed (C) and simultaneous rotation and energy rescaling (D).	100
9.5	Retrieval example using simulated data with prior spectrum F^{prior} (bottom right), observed cross spectrum Φ^{obs} (centre left), and retrieved wave spectrum F^{retr} . The cross spectra Φ^{prior} and Φ^{retr} simulated from the prior wave spectrum and the retrieved spectrum are shown one the lower left and upper left respectively. The spectrum F^{test} on the centre right was used to simulate the observed cross spectrum (for details see text).	108
9.6	Retrieval example using simulated data with prior spectrum F^{prior} (bottom right), observed cross spectrum Φ^{obs} (centre left), and retrieved wave spectrum F^{retr} . The cross spectra Φ^{prior} and Φ^{retr} simulated from the prior wave spectrum and the retrieved spectrum are shown one the lower left and upper left respectively. The spectrum F^{test} on the centre right was used to simulate the observed cross spectrum (for details see text).	109
9.7	PARSA retrieval for an ERS-2 cross spectrum acquired in the Indian Ocean at 23.46°S 64.36°E on Sep 5, 1996, 5:46 UTC. The satellite heading is 192.94° . The dashed vertical lines indicate the azimuthal cut-off wavelength as defined in Section 7.3.	110
9.8	PARSA retrieval for an ERS-2 cross spectrum acquired in the Pacific at 12.46°S 139.45°W on Sep 5, 1996, 8:06 UTC. The heading of the satellite is 347°	111
9.9	Comparison of significant wave height and mean direction of two-dimensional wave spectra computed with the WAM model (black) and respective PARSA retrievals (red) using ERS-2 cross spectra acquired on Sep 5, 1996.	112

-
- 9.10 Comparison of integral parameters of ocean wave spectra computed with the WAM model (horizontal axis) and respective PARSA retrievals (vertical axis). (A) Significant wave height. (B) Wave height for periods longer than 12 s. (C) Mean frequency. (D) Mean directions are given in the reference system of the sensor with range and azimuth directions corresponding to 90° and 0° respectively. 113

LIST OF TABLES

2.1	Classification of ocean wave systems in terms of the ratio of phase speed c_p and friction velocity u^* (wave age).	11
4.1	Coherence time τ_c for different wind speeds assuming C-band and 30° incidence angle (adapted from <i>Milman et al.</i> [1993])	29
5.1	General parameters of the ERS-2 SAR.	44
5.2	Periods of the reprocessed complex ERS-2 wave mode imagerettes available for the study.	44
5.3	Technical parameters of the ERS-2 SAR full swath mode and wave mode.	47
9.1	Standard deviations of the parameters α_1 , α_2 , ν_{RF} and ν_{IF} used to describe errors in the SAR ocean wave imaging model (compare eq. 9.5).	98
9.2	Standard deviations of the parameters used for the model describing errors in the prior wave spectrum (compare eq. 9.9).	101
12.1	List of symbols	123
12.2	List of symbols (continued)	124
12.3	List of acronyms	125

Chapter 1

INTRODUCTION

About 75 percent of our planet's surface is covered with water. The oceans play a central role in the global climate system and are an important factor in many economical fields.

The processes taking place in the oceans are driven by external forces such as the earth and moon gravity, the surface wind field or the solar radiation, and cover a wide range of spatial and temporal scales from several hundred years of the thermohaline circulation to periods in the order of milliseconds of acoustic waves. The understanding, the modelling and the forecast of these processes has taken a fast development, in particular with the advent of supercomputers, which allow numerical simulations with increasing resolution in time and space.

Due to the relatively small amount of in situ data available for the global oceans remote sensing techniques play an important role in oceanography. Although airborne and spaceborne sensors are restricted to measurement of geophysical variables of the sea surface, like sea surface temperature, sea surface elevation or surface currents, they help to understand processes like El Niño.

The present study is concerned with remote sensing of ocean surface gravity waves, which are the most visible manifestation of ocean dynamics on the fast time scale. Ocean waves play an obvious role for coastal regions, shipping and off-shore industry and also have an impact on global circulation processes, e.g. by conditioning the gas exchange between atmosphere and ocean. Another interesting aspect of ocean waves addressed in this study is their impact on sea ice, which is one of the key factors in the climate system.

Due to their stochastic nature, ocean waves (outside the strongly nonlinear near shore breaking zone) can be completely described by their two-dimensional variance spectra, which contain information on the distribution of the wavelengths, wave heights and propagation directions of different wave systems contributing to the variance of the sea surface elevation. Although it is in some cases sufficient to know integral parameters like significant wave height or mean period, interest is growing in detailed spectral information on sea state. This development is, e.g. driven by the increased understanding of the response of ships or off-shore platforms to waves, enabling improved designs by making use of the additional knowledge contained in two-dimensional wave spectra. Furthermore, numerical ocean wave models run at various weather centres, like the European Centre for Medium-Range Weather Forecast (ECMWF) have reached a level of accuracy where further improvements require the assimilation of detailed two-dimensional spectral information.

So far, the only remote sensing system capable of providing directional ocean

wave information on a global and continuous scale is the synthetic aperture radar (SAR). SAR is an active microwave radar with all-weather and daylight capability, which has amply demonstrated its large potential for land and ocean application, since the first spaceborne SAR aboard the SEASAT satellite was launched in 1978. Using sophisticated data acquisition and processing techniques, the current spaceborne SAR systems flown on the European satellites ERS-1, ERS-2 and ENVISAT or the Canadian satellite RADARSAT provide maps of the sea surface radar cross section with a resolution of about 20 m.

Conventional SAR measurements of ocean waves are based on the modulation of the radar cross section by different geometric and wave motion related mechanisms. Other techniques making use of additional phase information provided by multi-antenna SAR systems have been investigated [Bao *et al.*, 1997; Schulz-Stellenfleth and Lehner, 2001; Schulz-Stellenfleth *et al.*, 2001]. Although there is still debate about the appropriate modelling of some details of the SAR wave imaging process, like the so called hydrodynamic modulation, the overall mechanism is now well understood [Hasselmann *et al.*, 1985; Lyzenga, 1986; Alpers *et al.*, 1981].

Although SAR data contain more detailed information on the spatial structure of the wave field [Schulz-Stellenfleth and Lehner, 2003], the most common application is still the estimation of two-dimensional wave spectra. The retrieval of wave spectra from SAR data is a demanding problem, mainly because of the nonlinear coupling of different wave components in the mapping process. This effect causes the wave patterns on SAR images to appear distorted with respect to the underlying ocean wave field. Furthermore, SAR data lack information on the high frequency part of the ocean wave spectrum, i.e. some a priori information taken from wave models or other sensors is required to estimate a complete two-dimensional wave spectrum. This is in particular the case for shorter waves travelling in the sensor flight direction (azimuth), which are affected by the so called azimuthal cut-off.

Traditionally, SAR wave measurements were based on single intensity images, which provide a snapshot of the “frozen” sea surface. Using this approach, it is obvious that additional information is required to resolve the directional ambiguity of wave propagation. Several inversion schemes for the retrieval of two-dimensional wave spectra based on such data have been proposed, most of them using prior information from wave models [Hasselmann *et al.*, 1996; Mastenbroek and de Valk, 2000; Krogstad *et al.*, 1994].

A more recent method is based on the so called multi-look technique, where two images (looks) with a time separation of about one second are processed, making use of the special SAR imaging mechanism. Comparing the two looks by computing their cross spectrum yields information on the temporal evolution of the wave field, in particular on wave propagation directions [Engen and Johnson, 1995; Bao and Alpers, 1998]. The phase of the cross spectrum provides information about the shift of the harmonic waves contained in the wave field and the magnitude is related to wave energy.

The present study makes several contributions to the use of the multi-look technique for the measurement of ocean waves. The main points investigated are as follows:

- An analysis is presented of the first global data set of complex SAR data, which

were reprocessed from ERS-2 wave mode raw data.

- A noise model for look cross spectra is introduced, which enables an accurate assessment of the accuracy of the estimated cross spectrum phase.
- A modification of the existing integral transform for look cross spectra is proposed to exploit future high resolution systems like TerraSAR [*Mittermayer et al.*, 2002].
- Complex SAR data are used to study the damping of ocean waves in the marginal ice zone (MIZ).
- A parametric inversion scheme for the retrieval of two-dimensional ocean wave spectra from look cross spectra is introduced and applied to the global data set of ERS-2 cross spectra.

The cross spectra technique has been introduced about 10 years ago [*Vachon and Raney*, 1991], however up to now there were no data available to analyse the method on a statistical and global basis demonstrating its benefit, e.g. for wave model assimilation. In this study a new global data set of complex ERS-2 wave mode data is introduced [*Lehner et al.*, 2000], which allows such an investigation for the first time. The advantage of the new data compared to the ESA standard product is that multi-look techniques can be applied and furthermore the full image information is available. The study is meant to be a preparation for the data, which are currently becoming available from the new ENVISAT satellite launched in March 2002. Furthermore, it demonstrates the large amount of information contained in historical ERS data, which have not yet been fully exploited. The following points will be discussed in detail:

- What are the special processing requirements for complex SAR wave mode data ?
- Are the observed SAR cross spectra phases consistent with propagation directions found in numerical wave models ?
- Are the SAR cross spectra phases consistent with the theoretical phase speeds following from linear wave theory ?
- What is the benefit of the high resolution image information ?

The statistical analysis is complemented by a theoretical investigation [*Schulz-Stellenfleth et al.*, 2002] giving insight into the different factors determining the distribution of the estimated cross spectrum phase. The variance of the cross spectrum estimator is calculated depending on SAR system parameters and the underlying ocean wave field. The theory is applied to analyse the optimal choice of look separation and integration times.

Furthermore, a modification of the existing integral transform [*Engen and Johnson*, 1995] describing the mapping of a two-dimensional wave spectrum into the corresponding look cross spectrum is presented. The new transform is able to avoid meaningless values of the normalised radar cross section (NRCS), which can occur in

the old formulation. The problem is due to the commonly used linear model of the NRCS modulation, which has a probability of up to 10 % to predict negative radar cross sections at high sea states in the case of the ERS-2 configuration. It is shown that the performance of the linear model becomes intolerable if airborne sensors or future spaceborne systems like TerraSAR [Mittermayer *et al.*, 2002] with range resolutions of less than 2 m are used. The problem is solved using a nonlinear model for the NRCS, which is consistent with the linear formulation in so far as it maintains both the mean and variance of the NRCS. Simulations of SAR cross spectra showing the difference between the linear and nonlinear model are presented.

The benefit of lower noise levels in SAR cross spectra is demonstrated in a study of ocean waves travelling into sea ice [Schulz-Stellenfleth and Lehner, 2002]. Here, a special technique based on the multi-look technique, originally developed for wind speed estimation [Kerbaol *et al.*, 1998], is used to measure the damping of ocean waves by sea ice. The method is based on the strong correlation between the orbital velocity variance of the sea surface and the respective azimuthal cut-off wavelength, which can be estimated from the complex SAR image. It is shown that applying the technique to complex ERS-2 data acquired over the Greenland and the Weddell Sea yields damping parameters consistent with results obtained in earlier field campaigns. Furthermore, different typical effects found on SAR imagery acquired over the marginal ice zone (MIZ) like refraction of wave patterns at the ice boundary are shown to be caused by imaging artefacts. On the one hand this finding makes the interpretation of these data less straightforward, on the other hand the mechanism can be used to gain information about the damping of short waves by the ice. An approach to estimate the damping characteristic of the sea ice by simultaneous inversion of SAR image spectra in front and behind the ice boundary is proposed [Schulz-Stellenfleth and Lehner, 2002].

Finally, an inversion scheme for two-dimensional ocean wave spectra is introduced, which has ENVISAT-like cross spectra and prior information taken from a wave model as input. The scheme extends the basic retrieval method developed at the Max-Planck-Institute (MPI) [Hasselmann *et al.*, 1996; Hasselmann and Hasselmann, 1991], where the overall shape of the spectrum is taken from wave model data and the SAR information is used to correct different integral parameters like mean direction, mean wavelength and wave height of different wave systems. Compared to the MPI scheme the method has the following advanced features:

- The new phase information contained in look cross spectra is used to resolve ambiguities in the wave propagation direction.
- The directional spreading of different wave systems is introduced as an additional parameter.
- The scheme is based on explicit models for the measurement error, uncertainties in the SAR imaging model and errors in the prior wave spectrum, which allow a clear interpretation of the retrieval results in the framework of a maximum a posteriori approach.
- The inversion is performed on a polar grid with a dimension which is an order of magnitude lower than the cartesian grids used in Hasselmann *et al.* [1996].

This reduction enables the formulation of the retrieval as a straightforward minimisation problem with regard to the integral parameters, i.e. the second iteration loop with the sensitive cross assignment scheme as used in *Hasselmann et al.* [1996] is not required.

- The scheme provides an error covariance matrix of the retrieved parameters.

The scheme is applied to both simulated data and reprocessed ERS-2 wave mode cross spectra. In particular, the benefit of the additional phase information contained in cross spectra is demonstrated. Global maps comparing the inversion results with model output as well as scatter plots of integral parameters are presented.

The thesis is structured as follows: Chapter 2 gives an introduction to the physical background and the statistical treatment of ocean waves, including a brief description of the numerical wave model WAM used in the study. Chapter 3 summarises the basic concepts, capabilities and limitations of SAR. Special emphasise is put on the additional phase information contained in complex SAR data. The multi-look technique is described and look cross spectra are introduced. A well established model describing the ocean wave imaging process of a SAR is presented in Chapter 4. An extension of the model is proposed for application to high resolution SAR systems. Chapter 5 gives a description of the data used in the study. A noise model for look cross spectra acquired over the ocean is introduced in Chapter 6. The model enables the derivation of error bars for the estimated cross spectrum phase depending on SAR system parameters and the underlying ocean wave spectrum. Chapter 7 presents a study on ocean waves travelling into sea ice, while a statistical analysis of a reprocessed data set of complex ERS-2 imageries is given in Chapter 8. A new retrieval scheme for the estimation of two-dimensional ocean wave spectra from SAR cross spectra using wave model data as additional prior information is introduced in Chapter 9.

Chapter 2

OCEAN WAVES

In this chapter the basic elements of the theory of ocean surface gravity waves, which are needed for the subsequent investigation, are introduced.

The study of ocean waves and their dynamics has a long history [*Komen et al.*, 1994]. Along with the progress made in the field of fluid dynamics during the last two centuries, theories were developed for the propagation and generation of ocean waves. A big step in the understanding of surface gravity waves was the introduction of statistical concepts like, in particular the ocean wave spectrum. Taking the random nature of ocean waves into account models were developed for the generation, dissipation and interaction of waves. Milestones of this development were the studies on wave generation by *Phillips* [1957] and *Miles* [1957] and the theory on nonlinear wave interaction developed by *Hasselmann* [1962].

Several aspects of ocean wave dynamics like the generation of waves by wind or details of dissipation mechanisms like white capping are still subject of ongoing research [*Komen et al.*, 1994]

2.1 Linear wave theory

For the study of ocean surface gravity waves the ocean water is usually regarded as both incompressible and inviscid, i.e. viscous effects are neglected. Denoting the three-dimensional water velocity field with \mathbf{v} and pressure with p the water motion can be described by the Euler equation [*Phillips*, 1977]

$$\frac{\partial \mathbf{v}}{\partial t} + (\mathbf{v} \cdot \nabla) \mathbf{v} = \mathbf{f} - \frac{1}{\rho_W} \nabla p, \quad (2.1)$$

with ρ_W denoting the density of water. For surface gravity waves the Coriolis force and surface tension can be neglected to first order, so that the forcing term \mathbf{f} reduces to

$$\mathbf{f} = -\nabla(gz) \quad (2.2)$$

with gravitational acceleration g and z referring to the vertical axis. Assuming that wave amplitudes are small compared to wavelengths the quadratic term in the Euler equation can be neglected and the problem becomes linear. Furthermore, introducing a velocity potential $\Phi = -\nabla \cdot \mathbf{v}$ surface gravity waves in an infinite basin of water depth

h can be described by the following set of equations [Komen *et al.*, 1994]:

$$\Delta\Phi = 0 \quad (2.3)$$

$$g\zeta + \left(\frac{\partial\Phi}{\partial t}\right)_{z=\zeta} = 0 \quad (2.4)$$

$$\left(\frac{\partial\Phi}{\partial z}\right)_{z=\zeta} - \frac{\partial\zeta}{\partial t} = 0 \quad (2.5)$$

$$\left(\frac{\partial\Phi}{\partial z}\right)_{z=-h} = 0 \quad (2.6)$$

Here, ζ is the sea surface elevation with respect to the mean sea level. It can be shown [Phillips, 1977] that the fundamental solutions of these equations are given by plane harmonic waves, i.e.

$$\zeta_k(\mathbf{x}, t) = A \cos[\mathbf{k} \cdot \mathbf{x} - \omega t + \Phi_0] \quad (2.7)$$

with wave number vector \mathbf{k} , wave amplitude A , phase offset Φ_0 , and wave frequency ω , which obeys the dispersion relation given by

$$\omega^2(k) = g k \tanh(k h) . \quad (2.8)$$

If the water depth h is much larger than the wavelength, eq. 2.8 simplifies to the deep water dispersion relation

$$\omega^2(k) = g k . \quad (2.9)$$

The frequencies for which the above model is applicable typically range from about 0.05 Hz for long swell (600 m) to about 10 Hz for the shortest gravity waves in the centimetre regime (0.02 m).

Another important quantity is the phase speed c_p , which is given by

$$c_p(k) = \frac{\omega}{k} = \sqrt{\frac{g}{k} \tanh(k h)} . \quad (2.10)$$

The phase speed ranges from about 0.2 ms^{-1} for the shortest waves (0.02 m) to about 30 ms^{-1} for longer swell (600 m). The fact that longer waves propagate faster than shorter waves is easy to verify observing waves generated by ships at shore, where the longest waves arrive first. The group speed c_g , which describes the propagation of energy is half the phase speed.

Furthermore, it can be shown [Apel, 1995], that within the above linear theory individual water particles move on circles with radius r given by

$$r = A \exp(-k z) , \quad (2.11)$$

if deep water is assumed. Here, z denotes the vertical position of the circle centre. This simple behaviour allows a relatively straightforward description of the impact of wave motion on the SAR imaging process as described in Chapter 4. However, one should be aware that in the case of nonlinear waves or in shallow water the trajectories of individual water particles can deviate strongly from circles [Apel, 1995].

2.2 Statistical description of ocean waves

The solution of the Euler equation (eq. 2.1) requires exact knowledge about the boundary conditions, like bathymetry, and the initial state including the phases of the different ocean wave components. As such information is in general not available, the ocean surface elevation ζ is usually taken as a random process. This means that the ocean surface field is defined by a probability density function (pdf) with

$$\text{pdf}(\zeta_1, \dots, \zeta_m) d\zeta_1 \dots d\zeta_m \quad (2.12)$$

giving the probability that the surface elevations ζ_1, \dots, ζ_m measured at locations x_1, \dots, x_m lie within the intervals $[\zeta_1, \zeta_1 + d\zeta_1], \dots, [\zeta_m, \zeta_m + d\zeta_m]$. For a time period and a region small enough to assume constant boundary conditions the process is both stationary and homogenous, i.e. the statistical moments are shift invariant in both time and space.

According to the definition of the sea surface elevation, i.e. using the mean sea level as reference, the first moment of ζ is given by:

$$\langle \zeta(\mathbf{x}, t) \rangle = 0. \quad (2.13)$$

The second order statistics of the wave field is commonly described in the spectral domain. Let ζ have a Fourier representation given by

$$\zeta(\mathbf{x}, t) = 2 \text{Re} \left(\sum_{\mathbf{k}} \zeta_{\mathbf{k}} \exp[i(\mathbf{k} \cdot \mathbf{x} - \omega t)] \right), \quad (2.14)$$

where Re denotes the real part. For the second moments of ζ it is straightforward to show [Komen *et al.*, 1994] that from stationarity and homogeneity it follows that the auto-covariance function has the following form

$$\rho_{\zeta}(\mathbf{x}, t) = \langle \zeta(\mathbf{x}, t) \zeta(\mathbf{0}, 0) \rangle = \text{Re} \left(\sum_{\mathbf{k}} F_{\mathbf{k}} \exp[i(\mathbf{k} \cdot \mathbf{x} - \omega t)] \right), \quad (2.15)$$

with the ocean wave spectrum $F_{\mathbf{k}}$ defined as

$$F_{\mathbf{k}} d\mathbf{k} = 2 \langle |\zeta_{\mathbf{k}}|^2 \rangle \quad (2.16)$$

and $d\mathbf{k}$ denoting the spectral binsize associated with the finite size of the ocean wave field considered. This means $F_{\mathbf{k}}$ can be interpreted as the contribution of the different wave components to the variance of the surface elevation ζ .

It can be shown that within the linear theory the assumption of stationarity and homogeneity necessarily leads to a Gaussian wave field [Hasselmann, 1968]. The ocean wave spectrum $F_{\mathbf{k}}$ thus gives a complete statistical description of the ocean wave field in the linear approximation.

The sea state can be characterised by different integral parameters like, e.g. significant wave height H_s defined as follows:

$$H_s = 4 \sqrt{\text{var}(\zeta)} = 4 \sqrt{\int F_{\mathbf{k}} d\mathbf{k}} \quad (2.17)$$

Assuming a narrow wave spectrum F it can be shown that wave crest, i.e. local maxima of the elevation ζ , are approximately Rayleigh distributed [Phillips, 1977]. In this case the significant wave height can be interpreted as the average of the 30% highest wave crests. H_s roughly corresponds to the “average” wave height obtained via visual observation.

Most people concerned with practical problems, e.g. in ocean engineering, are used to directional frequency spectra $F_{f,\Phi}$, which are related to the wavenumber spectrum $F_{\mathbf{k}}$ via

$$F_{f,\Phi} = \frac{32 \pi^4 f^3}{g^2} F_{\mathbf{k}} , \quad (2.18)$$

with $\mathbf{k} = k (\cos \Phi, \sin \Phi)$, and $\omega = 2 \pi f$ connected to k via eq. 2.8. Based on $F_{\omega,\Phi}$ different parameters characterising the sea state like, e.g. peak frequency ω_p or peak direction Φ_p are defined. The one-dimensional frequency spectrum often used in practice is computed from $F_{f,\Phi}$ as

$$F_f = \int_0^{2\pi} F_{f,\Phi} d\Phi . \quad (2.19)$$

The importance of this spectrum lies in the fact that it has been measured by different traditional instruments like, e.g. buoys, for a long time, i.e. a lot of data exist and extensive analysis has been performed.

2.3 Parametric models

For larger areas and longer time periods the wave spectrum $F_{\mathbf{k}}$ changes due to wind forcing, dissipation and interactions between different wave components. When the wind starts to blow over calm water, short waves in the centimetre regime are generated. As time goes on the peak wavelength increases due to nonlinear interactions. Assuming that the wind is constant over a long time and a long distance (fetch) the wave spectrum finally reaches an equilibrium state (fully developed wind sea). This state is characterised by a peak frequency corresponding to phase speeds in the order of the wind speed near the sea surface and a typical shape of the high frequency tail of the spectrum. Fig. 2.1 gives a rough overview of wave height and wave period as a function of wind speed U_{10} , wind duration t_W and fetch distance x_f .

A simple rule of thumb for the peak wavenumber k_p and the wave height of fully developed wind seas is given by the following formulas [Alpers, 1983]:

$$\begin{aligned} k_p &= 0.697 \frac{g}{U_{10}^2} \\ H_s &= 0.24 \frac{U_{10}^2}{g} \end{aligned} \quad (2.20)$$

For instance a wind speed of 10 ms^{-1} at 10 m height results in about 2.5 m wave height and about 100 m peak wavelength.

Due to their high phase speeds the longer wave components of the wind generated wave systems leave the area of generation as so called swell and propagate along great circles over the ocean. In the case of strong storm events, swell can be observed even

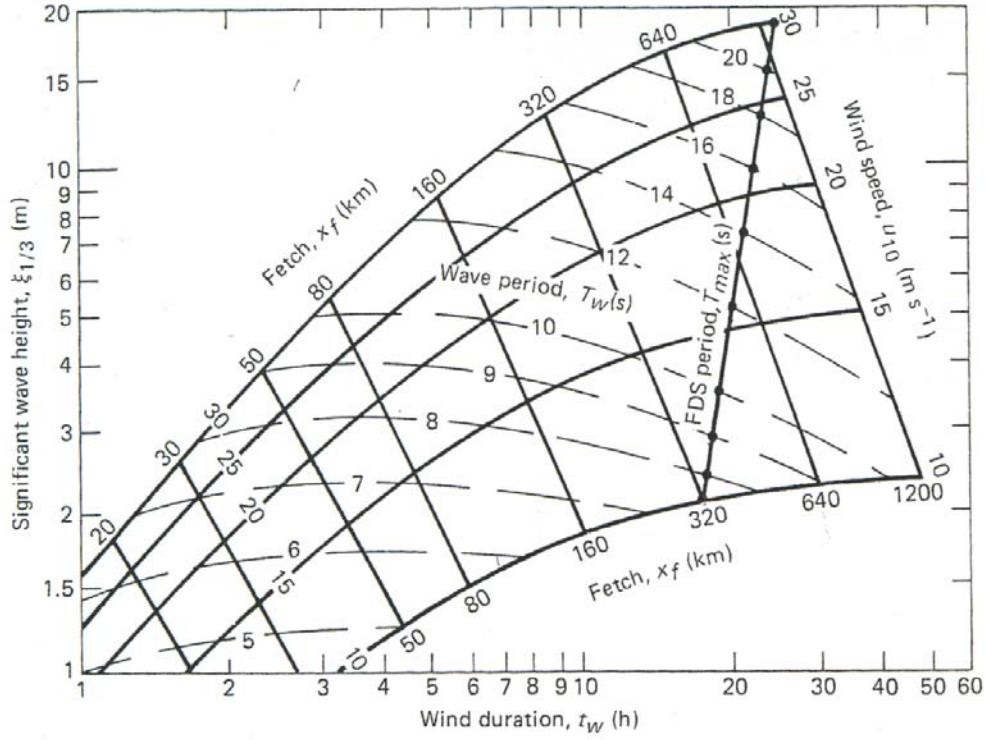


Fig. 2.1: Diagram showing significant wave height $H_s = \xi_{1/3}$ as a function of wind duration t_W , fetch distance x_f and wind speed U_{10} . T_{max} indicates the maximum wave period observed for fully developed wind seas (FDS) [Adapted from Van Dorn, W.G, Oceanography and Seamanship, 1974].

several thousand kilometres from the generating area, before it is finally damped out by dissipation effects.

A classification of different wind sea and swell systems is usually done in terms of the ratio of the wave phase speed c_p and the friction velocity u^* . The friction velocity is related to U_{10} via

$$U_{10} = \frac{u^*}{\kappa} \log \left[\frac{10 g}{\alpha_{ch} (u^*)^2} \right] \quad (2.21)$$

with Charnock constant $\alpha_{ch} = 0.0185$ and $\kappa = 0.41$ the Karman constant [Komen *et al.*, 1994]. An overview of the different wave system types is given in table 2.1.

As suggested by Fig. 2.1 the generation of waves by the wind field is a complex mechanism, which is in fact still the subject of ongoing research [Mastenbroek, 1996]. The exact shape of the wind sea spectrum depends on the fetch as well as the duration of the wind impact. An empirical model for the wind sea spectrum was derived from data acquired during the JONSWAP experiment [Hasselmann, 1973] and is given by the following expression for the one dimensional frequency wave spectrum:

$$F(\omega) = \alpha g^2 \omega^{-5} \exp \left[-\frac{5}{4} \frac{\omega^{-4}}{\omega_p^{-4}} + \log \gamma_p \exp \left[-\frac{(\omega - \omega_p)^2}{2 \sigma_j^2 \omega_p^2} \right] \right] \quad (2.22)$$

Classification	c_p/u^*
young windsea	$\leq 10-20$
old windsea	$\approx 20-30$
fully developed	$\approx 30-40$
swell	$\geq 30-40$

Tab. 2.1: Classification of ocean wave systems in terms of the ratio of phase speed c_p and friction velocity u^* (wave age).

Here, α is a dimensionless parameter describing the energy level, ω_p is the peak frequency, γ_p is the peak enhancement parameter and σ_j defined as

$$\sigma_j = \begin{cases} 0.09 & \text{if } \omega \leq \omega_p \\ 0.07 & \text{if } \omega \geq \omega_p \end{cases} \quad (2.23)$$

determines the width of the spectrum. For a fully developed wind sea one has

$$\alpha = 0.0081 \quad \gamma_p = 1 \quad (2.24)$$

and eq. 2.22 is also referred to as Pierson-Moskowitz spectrum. For a growing wind sea the parameters were chosen as

$$\alpha = 0.01 \quad \gamma_p = 3.3 \quad (2.25)$$

in accordance with *Brüning et al.* [1990]. Fig. 2.2 (B) shows frequency spectra for fully developed (dashed lines) and growing wind seas (solid lines) for two peak frequencies. One can see that growing wind seas are characterised by a more peaked appearance than fully developed seas, which is due to nonlinear interactions between different wave components [*Hasselmann*, 1973]. The high frequency tail of the JONSWAP spectrum shows a ω^{-5} decay, which is associated with wave breaking and cusp-like crests. However, there is still some debate about the exact power law suitable to describe these processes [*Phillips*, 1985].

Following *Brüning et al.* [1990] to describe the directional spreading, the following expression is derived from eq. 2.22 for the two-dimensional JONSWAP wavenumber spectrum:

$$F_{\mathbf{k}} = \frac{\alpha}{\pi} k^{-4} \exp \left[-\frac{5}{4} \frac{k^{-2}}{k_p^{-2}} + \log \gamma_p \exp \left[-\frac{(\sqrt{k} - \sqrt{k_p})^2}{2\sigma_j^2 k_p} \right] \right] \cos^{2p}(\Phi - \Phi_p) N(p) \quad (2.26)$$

Here, the wavenumber dependent spreading factor p is given by

$$p = \begin{cases} 0.46 (k/k_p)^{-1.25} p_m & \text{if } k \geq k_p \\ 0.46 (k/k_p)^{2.5} p_m & \text{if } k < k_p \end{cases} \quad (2.27)$$

with p_m defined as

$$p_m = 8.7 \left(\frac{U_{10}}{\sqrt{g/k_p}} \right)^{-2.5} \quad (2.28)$$

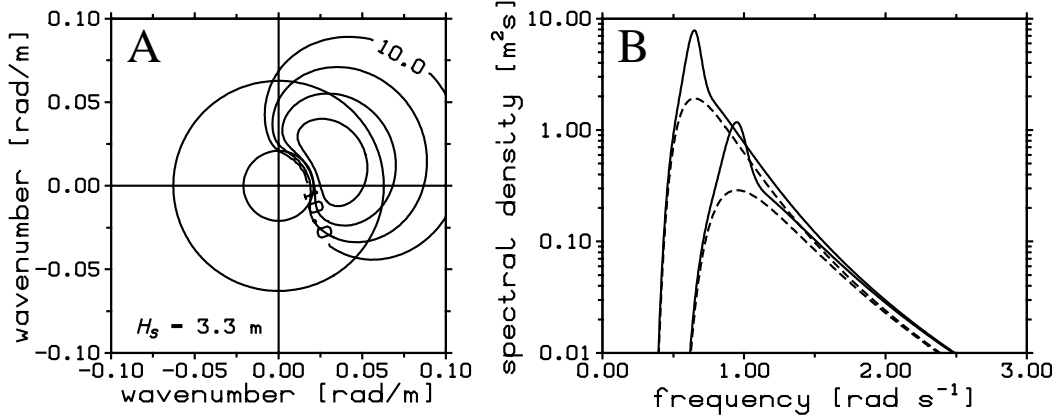


Fig. 2.2: (A) Two-dimensional JONSWAP wavenumber spectrum (fully developed) with a \cos^2 directional distribution and 145 m peak wavelength. The unit of the isoline labels is m^4 . (B) JONSWAP frequency spectra with two peak frequencies $\omega_p = 0.95 \text{ s}^{-1}$ and $\omega_p = 0.65 \text{ s}^{-1}$ assuming fully developed sea state (dashed line) and developing sea state (solid line) respectively. The dashed curve for the lower peak frequency corresponds to the wavenumber spectrum shown in (A) in the case of deep water.

and normalisation factor $N(p)$ given by:

$$N(p) = \frac{1}{\sqrt{\pi}} \frac{\Gamma(1 + p/2)}{\Gamma(1/2 + p/2)} \quad (2.29)$$

The model represents a single wave system with peak wavenumber $k_p = |\mathbf{k}_p|$ and propagation direction $\Phi_p = \text{atan}(k_y, k_x)$. The high wavenumber part of the spectrum is dominated by a k^{-4} decay. One should note that there is still a lot of debate about a suitable model for the directional spreading. In fact this is the reason why the directional spreading is introduced as an additional parameter in the inversion scheme presented in Chapter 9. Because of the uncertainty we will also use a simpler \cos^2 model, without frequency dependence in some of the simulations presented in this study. A contour-plot of a two-dimensional spectrum representing a fully developed wind sea with a \cos^2 distribution is shown in Fig. 2.2 (A).

2.4 The numerical ocean wave model WAM

Ocean wave models like WAM [WAMDI Group, 1988] describe the temporal and spatial evolution of the two-dimensional ocean wave spectrum. The driving near-surface wind field as well as the the bottom topography is needed as input. Such numerical models are used operationally at different metereological institutes like the ECMWF and are capable of giving ocean wave forecasts typically on a time scale of a few days.

In this thesis the ocean wave model WAM is used to compute ocean wave hindcasts. WAM is a third generation model based on a closed theory for the generation and propagation of ocean waves. The model is expressed in terms of a partial differential equation (action balance equation), which in a simplified form (assuming no

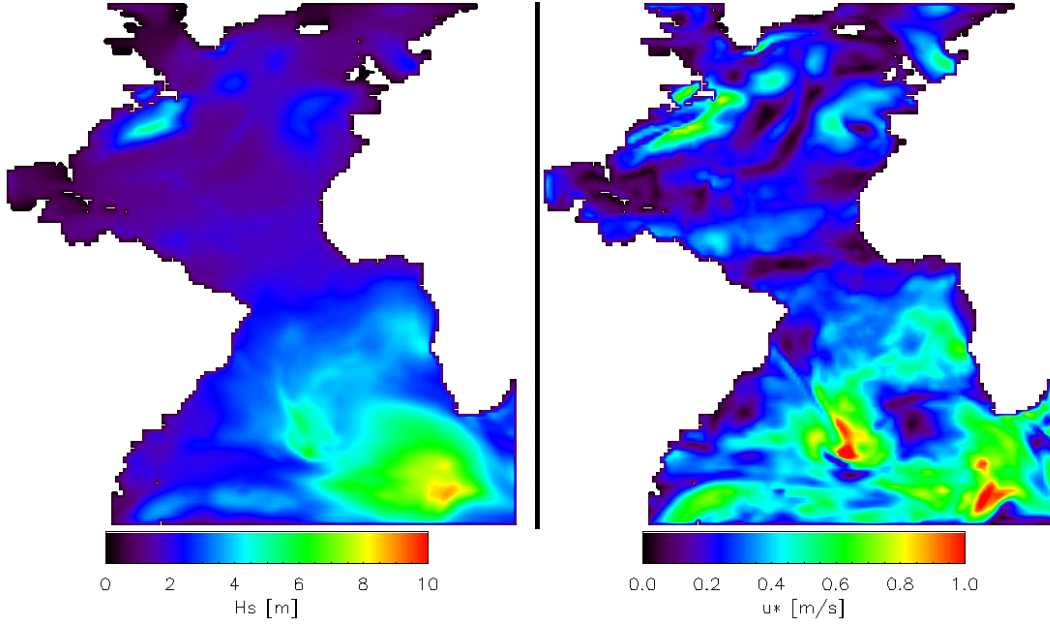


Fig. 2.3: (Left) Map showing significant wave heights H_s computed with the WAM model for the Atlantic on May 27, 1997, 6:00 UTC (Right) Corresponding friction velocity u^* used as input for the model.

currents and infinite water depth) is given by the following expression :

$$\left(\frac{\partial}{\partial t} + c_g \cdot \frac{\partial}{\partial \mathbf{x}} \right) F(\mathbf{k}, \mathbf{x}, t) = S_{\text{in}} + S_{\text{nl}} + S_{\text{ds}} \quad (2.30)$$

The action balance equation describes the development of an ocean wave spectrum F with time t at different locations \mathbf{x} . The term S_{in} represents the energy input of the wind; S_{nl} describes nonlinear interactions between different wave components [Hasselmann, 1962] and S_{ds} introduces dissipation effects [Komen *et al.*, 1994].

Fig. 2.3 shows an example of a WAM run computed for the Atlantic Ocean set up on a 1° grid using ECMWF wind fields as input. Both the significant wave height and friction velocity for May 27, 1997 are shown. The model was run with 20 min time steps and three days spin up time. Wind fields are available every 6 hours and are interpolated in between. One can see different low pressure systems mainly in the south east and north west Atlantic with wind speeds (in 10 m height) of up to 20 ms^{-1} . The sea states generated by the respective wind fields have significant wave heights of up to 10 m.

Chapter 3

SYNTHETIC APERTURE RADAR

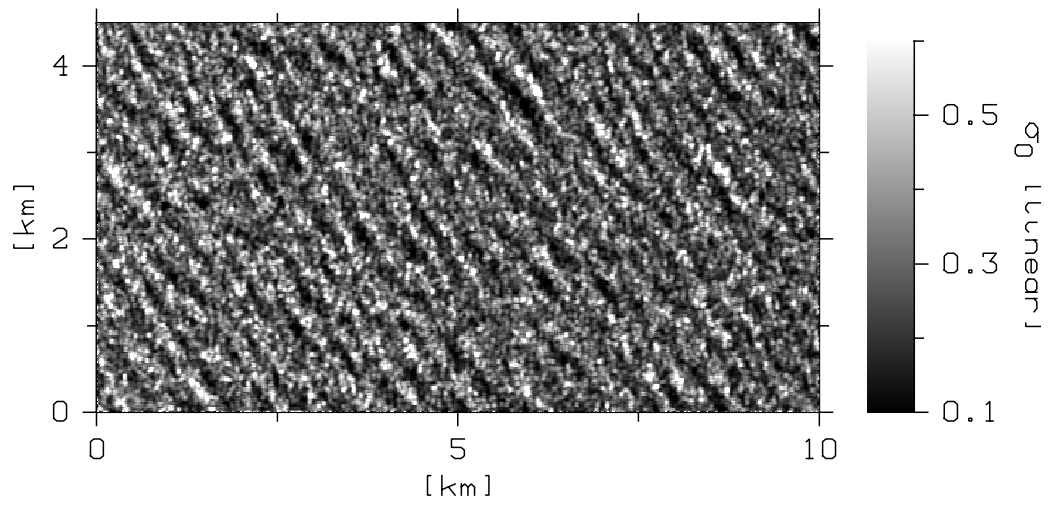


Fig. 3.1: ERS-2 SAR imagette acquired at 54.86°S 55.48°W on Oct 6, 1996, 13:03 UTC. The corresponding complex data were processed with the DLR processor BSAR.

In this chapter the basic SAR imaging mechanism and the main SAR processing steps are explained. Furthermore, the so called multi-look technique is described, including an introduction to look cross spectra. Finally, some basic properties of SAR speckle noise are summarised. The techniques and concepts introduced provide the basis for the understanding of the different aspects of SAR ocean wave imaging discussed in the subsequent chapters.

3.1 Imaging principle and data processing

Synthetic aperture radar is an active remote sensing system, which provides two-dimensional maps of the normalised radar cross section (NRCS), denoted by σ_0 . As an example Fig 3.1 shows a SAR intensity image of 10 by 5 km size acquired over the South Indian Ocean by the SAR onboard the ERS-2 satellite. Ocean wave patterns are clearly visible. A detailed discussion of the exact relationship between the image wave patterns and the underlying moving ocean wave field is given in Chapter 4.

The NRCS is a measure for the ability of a surface to reflect radar signals. It is defined as the normalised energy flux scattered by a unit area of the surface into a

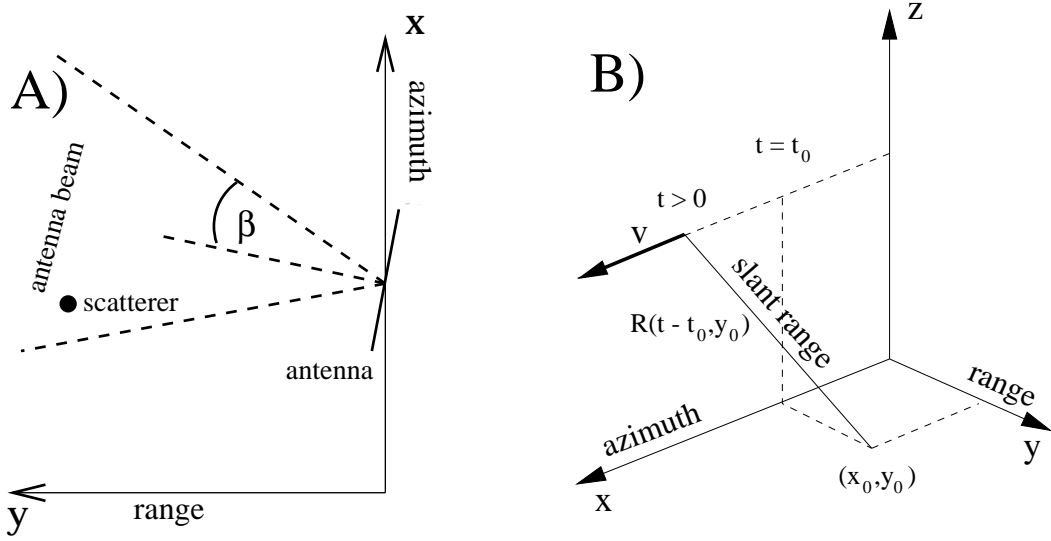


Fig. 3.2: SAR imaging geometry in two dimensions (left) and three dimensions (right). In the standard reference system the SAR sensor is moving in the positive x -direction with velocity V , looking in the positive (left looking) or negative (right looking) y -direction. The left plot shows a squinted imaging geometry, i.e. the scatterer are not in the centre of the antenna beam at the time of closest approach (Doppler zero).

given direction observed at large distances. The normalisation is done by dividing by the incident power. The NRCS is a dimensionless variable denoted by σ_0 , which is usually given in dB values [Fung, 1994]. In the case of surface waves the radar return for the system configurations considered here is dominated by Bragg scattering. A model for the normalised radar cross section of the sea surface, which depends on the wave spectrum, will be introduced in Section 4.1.

The basic object imaged by a SAR is the complex reflectivity r , which has a magnitude related to the NRCS by

$$\sigma_0 = \langle |r|^2 \rangle \quad (3.1)$$

and a phase which accounts for possible phase shifts taking place in the scattering process. As the phase of r is very sensitive to the detailed geometry of the local scattering process, r is usually taken as a random circular Gaussian process with second moments related to the NRCS via eq. 3.1, where the angle brackets can be interpreted as an average over a resolution cell.

Making use of the platform motion, airborne or spaceborne SAR systems achieve a high resolution both in flight (azimuth) and across flight (range) direction (compare Fig. 3.2). As the imaging processes in the two dimensions are governed by different time scales, they can in a first approximation be treated as independent [Bamler and Schättler, 1993].

3.1.1 Range processing

As known from conventional real aperture radar (RAR), the SAR imaging mechanism in the range dimension is based on the measurement of the time return echo of the

transmitted signal [Curlander, 1991]. Most SAR systems transmit chirp signals of the form

$$p^t(t) = \exp[i(\omega_0 t - \beta_f t^2)] \quad |t| \leq \tau_p/2 \quad (3.2)$$

with carrier frequency ω_0 , frequency modulation rate β_f , and signal duration time τ_p . The bandwidth B_r of such signals is given by

$$B_r = \frac{\beta_f \tau_p}{\pi} . \quad (3.3)$$

In the case of the ERS SAR the chirp duration is $4 \cdot 10^{-5}$ s and the range bandwidth is $B_r = 15.5$ MHz.

The standard reference system for SAR imaging models is a right handed coordinate system with the SAR flying in positive x direction with velocity V (compare Fig. 3.2). The location of a point scatterer on the surface is given by its distance to the radar R_0 at the time t_0 of the closest approach (Doppler zero) and either t_0 or the corresponding spatial azimuth coordinate $x_0 = t_0 V$. The received signal returned from a point scatterer with slant range distance $R(t)$ from the radar at time t is given by

$$p^r(t) = C(R) r(x_0, t - \frac{R(t)}{c_L}) p^t(t - \frac{2R(t)}{c_L}) \exp[-2i k_E R(t)] , \quad (3.4)$$

where c_L is the speed of light and k_E is the radar wavenumber. The real factor $C(R)$ accounts for signal power lost on the round trip path [Bamler and Schättler, 1993]. Here, the so called start stop approximation is used, which neglects the very small change of the range distance R between transmission and reception. The returned signal is processed by first removing the carrier frequency ω_0 and subsequent cross correlation with a replica chirp. As it can be assumed that r is constant for the duration of a range chirp this yields an impulse response h_r given by [Oliver and Quegan, 1998; Bamler and Schättler, 1993]:

$$\begin{aligned} h_r\left(t - \frac{2R(t)}{c_L}\right) &= r(x_0, t) \int_{\tau_p/2}^{\tau_p/2} \exp(i\beta_f t'^2) \exp(-i\beta(t' + t)^2) \text{rect}\left(\frac{t' + t}{\tau_p}\right) dt' \\ &\approx r(x_0, t) \tau_p \exp[-2i k_E R(t)] \text{sinc}(B_r t) \end{aligned} \quad (3.5)$$

The last approximation holds near the peak $|t| \ll \tau_p$ of h_r for large time-bandwidth products $B_r \tau_p \gg 1$, which are used for common SAR systems like the ERS SAR with $B_r \tau_p = 575.05$. The range resolution can be defined as the 3dB width of the impulse response function h_r and is given by

$$\rho_{sr} = 0.885 \cdot \frac{c_L}{2 B_r} \quad (3.6)$$

using the approximation in eq. 3.5. For the ERS SAR the slant range resolution is about 8 m. The corresponding ground range resolution ρ_{gr} is dependent on the incidence angle θ and is given by [Curlander, 1991]

$$\rho_{gr} = \frac{\rho_{sr}}{\sin \theta} , \quad (3.7)$$

assuming an idealised flat surface. The ground range resolution of the ERS SAR in mid swath is about 20 m.

3.1.2 Azimuth processing

The azimuth resolution for a conventional real aperture radar is given by the width of the antenna beam β_A , which in turn depends on the radar wavelength λ_E and the antenna length L . The 3dB width β_A^{3dB} of the antenna beam is given by [Bamler and Schättler, 1993]:

$$\beta_A^{3dB} = 0.64 \frac{\lambda}{L} \quad (3.8)$$

For the ERS SAR this yields an antenna footprint on the earth surface of about 4 km length in azimuth. Scatterers with slant range distance R_0 are thus illuminated by the radar for an integration time T_0^{3dB} given by (compare eq. 3.8):

$$T_0^{3dB} = 0.64 \frac{\lambda R_0}{V L} \quad (3.9)$$

For the ERS-2 SAR the integration time defined in this way is about 0.46 s. Note that the processed ERS-2 integration time available for the techniques applied in this thesis is about 0.66 s and thus slightly longer than T_0^{3dB} .

The high resolution in flight direction achieved by a SAR is based on the phase history of the signals returned from each scatterer as the radar passes by (compare eq. 3.5). Assuming that the range processing has already been performed the raw data signal returned from the point scatterer received by the SAR at time t is given by

$$s(t) = C(R_0) r(x_0, t) G(t_0, x_0) \exp[-2 i k_E R(x_0, t)] \quad , \quad (3.10)$$

with antenna pattern G . A simple model for G is given by [Alpers *et al.*, 1981]:

$$G(t, t_0) = \exp\left[-2 \frac{(t_0 - t)^2}{T_0^2}\right] \quad (3.11)$$

Similar to the range compression step the azimuth processing is done by correlation with a replica chirp. Assuming that the complex reflectivity r remains unchanged during integration time and further using a quadratic approximation for the range distance, i.e.

$$R(x_0, y_0, t) \approx R_0 + \frac{V^2 (t - t_0)^2}{2 R_0} \quad , \quad (3.12)$$

the complex SAR image c is given by

$$\begin{aligned} c(t = \frac{x}{V}) &= \int s(t') \exp\left[i k_E \frac{V^2 (t' - t)^2}{R_0}\right] dt' \\ &= C(R_0) r(x_0) \exp\left[-i k_E \left(2 R_0 - \frac{(x - x_0)^2}{R_0}\right)\right] \\ &\quad \cdot \exp\left[-\frac{k_E^2 V^2 T_0^2 (x - x_0)^2}{2 R_0^2}\right] . \end{aligned} \quad (3.13)$$

The impulse response is centred at $t_0 = x_0 V^{-1}$ with phase at the peak given by $\text{Arg}(r(x_0)) - 2 k_E R_0$. The phase of the complex SAR image thus contains information on the slant range R_0 on a centimetre scale. This fact is the basis for so called SAR interferometry, where pairs of complex SAR images are used to obtain information

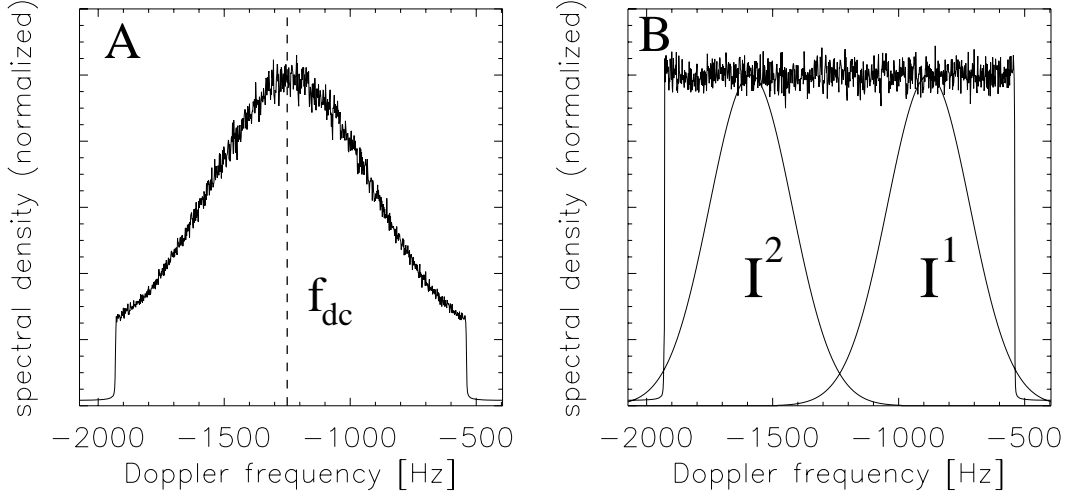


Fig. 3.3: (A) Azimuth spectrum with Doppler centroid frequency f_{dc} of the ERS-2 imagette shown in Fig. 3.1. (B) Azimuth spectrum with antenna weighting removed and filter functions used to extract looks, which are separated in time by 0.33 s.

on digital elevation models of terrain [Bamler and Hartl, 1998], ocean waves [Schulz-Stellenfleth et al., 1998; Schulz-Stellenfleth and Lehner, 2001; Bao et al., 1997], and currents [Romeiser and Thompson, 2000].

The intensity image I_σ of the point scatterer is given by:

$$I_\sigma = \langle |c(t)|^2 \rangle = C^2(R_0) \sigma_0(x_0) \exp\left[-\frac{k_E^2 V^4 T_0^2 (t - t_0)^2}{R_0^2}\right] \quad (3.14)$$

Here, the angle brackets indicate an ensemble average over different realisations of the r process. The spatial azimuth resolution ρ_{az} of the intensity image is given by the 3dB width of the impulse response function and is calculated as

$$\rho_{az} = 0.41 L \approx \frac{L}{2} \approx \frac{\lambda_E R_0}{2VT_0} \quad (3.15)$$

using eq. 3.9. The small deviation from the resolution of $L/2$ often found in the literature is due to the model of the antenna pattern (eq. 3.11) which we have used in this study to remain consistent with other literature [Alpers et al., 1981]. More realistically the antenna pattern should be modelled by a squared sinc function [Bamler and Schättler, 1993]. The azimuth resolution of the ERS-2 SAR is about 5 m.

3.2 Multilooking

Complex SAR data contain information on the time evolution of the NRCS during integration time. This information can, e.g. be extracted by applying the so called multi look technique. In this method the integration time is split into two or more subintervals and each interval is processed to a SAR image separately. In practice

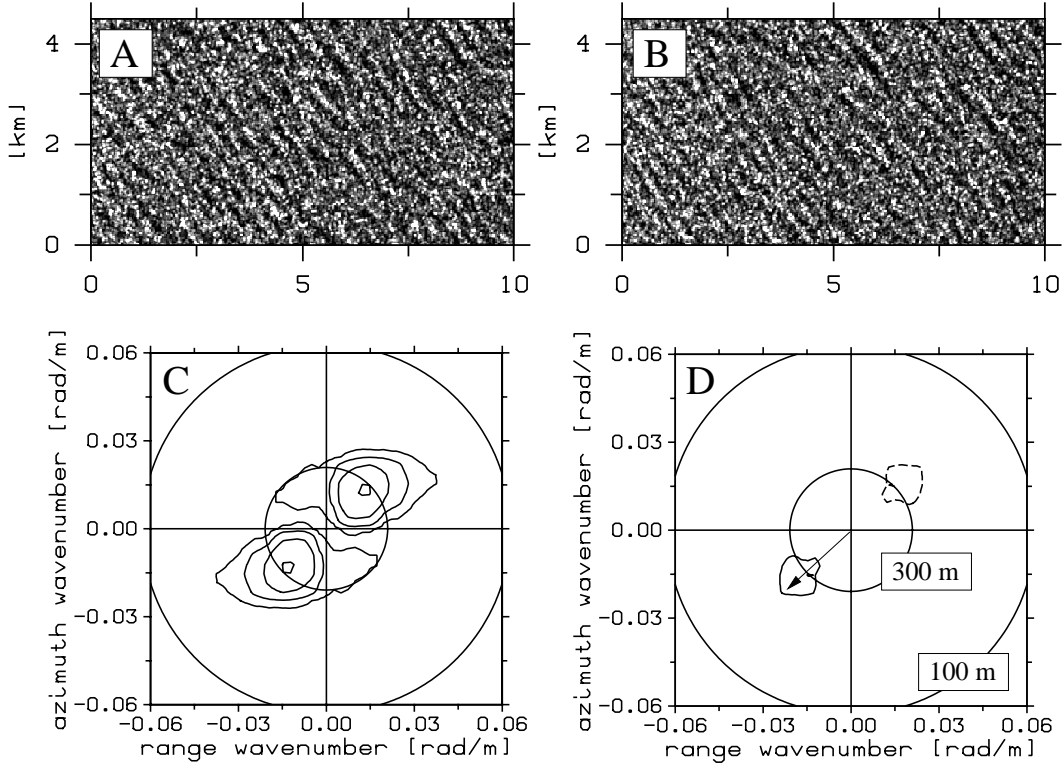


Fig. 3.4: (A,B) Two looks processed from the complex ERS-2 wave mode data. The looks are separated in time by 0.33 s, with the left look (A) followed by the right one. The corresponding single look intensity image is shown in Fig. 3.1. (C,D) Symmetric real part (C) and anti-symmetric imaginary part (D) of the corresponding look cross spectrum as defined in eq. 3.22, indicating a wave system of about 300 m wavelength propagating to the lower left. Dashed isolines indicate negative values.

the looks are calculated from a given complex SAR image c by selecting sub-bands from the corresponding azimuth Fourier spectrum. A theoretical expression for this spectrum in case of a single point scatterer can be calculated by applying both the convolution theorem and the stationary phase method [Bamler and Schättler, 1993] to eq. 3.13

$$\mathcal{F}(c) \approx \sqrt{\frac{i}{\text{FM}}} C(R_0) r(x_0, \frac{f}{\text{FM}}), G(\frac{f}{\text{FM}}) \quad (3.16)$$

with \mathcal{F} denoting the Fourier transform and frequency modulation rate FM given by

$$\text{FM} = -\frac{2V^2}{\lambda_E R_0} \quad (3.17)$$

For the ERS-2 SAR the FM rate is about -2100 Hz s^{-1} . It can be seen that via

$$t = \frac{f}{\text{FM}} \quad (3.18)$$

a correspondence between time t and frequency f is given. This means that selecting sub-bands from the azimuth spectrum of complex data is equivalent to selecting

subintervals of the integration time T_0 . Denoting the band pass filter used for look generation by H^i a look I_σ^i is calculated as follows:

$$I_\sigma^i = |\mathcal{F}^{-1}(\mathcal{F}(c) H^i)|^2 \quad i = 1, 2 \quad (3.19)$$

Fig. 3.3 (A) shows the azimuth spectrum of the complex ERS-2 imager in Fig 3.1. The Doppler centroid frequency f_{dc} denotes the centre of the antenna beam. The fact that f_{dc} is not zero is due to the squinted antenna geometry (compare with Fig. 3.2). The usable frequency bandwidth is about 2100 Hz corresponding to 0.66 s integration time. Fig. 3.3 (B) shows the azimuth spectrum with antenna weighting removed together with two filter functions H_1, H_2 used to extract two looks I_σ^1, I_σ^2 . Both the separation time between the looks and the integration time of each look is about 0.33 s. For the general case assuming that the filter functions are centred at frequencies $f_1 < f_2$, the looks are separated in time by

$$\Delta t = \frac{f_1 - f_2}{\text{FM}} > 0. \quad (3.20)$$

Two looks processed from the complex data of the ERS-2 image in Fig. 3.1 are shown in Fig. 3.4 (A,B). Due to the reduced bandwidth both looks have a lower azimuthal resolution, i.e. in case half the integration time is used for both looks the respective azimuthal resolution is about 20 m.

3.3 SAR cross spectra

In this section the cross spectrum of two looks processed by applying the technique described in the previous section is introduced. The standard estimation technique is recovered and cross spectra coherence is introduced. In summary it will be demonstrated that cross spectra have the following two advantages compared to conventional SAR image variance spectra:

- SAR cross spectra provide information on ocean wave propagation directions without ambiguity.
- SAR cross spectra have lower noise levels.

The use of SAR cross spectra for ocean wave measurements is well established by now [Engen and Johnson, 1995]. The idea is to use the time gap between two looks to gain information about wave motion and in particular wave propagation directions. As the shift of wave patterns during integration time is small compared to the resolution of common spaceborne SAR systems, a sensitive estimation technique has to be used to detect the differences between the two looks. Fig. 3.5 shows the shift of wave patterns taking place during a time $\Delta t = 0.33$ s, which corresponds to a look extraction as indicated in Fig. 3.3, and $\Delta t = 0.66$ s, which is the upper limit for the ERS-2 case. The dashed line in Fig. 3.5 (A) represents the azimuthal and approximate range resolutions for looks with half bandwidth. As one can see, the expected phase shifts are in fact on the sub-resolution scale even for the longest waves, which have the highest phase speeds (compare eq. 2.10). It should be noted that the phases given in Fig. 3.5 (A) are based on a linear imaging model, which has some shortcomings

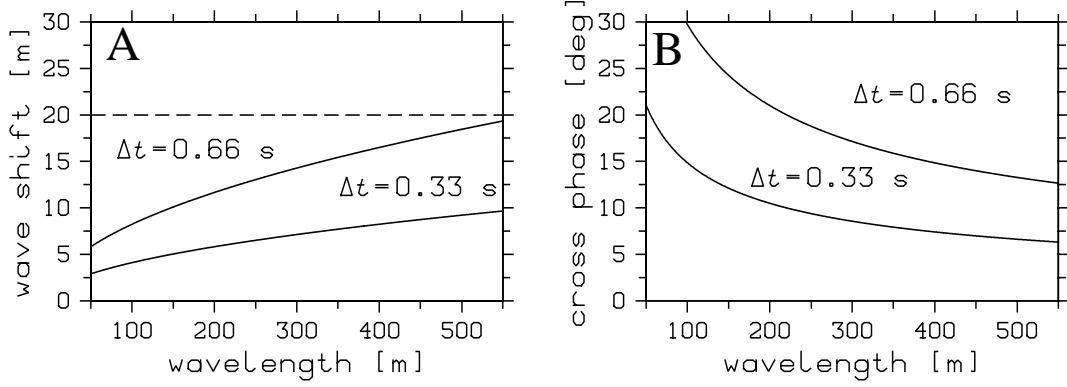


Fig. 3.5: (A) Shift of waves patterns taking place between look acquisition as a function of ocean wavelength assuming look separation times of $\Delta t = 0.33$ s and $\Delta t = 0.66$ s. The dashed line indicates the ERS-2 azimuth resolution for looks with half azimuth bandwidth. (B) The same as (A) for the cross spectrum phase.

in particular for shorter waves. In the general case the cross spectrum phases can deviate from the theoretical values due to nonlinear effects. A model to describe these distortions will be presented in Chapter 4. The data analysis presented in Chapter 8 will show that at least on average there is good agreement of the measurements with the linear model.

A standard approach to detect small phase shifts is to compute the cross spectrum [Honerkamp, 1993] of the looks, which is defined as the Fourier spectrum of the cross covariance function $\rho_{I_\sigma^1 I_\sigma^2}$

$$\Phi_k^{I_\sigma^1 I_\sigma^2} = \mathcal{F}(\rho_{I_\sigma^1 I_\sigma^2}) \quad . \quad (3.21)$$

The cross spectrum can alternatively be written as [Honerkamp, 1993]

$$\Phi_k^{I_\sigma^1 I_\sigma^2} = \langle \mathcal{F}(I_\sigma^1 - \langle I_\sigma^1 \rangle) \mathcal{F}(I_\sigma^2 - \langle I_\sigma^2 \rangle)^* \rangle \quad , \quad (3.22)$$

where the asterisk denotes complex conjugation. The cross spectrum is a complex valued function with symmetric real and antisymmetric imaginary part, i.e.

$$\text{Re}(\Phi_k^{I_\sigma^1 I_\sigma^2}) = \text{Re}(\Phi_{-k}^{I_\sigma^1 I_\sigma^2}) \quad (3.23)$$

$$\text{Im}(\Phi_k^{I_\sigma^1 I_\sigma^2}) = -\text{Im}(\Phi_{-k}^{I_\sigma^1 I_\sigma^2}) \quad , \quad (3.24)$$

with the positive peaks of the imaginary part indicating the propagation direction of the different harmonic wave components. Fig. 3.4 shows the real part (C) and imaginary part (D) of the cross spectrum computed from the looks shown in (A) and (B). A wave system of about 300 m wavelength can be seen propagating to the left. The collocated two-dimensional wave spectrum in Fig. 3.6 (A) computed with the WAM model confirms this finding.

3.3.1 Cross spectra estimation

A common way to estimate the cross spectrum is to average so called cross periodograms [Honerkamp, 1993]. A cross periodogram of two looks I_σ^1, I_σ^2 is defined

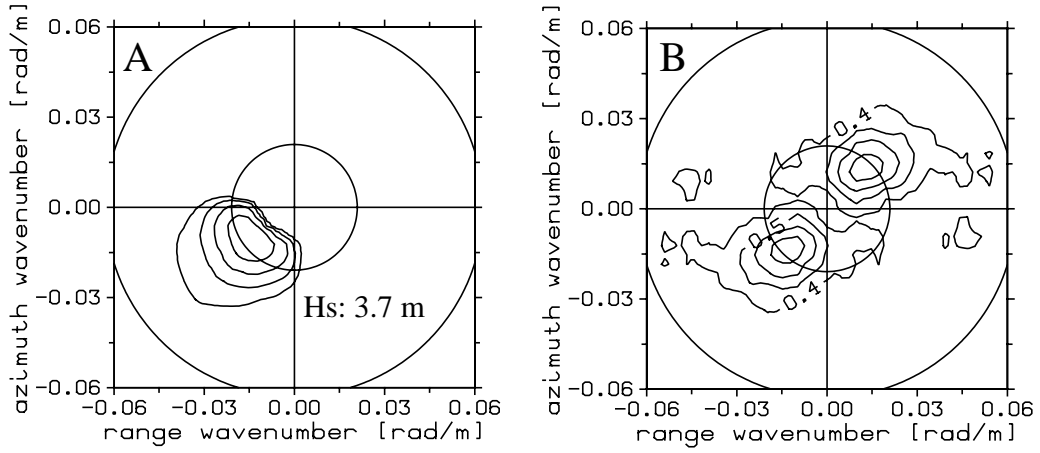


Fig. 3.6: (A) Two-dimensional wave spectrum computed with the WAM model collocated with the cross spectrum shown in Fig. 3.4. (B) Coherence estimate of the respective cross spectrum.

as

$$\overline{\Phi}_k^{I_\sigma^1 I_\sigma^2} = \hat{I}_k^1 (\hat{I}_k^2)^* , \quad (3.25)$$

where \hat{I}^i , $i = 1, 2$ are the discrete complex Fourier transforms of the looks given by

$$\hat{I}_{j_x j_y}^i = \sum_{i_x=0}^{N_x-1} \sum_{i_y=0}^{N_y-1} I_{i_x i_y}^i \exp \left[-2\pi i \left(\frac{i_x j_x}{N_x} + \frac{i_y j_y}{N_y} \right) \right] \quad i = 1, 2 \quad . \quad (3.26)$$

Here, we have assumed that the looks I_σ^1, I_σ^2 have $N_x \times N_y$ pixel. Denoting the pixel size of the looks with d_x, d_y the indices j_x, j_y of the spectrum refer to a wavenumber grid (with unit rad m^{-1}) of the following form:

$$\mathbf{k}_{i_x, i_y} = \left(\frac{2\pi i_x}{N_x d_x}, \frac{2\pi i_y}{N_y d_y} \right), \quad i_x = -N_x/2, \dots, N_x/2, \quad i_y = -N_y/2, \dots, N_y/2 \quad (3.27)$$

A standard technique to obtain an asymptotically consistent and unbiased estimator $\hat{\Phi}$ for the cross spectrum is to average cross periodograms $\overline{\Phi}_k^{I_\sigma^1 I_\sigma^2}$ obtained from N subimages at the cost of lower spectral resolution, i.e.

$$\hat{\Phi}_k^{I_\sigma^1 I_\sigma^2} = \frac{1}{N} \sum_{i=1}^N \overline{\Phi}_k^{I_\sigma^1 I_\sigma^2(i)} . \quad (3.28)$$

There are alternative ways to estimate the cross spectrum, e.g. by first estimating the cross covariance function and then applying definition eq. 3.29. However, as there is no obvious optimal choice of method in the present framework, the cross periodogram averaging technique is used in this study, mainly because it is easy to compute and to handle theoretically as will be shown in Chapter 4.

3.3.2 SAR cross spectra coherence

Another interesting quantity provided by the multilook technique is the coherence γ . A first analysis of the look cross spectra coherence in the framework of SAR ocean wave measurements has been performed in *Schulz-Stellenfleth et al.* [2002]. The coherence enables a quantification of the decorrelation of the two looks and can, e.g. be used to derive error bars for the cross spectrum phase as will be shown in Section 6.

The cross spectrum coherence is defined as the complex valued cross-correlation function of the two look spectra I_k^1, I_k^2 , i.e.

$$\gamma_k = \frac{\Phi_k^{I_\sigma^1 I_\sigma^2}}{\sqrt{\Phi_k^{I_\sigma^1 I_\sigma^1} \Phi_k^{I_\sigma^2 I_\sigma^2}}} \quad (3.29)$$

with

$$0 \leq |\gamma_k| \leq 1 \quad . \quad (3.30)$$

For $|\gamma_k| = 1$ the looks are perfectly correlated whereas complete decorrelation is indicated by $|\gamma_k| = 0$.

In the framework of ocean waves it can be assumed that

$$\Phi_k^{I_\sigma^1 I_\sigma^1} = \Phi_k^{I_\sigma^2 I_\sigma^2} \quad , \quad (3.31)$$

because the look variance spectra are directly related to the corresponding ocean wave spectra [*Hasselmann and Hasselmann*, 1991]. As the ocean wave spectrum can be assumed as constant on the look separation time scale the assumption is justified.

A natural estimator for the coherence is given by separate estimation of the nominator and denominator in eq. 3.29 using a periodogram and cross periodogram averaging technique as described above.

Fig. 3.6 (B) shows the coherence γ estimated for the cross spectrum in Fig. 3.4. The isolines have a linear spacing of 0.1. The maximum coherence is about 0.75 and is observed at the peak wave vector already found in the cross spectrum. An explanation for this finding will be given in Chapter 6.

3.4 Speckle noise

In this section the impact of SAR image speckle noise on the image variance spectrum and the look cross spectrum are explained.

Radar signals returned from different scatterer within a SAR resolution cell add up coherently as in a random walk. As there are many scatterer with uncorrelated complex reflectivities contributing, real and imaginary parts of a complex SAR image are independent Gaussian distributed. Hence, the intensity I_σ of a single look complex pixel follows a negative exponential distribution [*Goodman*, 1985; *Oliver and Quegan*, 1998] with probability density function (pdf) given by

$$\text{pdf}(I_\sigma) = \frac{1}{\langle I_\sigma \rangle} \exp\left[-\frac{I_\sigma}{\langle I_\sigma \rangle}\right] \quad . \quad (3.32)$$

A basic property of this distribution is that the variance $\text{var}(I_\sigma)$ equals the squared mean $\langle I_\sigma \rangle^2$. Therefore, SAR image statistics is commonly analysed using a multiplicative noise model, where SAR image intensity I_σ is expressed as the product of a negative exponential distributed speckle process S with unit mean and a process X carrying the cross section information [Oliver and Quegan, 1998; Alpers and Hasselmann, 1982], i.e.

$$I_\sigma = X S, \quad (3.33)$$

with both processes assumed as independent. For a SAR image acquired over the ocean, X is modulated by the underlying NRCS of the sea surface, which is basis for the retrieval of ocean wave spectra as discussed in Chapter 9. According to our assumptions, the mean of X which is, e.g. relevant for wind speed measurements, is simply given by

$$\langle X \rangle = \langle I_\sigma \rangle, \quad (3.34)$$

where brackets indicate spatial averages. Wave measurements are commonly based on a normalised, i.e. calibration independent version of X defined as

$$m = \frac{X - \langle X \rangle}{\langle X \rangle}. \quad (3.35)$$

It is straightforward to show that the covariance functions of m and the respective normalised intensity image I defined as

$$I = \frac{I_\sigma - \langle I_\sigma \rangle}{\langle I_\sigma \rangle} \quad (3.36)$$

are connected by the following equation [Kerbaol *et al.*, 1998]:

$$\rho_{II} = \rho_{mm} (\rho_{SS} + 1) + \rho_{SS}. \quad (3.37)$$

The corresponding variance spectrum Φ^I follows by taking the Fourier transform of eq. 3.37

$$\Phi^I = \Phi^m + \Phi^S + \Phi^m \otimes \Phi^S. \quad (3.38)$$

Here, \otimes denotes the convolution operator. To first order it can be assumed that the correlation length of the speckle S , which is in the order of the system resolution is shorter than the correlation length of the modulation m [Kerbaol *et al.*, 1998]. Eq. 3.38 then simplifies to

$$\Phi^I = \Phi^m + \Phi^S (1 + \text{var}(m)). \quad (3.39)$$

It can be seen, that the first order impact of SAR image speckle on the normalised SAR image variance spectrum is an additive noise floor. Furthermore, the variance of the modulation m caused by ocean waves is in general smaller than 1 [Lehner *et al.*, 2000].

Assuming white speckle noise and a SAR system with range and azimuth resolution ρ_{az} and ρ_{ra} the noise floor is therefore approximately given by [Mastenbroek and de Valk, 2000]

$$\Phi_k^S \approx \frac{\rho_{az} \rho_{ra}}{4 \pi^2}. \quad (3.40)$$

A first-order correction for image speckle is thus to subtract this noise level from the normalised SAR image variance spectrum, yielding an estimate for the variance

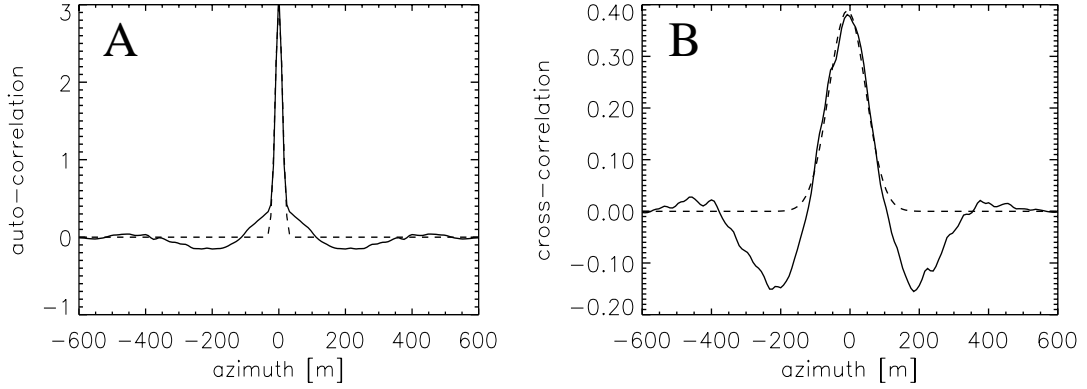


Fig. 3.7: (A) Azimuth auto-correlation function of the intensity image shown in Fig. 3.1. (B) Respective cross-correlation function of two looks with non-overlapping frequency bands. The dashed lines are fitted Gaussian functions.

spectrum of m . One should be aware that this correction is approximative with the complete speckle impact described by eq. 3.38.

The impact of image speckle on the look cross spectrum is straightforward if we assume that the frequency bands used to process the looks do not overlap (compare figure 3.4). In that case the looks are affected by uncorrelated speckle processes S_1 and S_2 and the looks can be written as

$$I_{\sigma}^i = X_i S_i, \quad i = 1, 2. \quad (3.41)$$

It can then be readily shown that

$$\rho_{I_{\sigma}^1 I_{\sigma}^2} = \rho_{X_1 X_2} \quad (3.42)$$

and thus the speckle noise cancels out in the expectation value. Due to definition the same applies for the look cross spectrum

$$\Phi_k^{I_{\sigma}^1 I_{\sigma}^2} = \mathcal{F}(\rho_{X_1 X_2}). \quad (3.43)$$

For a stationary scene with $X_1 = X_2$ the cross spectrum thus equals the variance spectrum of X .

It should be pointed out that the image speckle cancels out only in the exact cross spectrum (i.e. in the sense of expectation values), which is of course not available in practice. An analysis of the speckle impact on the estimated cross spectrum is given in Chapter 6.

A comparison of the impact of speckle on the auto- and cross-covariance functions of two looks is shown in Fig. 3.7. It can be seen that the auto-covariance function (A) in the azimuth direction is affected by a strong peak in the centre associated with the speckle correlation length, while the cross-covariance function (B) is a damped cosine representing the correlation properties of the underlying NRCS. The azimuth cross-correlation function is one important tool for the investigation of ocean wave damping by sea ice presented in Chapter 7.

Chapter 4

SAR OCEAN WAVE IMAGING THEORY

In this section the basic elements of the standard SAR ocean wave imaging theory are reviewed. Furthermore, a modification of the existing model for look cross spectra is presented, which is of relevance in particular for future high resolution systems like TerraSAR [Mittermayer *et al.*, 2002] and airborne systems.

SAR imaging of the sea surface has been investigated in many studies [Hasselmann and Hasselmann, 1991; Hasselmann *et al.*, 1985; Lyzenga, 1988; Alpers *et al.*, 1981]. A major step in understanding the SAR ocean wave imaging process was the derivation of a nonlinear integral transform describing the mapping of a two-dimensional ocean wave spectrum into the corresponding SAR image variance spectrum [Hasselmann and Hasselmann, 1991] or look cross spectrum respectively [Engen and Johnson, 1995].

The SAR imaging mechanism is sensitive to both the NRCS modulation and the sea surface motion associated with ocean waves. The standard model used in literature consists of three main parts:

- The first important element is the local radar backscattering mechanism, which is governed by the sea surface roughness on a centimetre scale.
- Secondly, the modulation of the local backscatter processes by long waves (longer than twice the SAR resolution cell) is discussed assuming a stationary sea surface. This mechanism is known as the real aperture radar (RAR) modulation mechanism, as it describes the radar cross section as seen by a conventional radar without synthesised antenna.
- In the final step the impact of Doppler shifts associated with wave motion on the SAR image formation is explained. The respective mechanism is known as the velocity bunching effect.

As a modification of the standard theory a nonlinear formulation of the RAR modulation mechanism is proposed. The approach is able to avoid negative SAR intensities, which can occur in the existing model at higher sea states. It is shown that this effect is significant in particular for systems with high resolution in range direction. Based on the nonlinear RAR model a new integral transform for look cross spectra is derived and compared to the existing transform.

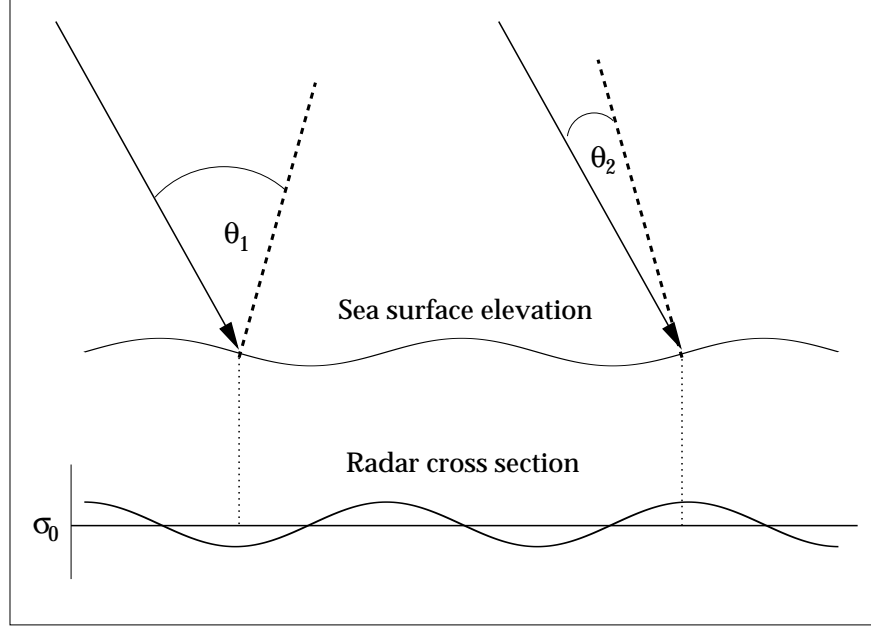


Fig. 4.1: Illustration of the real aperture radar (RAR) tilt modulation mechanism. Due to the modulation of the local incidence angle by the long waves (longer than twice the resolution cell) the cross section pattern is shifted by 90° towards the radar with respect to the sea surface elevation.

4.1 Backscattering model for the sea surface

4.1.1 Bragg scattering

Assuming incidence angles between 20° and 60° the microwave radar return from the ocean surface is dominated by Bragg scattering [Hasselmann *et al.*, 1985]. The backscatter is thus governed by the sea surface roughness on the scale of the radar wavelength, which is 5.6 cm for the ERS SAR. With incidence angles between 20° and 26° the ERS SAR falls into the Bragg regime. The NRCS is related to the spectral wave energy F contained in the short ripple waves with Bragg wavenumber k_B via

$$\sigma_0 = \gamma_G [F(\mathbf{k}_B) + F(-\mathbf{k}_B)] , \quad (4.1)$$

where γ_G is a factor depending on incidence angle, polarisation and the dielectric constant of sea water [Valenzuela, 1978; Apel, 1995]. The wave vector \mathbf{k}_B lies in the incidence plane and has to satisfy the Bragg condition [Apel, 1995]

$$k_B = 2 k_E \sin \theta . \quad (4.2)$$

Here, k_E is the electromagnetic wavenumber and θ is the incidence angle. For the ERS SAR the range of Bragg wavelength is between 0.065 m and 0.085 m corresponding to incidence angles of 26° and 20° . As the high frequency tail of the wave spectrum

wind speed	5 ms ⁻¹	10 ms ⁻¹	15 ms ⁻¹
coherence time τ_c	0.1 s	0.052 s	0.034 s

Tab. 4.1: Coherence time τ_c for different wind speeds assuming C-band and 30° incidence angle (adapted from *Milman et al.* [1993])

is characterised by a ω^{-5} decay of energy (compare eq. 2.22), the radar return is increasing with decreasing incidence angles. This is an effect which can, e.g. be seen on ERS full swath data, where the NRCS decreases in the order of 5 dB going from near range to far range.

Apart from knowledge about the NRCS, the spatial and temporal correlation properties of the complex reflectivity r , which is the basic quantity measured by a SAR (compare Chapter 3), are required to model the SAR imaging process. As in most studies, we will assume that r is a white process in the spatial domain [*Hasselmann et al.*, 1985].

For the temporal correlation of r in the open water we assume coherence times as given by *Milman et al.* [1993] for C-band and 30° incidence angle, which is close the ERS configuration. The respective values for different wind speed are summarised in table 4.1. The auto-correlation function of r can then be written as

$$\langle r(\mathbf{x}_1, t_1) r^*(\mathbf{x}_2, t_2) \rangle = \sigma_0(\mathbf{x}_1, \frac{t_1 + t_2}{2}) \delta(\mathbf{x}_1 - \mathbf{x}_2) \exp\left[-\frac{(t_1 - t_2)^2}{\tau_s^2}\right] \quad (4.3)$$

with angle brackets indicating averages over different realisations of the r process.

4.1.2 Two-scale model

Based on the Bragg scattering theory explained above, SAR ocean wave imaging can be explained based on a two-scale model of the ocean wave spectrum [*Hasselmann et al.*, 1985; *Alpers and Rufenach*, 1979]. In this approach the wave spectrum is split into short ripple waves responsible for the Bragg scattering mechanism and longer waves modulating these local processes. The model explains the radar cross section as seen by a conventional real aperture radar and is therefore called RAR modulation. The dominant RAR modulation mechanism are the following [*Schmidt*, 1995]:

- Tilt modulation: Long waves modulate the local incidence angle and thus the radar return according to the Bragg condition eq. 4.2 (compare Fig. 4.1).
- Hydrodynamic modulation: Hydrodynamic interactions lead to the modulation of energy contained in the Bragg waves by longer waves.
- Range Bunching: A pure geometric effect, which leads to a modulation of SAR image intensities associated with surface slopes caused by longer waves.

RAR modulation dominates imaging of range travelling waves and is in general assumed to be a linear process [*Alpers et al.*, 1981]. It can therefore be written using a transfer function T^R as [*Hasselmann and Hasselmann*, 1991]

$$I^{RL} = \frac{\sigma_0(\mathbf{x}, t) - \langle \sigma_0 \rangle}{\langle \sigma_0 \rangle} = 2 \operatorname{Re} \left(\sum_k T_k^R \zeta_k \exp[-i(\mathbf{k} \cdot \mathbf{x} - \omega t)] \right), \quad (4.4)$$

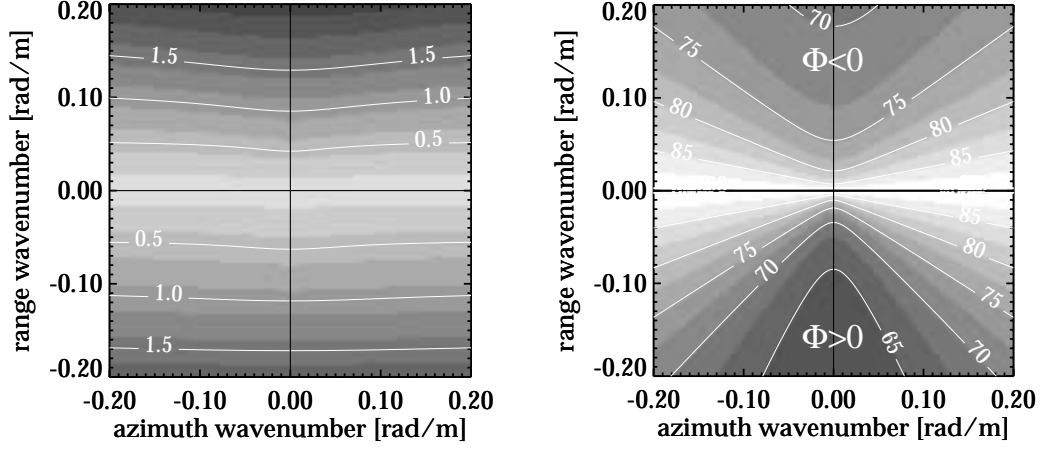


Fig. 4.2: Modulus (left) and absolute phase values (right) of theoretical RAR transfer function (compare eq. 4.5). A right looking SAR (looking in negative k_y direction) with VV polarisation and 23.5° incidence angle is assumed.

where ζ_k is the complex spectrum of the sea surface elevation (compare eq. 2.14). As all three modulation mechanisms are assumed to be independent T^R can be expressed as the sum of the respective transfer functions:

$$T_k^R = T_k^{tilt} + T_k^{hydr} + T_k^{rb} \quad (4.5)$$

For vertical polarisation in transmit and receive (VV) and a right looking SAR imaging geometry analytical expressions for the transfer functions are given by the following expressions:

$$T_k^{tilt} = -\frac{4 i k_y \cot \theta}{1 + \sin^2 \theta} \quad (4.6)$$

$$T_k^{rb} = -i k_y \frac{\cos \theta}{\sin \theta} \quad (4.7)$$

$$T_k^{hyd} = 4.5 \omega \frac{k_y^2}{|k|} \frac{\omega - i\mu}{\omega^2 + \mu^2} \quad (4.8)$$

Here, μ is the hydrodynamic relaxation rate, which is chosen as 0.5 s^{-1} following Hasselmann and Hasselmann [1991].

In Fig. 4.2 the modulus and absolute values of the phases of the theoretical RAR MTF are plotted. A right looking SAR (looking in negative k_y direction) with VV polarisation and 23.5° incidence angle is assumed. Negative phases are found for positive range wavenumbers and vice versa. According to the definition of the transfer function a positive phase indicates a shift of the respective harmonic wave in opposite wave propagation direction. It can be seen that the RAR modulation becomes stronger with increasing range wave numbers and is negligible for waves travelling in flight direction. The NRCS pattern is always shifted towards the radar with respect to the sea surface elevation. Due to the hydrodynamic modulation, this effect is stronger if the wave is propagating in opposite look direction.

Finally, it should be noted that the choice of the separation wavenumber required in the two-scale model is not straightforward. It can be chosen either independent of the SAR sensor from pure electromagnetic and hydrodynamic considerations (EMH model) [Hasselmann *et al.*, 1985] or dependent on the SAR resolution (SAR two-scale model) [Hasselmann *et al.*, 1985; Kasilingam and Shemdin, 1990]. In this thesis the view of the EMH model is taken, which is based on the backscatter from single facets consisting of a small number (about 10) of Bragg wavelength. As shown, e.g. in Milman *et al.* [1993] the white process assumption about the complex reflectivity r (compare eq. 4.3) is well satisfied on this spatial scale. The choice of model has some implications for the interpretation of the coherence time τ_s defined in eq. 4.3. Within the SAR two-scale model τ_s refers to the temporal decorrelation of the backscatter returned from a SAR resolution cell, which is an order of magnitude larger than a facet, at least for the ERS SAR system with about 20 m resolution. As this decorrelation depends not only on the time evolution of the small scale facets (intrinsic decorrelation) but also on the motion of the intermediate waves shorter than twice the SAR resolution and longer than the facet size, τ_c has a different meaning in this model [Vachon *et al.*, 1993].

4.1.3 A nonlinear RAR model

A shortcoming of the linear RAR model given by eq. 4.4 not discussed in the literature so far is the fact that negative values for the radar cross section can occur, which have no physical meaning. Using the JONSWAP spectrum eq. 2.22 as input, Fig. 4.3 (D) shows the percentage of image points which have a negative radar cross section as a function of wavelength, assuming a range resolution of $\rho_r=25$ m (dashed line), which corresponds to the ERS SAR configuration and $\rho_r=2$ m, which will be the level of resolution achieved by future SAR systems like TerraSAR. The curve was computed by first calculating the RAR image variance according to

$$\langle (I^{RL})^2 \rangle = \sum_k |T_k^R|^2 F_k \Delta \mathbf{k} , \quad (4.9)$$

and then using the fact that I^{RL} is Gaussian distributed. One can see that the frequency of physically meaningless predictions for the radar cross section is relative moderate for the ERS SAR case with less than 10% even for higher waves. However, due to the functional dependence of T^R on the range wavenumber (compare eq. 4.6) the observed effect becomes stronger with increasing range resolution. For the TerraSAR configuration the percentage is around 20% even for moderate sea states. While the effect is regarded as acceptable for the ERS case, at least for moderate sea states, it is certainly not tolerable for high resolution systems.

To overcome the problem described above we propose to replace the linear model for the RAR modulation given by eq. 4.4 by an exponential formulation as follows:

$$\sigma_0 \langle \sigma_0 \rangle^{-1} = I^{RL} + 1 \quad \longrightarrow \quad \sigma_0 \langle \sigma_0 \rangle^{-1} = \alpha_1 \exp[\alpha_2 I^{RL}] \quad (4.10)$$

In the new formulation the cross section has a log-normal distribution, which is a standard distribution used in SAR image analysis [Oliver and Quegan, 1998]. The transformation eq. 4.10 is mainly chosen because it is simple to handle from the

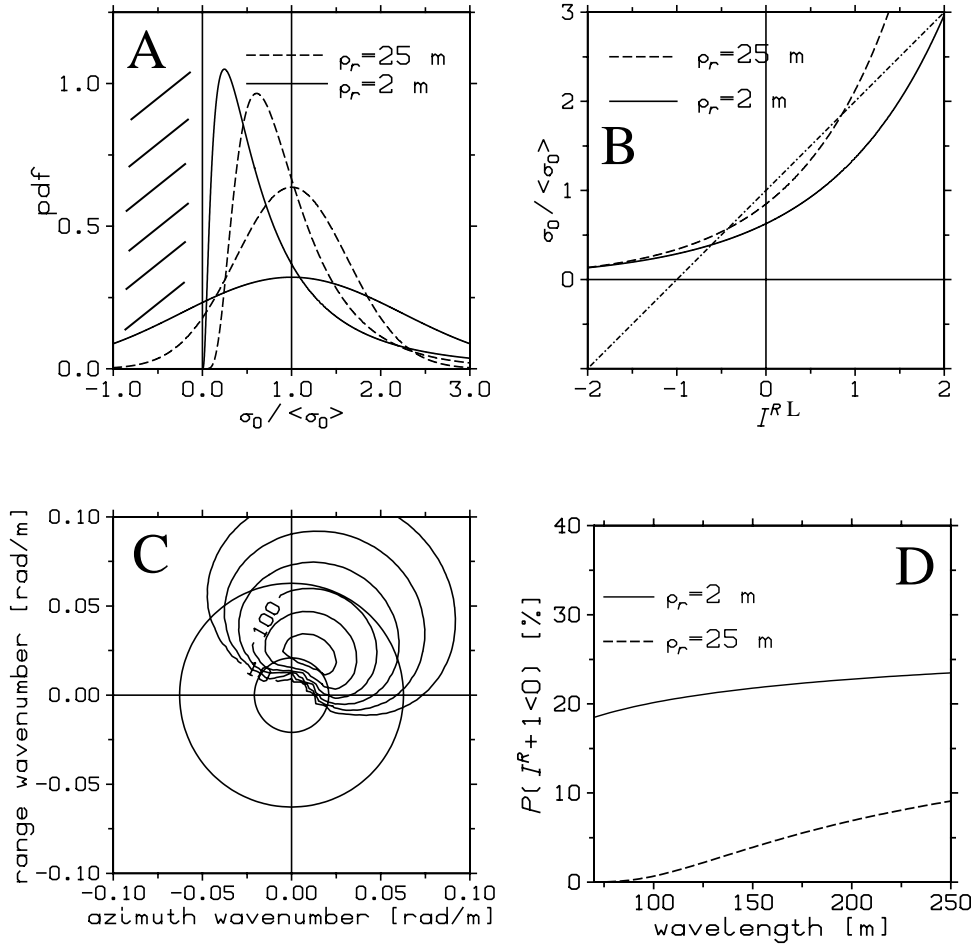


Fig. 4.3: (A) Probability density functions of the normalised RAR image using the linear model eq. 4.4 (Gaussian curves) and the exponential model as given in eq. 4.10 for range resolutions of $\rho_r=25$ m (dashed curves) and $\rho_r=2$ m (solid curves). (B) Respective functional dependence of the RAR image on the zero mean process I^{RL} for the exponential model (solid and dashed curve) and the linear model (dashed dotted curve). (C) JONSWAP spectrum representing a fully developed wind sea with 200 m wavelength and 4.5 m significant wave height. (D) Percentage of negative RAR image points predicted by the linear model as a function of wavelength for fully developed wind seas assuming different range resolutions.

analytical point of view, which will be important in the derivation of the nonlinear transform in Section 4.3.2. To keep the linear and exponential models consistent, the parameters α_1 and α_2 are chosen such that both the mean and the variance of the linear formulation are maintained, i.e.

$$\langle \alpha_1 \exp[\alpha_2 I^{RL}] \rangle = 1 \quad (4.11)$$

$$\langle \alpha_1^2 \exp[2 \alpha_2 I^{RL}] \rangle = \rho^{II}(0) + 1 \quad , \quad (4.12)$$

where $\rho^{II}(0)$ is the variance of the RAR image I^{RL} . By straightforward integration this condition leads to

$$\alpha_1 = \left(1 + \rho^{II}(0)\right)^{-1/2} \quad (4.13)$$

$$\alpha_2 = \sqrt{\frac{\log(1 + \rho^{II}(0))}{\rho^{II}(0)}}. \quad (4.14)$$

Fig. 4.3 (A) shows a comparison of the probability density functions for $\sigma_0 \langle \sigma_0 \rangle^{-1}$ with the linear model (Gaussian curves) and the exponential model using a fully developed JONSWAP spectrum (C) with 200 m wavelength as input. As can be seen the linear model predicts negative cross sections in a significant number of cases, while the nonlinear formulation avoids this unwanted effect altogether.

4.2 Motion related SAR imaging mechanisms

In this section the impact of wave motion on the SAR imaging process is explained. The presentation starts with a brief description of the scanning distortion effect, which plays a minor role for spaceborne SAR systems and then moves on to the more important velocity bunching mechanism.

4.2.1 Scanning distortion

An ocean wave imaging mechanism, which in general has to be taken into account for scanning systems like SAR is the so called scanning distortion. This effect causes a shearing of the imaged ocean waves due to the finite radar platform velocity. As the ocean wave phase speed c_p for a given water depth is known theoretically (compare eq. 2.10), the mechanism can be readily modelled by applying the following transformation in the spectral domain [Schmidt, 1995]:

$$k'_x = k_x - \frac{c_p}{V} |k| \quad (4.15)$$

$$k'_y = k_y \quad (4.16)$$

Here, (k_x, k_y) are the original wavenumbers referring to the underlying ocean wave field and (k'_x, k'_y) are the corresponding wavenumbers in the the respective scanned image.

As the ratio of phase speed to platform velocity for spaceborne SAR systems like the ERS SAR is very small (<0.01), we will neglect it in this study. One should be aware however that for airborne systems the effect can be significant [Schulz-Stellenfleth and Lehner, 2001].

4.2.2 Velocity bunching

As explained in Chapter 3, SAR determines the azimuth position of backscattering objects by recording the Doppler history of the returned signals. As sea surface motion leads to a velocity component u_r of a backscattering ocean surface facet towards the

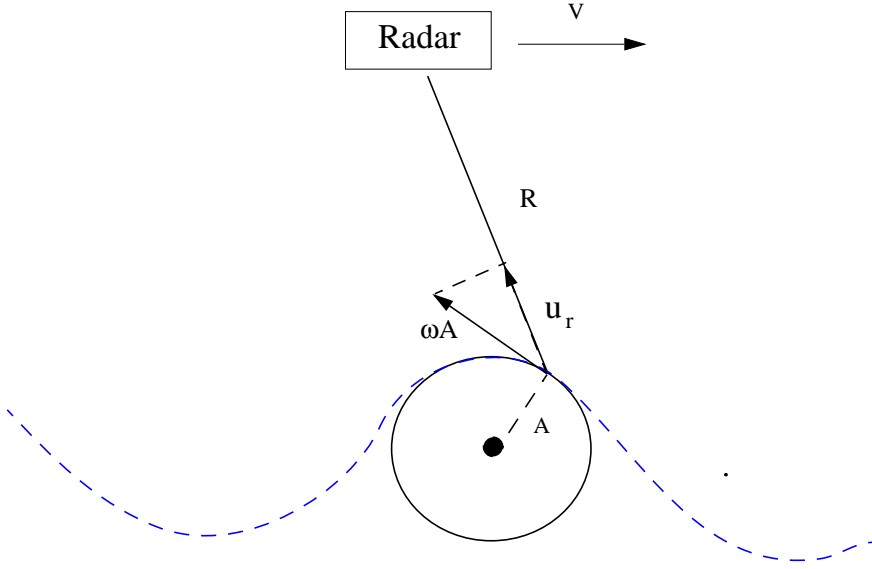


Fig. 4.4: Illustration of the velocity bunching mechanism. Water particles performing a circular motion (compare Chapter 2) have a velocity component in slant range direction of the radar. The resulting Doppler shift leads to shifts of the corresponding image points in the azimuth direction.

radar (slant range) the resulting effect is a shift of the corresponding SAR image point in flight direction [Lyzenga *et al.*, 1985] by a distance

$$\xi_x = \frac{R}{V} u_r . \quad (4.17)$$

For SAR imagery acquired over land this effect is for obvious reasons known as the “train off the track” effect. In case of the ocean the periodic movement of the surface leads to an alternate stretching and bunching of image intensities in azimuth (velocity bunching). The velocity bunching effect is a governing factor for SAR imaging of azimuth travelling waves and is in general strongly nonlinear [Alpers and Brüning, 1986].

Based on a standard SAR image processing procedure as described in Chapter 3, a model was derived for a SAR intensity image of a moving sea surface [Brüning *et al.*, 1990]. Assuming that the NRCS of the sea surface is given by σ_0 and furthermore that the orbital velocity associated with the ocean waves has a slant range component u_r , an integral expression for the SAR intensity image is given by [Brüning *et al.*, 1990]:

$$I_\sigma(\mathbf{x}) = \frac{\pi T_0^2 \rho_a}{2} \int \frac{\sigma_0(\mathbf{x}')}{\hat{\rho}_a^2(\mathbf{x}')} \exp \left[-\frac{\pi^2}{\hat{\rho}_a^2} (x - x' - \beta u_r(\mathbf{x}'))^2 \right] \delta(y' - y) dx' dy' . \quad (4.18)$$

Here, x and y are the azimuth and range coordinates, β is defined as

$$\beta = \frac{R}{V} , \quad (4.19)$$

T_0 is the SAR integration time and $\hat{\rho}_a$ is the degraded azimuthal resolution given by

$$\hat{\rho}_a = \rho_a \sqrt{1 + \frac{T_0^2}{\tau_s^2}} \quad , \quad (4.20)$$

with scene coherence time τ_s and azimuth resolution ρ_a . Eq. 4.18 is based on the SAR processing procedure as described in Section 3.1, in particular with antenna pattern as defined in eq. 3.11. Furthermore, the correlation properties of the complex reflectivity r given in eq. 4.3 are used in the derivation.

A simple model for the orbital velocity required in eq. 4.18 is based on the linear wave theory presented in Chapter 2. As explained before, individual water particles follow a circular trajectory (compare Fig. 4.4), if deep water is assumed and nonlinear effects are neglected. In this case the slant range component of the orbital velocity component u_r can be related to the complex spectrum of the sea surface ζ_k via

$$u_r(\mathbf{x}, t) = 2 \operatorname{Re} \left(\sum_k T_k^u \zeta_k \exp[-i(\mathbf{k} \cdot \mathbf{x} - \omega t)] \right) \quad , \quad (4.21)$$

where T^u is the orbital velocity transfer function, which is for a right looking SAR system given by [Hasselmann and Hasselmann, 1991]

$$T_k^u = -\omega \left(\frac{k_y}{k} \sin \theta + i \cos \theta \right) \quad . \quad (4.22)$$

For small incidence angles the slant range velocity u_r is 90° phase shifted in wave propagation direction with respect to the surface elevation η and T^u simplifies to

$$T_k^u \approx -i \omega \quad . \quad (4.23)$$

The sign convention for u_r is such that positive velocities indicate a movement of the imaged facette towards the radar.

4.3 Cross spectra integral transform

Eq. 4.18 provides a mapping relation between one realisation of the ocean surface and the corresponding SAR image. In principle the transform can be used to estimate SAR image variance spectra or look cross spectra using a Monte Carlo technique as, e.g. performed in Br uning *et al.* [1990] or Schulz-Stellenfleth and Lehner [2001]. However, due to the computational effort this method is not practical for ocean wave retrieval schemes. The problem was solved however by the derivation of an analytical expression for the statistical moments of the SAR intensity image. For the first moment it can be shown [Krogstad, 1992] that

$$\langle I_\sigma \rangle = \langle \sigma_0 \rangle \quad , \quad (4.24)$$

i.e. the velocity bunching mechanism maintains the mean RAR image intensity. The second moments were derived in Hasselmann and Hasselmann [1991] relating the ocean wave spectrum F to the SAR image variance spectrum Φ^{II} . This expression was later extended to include finite SAR resolution and coherence time [Bao *et al.*, 1993] as well as SAR cross spectra [Engen and Johnson, 1995].

4.3.1 Integral transform derived by Engen & Johnson

Based on the linear model for the RAR image modulation eq. 4.4 the following integral transform relates F to the SAR cross spectrum of the normalised looks $I^i = \langle I_\sigma \rangle^{-1} (I_\sigma^i - \langle I_\sigma \rangle)$, $i = 1, 2$ separated by the time Δt [Engen and Johnson, 1995]:

$$\begin{aligned} \Phi_{\mathbf{k}}^{I^1 I^2} &= \frac{1}{4 \pi^2} \exp[-k_x^2 \beta^2 \rho^u(\mathbf{0}, 0)] \int d^2 x \exp[-i \mathbf{k} \cdot \mathbf{x}] \exp[k_x^2 \beta^2 \rho^{uu}(\mathbf{x}, \Delta t)] \\ &\cdot \left[1 + \rho^{II}(\mathbf{x}, \Delta t) + i k_x \beta (\rho^{Iu}(\mathbf{x}, \Delta t) - \rho^{Iu}(-\mathbf{x}, -\Delta t)) \right. \\ &\quad \left. + (k_x \beta)^2 (\rho^{Iu}(\mathbf{x}, \Delta t) - \rho^{Iu}(\mathbf{0}, 0)) (\rho^{Iu}(-\mathbf{x}, -\Delta t) - \rho^{Iu}(\mathbf{0}, 0)) \right] \end{aligned} \quad (4.25)$$

Here, the cross-covariance functions ρ^{II} , ρ^{uu} and ρ^{Iu} are defined as follows:

$$\begin{aligned} \rho^{II}(\mathbf{x}, \Delta t) &= 0.5 \int d^2 x \left(F_k |T_k^R|^2 \exp[i\omega \Delta t] \right. \\ &\quad \left. + F_{-k} |T_{-k}^R|^2 \exp[-i\omega \Delta t] \right) \exp[i \mathbf{k} \cdot \mathbf{x}] \end{aligned} \quad (4.26)$$

$$\begin{aligned} \rho^{Iu}(\mathbf{x}, \Delta t) &= 0.5 \int d^2 x \left(F_k T_k^R (T_k^u)^* \exp[i\omega \Delta t] \right. \\ &\quad \left. + F_{-k} (T_{-k}^R)^* T_{-k}^u \exp[-i\omega \Delta t] \right) \exp[i \mathbf{k} \cdot \mathbf{x}] \end{aligned} \quad (4.27)$$

$$\begin{aligned} \rho^{uu}(\mathbf{x}, \Delta t) &= 0.5 \int d^2 x \left(F_k |T_k^u|^2 \exp[i\omega \Delta t] \right. \\ &\quad \left. + F_{-k} |T_{-k}^u|^2 \exp[-i\omega \Delta t] \right) \exp[i \mathbf{k} \cdot \mathbf{x}] \end{aligned} \quad (4.28)$$

Expanding the transform eq. 4.25 to first order with respect to the wave spectrum F yields the linear approximation [Hasselmann and Hasselmann, 1991]

$$\Phi_k^{I^1 I^2}(\Delta t) \approx 0.5 \left(|T_k^S|^2 \exp(i\omega \Delta t) F_k + |T_{-k}^S|^2 \exp(-i\omega \Delta t) F_{-k} \right) \quad (4.29)$$

with SAR transfer function T^S given by

$$T_k^S = T_k^R - i \frac{R}{V} k_x T_k^u. \quad (4.30)$$

Expanding only the integral part of eq. 4.25 to linear order, keeping the leading exponential factor yields the quasi-linear transform given by

$$\begin{aligned} \Phi_k^{I^1 I^2}(\Delta t) &\approx 0.5 \exp[-k_x^2 \beta^2 \rho^u(\mathbf{0})] \\ &\quad \left(|T_k^S|^2 \exp[i\omega \Delta t] F_k + |T_{-k}^S|^2 \exp[-i\omega \Delta t] F_{-k} \right). \end{aligned} \quad (4.31)$$

To simplify the notation the auto-covariance function of u_r is written as

$$\rho^u(\mathbf{x}) = \rho^{uu}(\mathbf{x}, 0) \quad (4.32)$$

and hence $\rho^u(\mathbf{0})$ is the respective orbital velocity variance. The quasi-linear forward model is helpful as it allows a simple first order retrieval of two-dimensional wave spectra from SAR cross spectra.

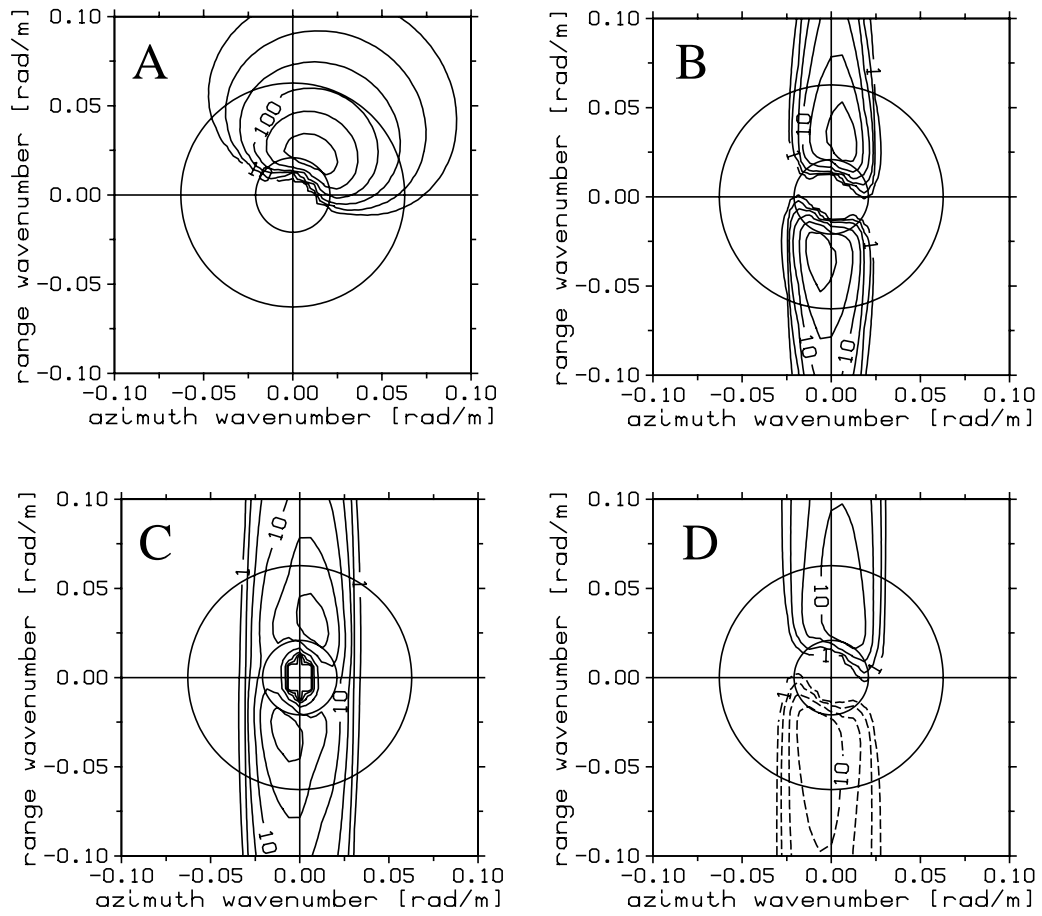


Fig. 4.5: Simulation of the SAR ocean wave imaging mechanism based on the nonlinear transform given by eq. 4.25 with wave spectrum (A) representing a fully developed wind sea of 200 m wavelength and 4.5 m wave height used as input, and resulting real part (C) and imaginary part (D) of the look cross spectrum. The imaging parameters of the ERS-2 SAR (compare table 5.1) were used for the simulation. The respective real part obtained with the quasi-linear model eq. 4.31 is shown in (B). Dashed isolines indicate negative values.

Fig. 4.5 shows a simulation of a look cross spectrum using a JONSWAP ocean wave spectrum with a fully developed wind sea system of 200 m wavelength (A) and 4.5 m significant wave height as input. The simulated real part and imaginary part of the cross spectrum are shown in Fig. 4.5 (C) and (D). One can see that, despite the distortions caused by the azimuthal cut-off and the nonlinear coupling of different wave components, the spectral peak of the ocean wave spectrum is still clearly visible in the cross spectrum with the correct propagation direction indicated by the positive peak of the imaginary part. Fig. 4.5 (B) shows the respective real part of the cross spectrum obtained with the quasi-linear model eq. 4.31. It can be seen that the

overall agreement with the nonlinear model is good in particular for longer wave components. The strongest deviations are observed in the cut-off region, where nonlinear coupling causes a shift of energy from shorter azimuth waves towards longer wave components.

4.3.2 New integral transform for high resolution SAR systems

In this section the derivation of a new transform analogue to eq. 4.25 with the linear RAR model replaced by the nonlinear formulation introduced in Section 4.1.3 (compare eq. 4.10) is presented. The transform is supposed to be a basis for inversion schemes, which have high resolution SAR data as, e.g. provided by TerraSAR as input. As shown in Section 4.1.3 the linear model fails to provide a realistic distribution of image intensities for such systems.

Using the stationarity and homogeneity of the sea surface, the look cross spectrum $\Phi^{I^1 I^2}$ can be written as (compare eq. 3.22)

$$\Phi_k^{I^1 I^2} = \frac{\alpha_1^2}{4\pi^2} \int G(\mathbf{x}, k_x) \exp[-i \mathbf{k} \cdot \mathbf{x}] d\mathbf{x} \quad (4.33)$$

with α_1 given by eq. 4.13 and G function defined as follows:

$$G(\mathbf{x}, k_x) = \langle \exp[\alpha_2 I^{RL}(\mathbf{x}, \Delta t) + \alpha_2 I^{RL}(\mathbf{0}, 0) - i k_x \frac{R}{V} (u_r(\mathbf{x}, \Delta t) - u_r(\mathbf{0}, 0))] \rangle \quad (4.34)$$

G can be written in terms of the characteristic function [Honerkamp, 1993] as

$$K(\mathbf{t}) = \langle \exp(i \mathbf{t}^T \mathbf{X}) \rangle, \quad (4.35)$$

with vectors \mathbf{t} and \mathbf{X} defined as follows:

$$\mathbf{X} = \left(I^{RL}(\mathbf{x}, t), I^{RL}(\mathbf{0}, 0), u_r(\mathbf{x}, t), u_r(\mathbf{0}, 0) \right)^T \quad (4.36)$$

$$\mathbf{t} = \left(-i \alpha_2, -i \alpha_2, -k_x \frac{R}{V}, k_x \frac{R}{V} \right)^T \quad (4.37)$$

Using the assumption that the wave field is Gaussian distributed the characteristic function K can be written as [Krogstad, 1992]

$$K(\mathbf{t}) = \exp(i \mathbf{t} \langle \mathbf{X} \rangle - \frac{1}{2} \mathbf{t}^T H \mathbf{t}) \quad (4.38)$$

with covariance matrix H given by

$$H = \begin{pmatrix} \rho^{II}(\mathbf{0}, 0) & \rho^{II}(\mathbf{x}, \Delta t) & \rho^{Iu}(\mathbf{0}, 0) & \rho^{Iu}(\mathbf{x}, \Delta t) \\ \rho^{II}(\mathbf{x}, \Delta t) & \rho^{II}(\mathbf{0}, 0) & \rho^{Iu}(-\mathbf{x}, -\Delta t) & \rho^{Iu}(\mathbf{0}, 0) \\ \rho^{Iu}(\mathbf{0}, 0) & \rho^{Iu}(-\mathbf{x}, -\Delta t) & \rho^{uu}(\mathbf{0}, 0) & \rho^{uu}(\mathbf{x}, \Delta t) \\ \rho^{Iu}(\mathbf{x}, \Delta t) & \rho^{Iu}(\mathbf{0}, 0) & \rho^{uu}(\mathbf{x}, \Delta t) & \rho^{uu}(\mathbf{0}, 0) \end{pmatrix}. \quad (4.39)$$

Inserting eqs. 4.37, 4.39 into eq. 4.38, the G function can be expressed in terms of the auto and covariance functions eq. 4.26-4.28 as follows:

$$G(\mathbf{x}, k_x) = \alpha_1^2 \exp[\alpha_2^2 \rho^{II}(\mathbf{0}, 0) - \beta^2 k_x^2 \rho^{uu}(\mathbf{0}, 0)] \exp[\alpha_2^2 \rho^{II}(\mathbf{x}, \Delta t)] \\ \exp\left[i \beta \alpha_2 k_x (\rho^{Iu}(\mathbf{x}, t) - \rho^{Iu}(-\mathbf{x}, -\Delta t)) + \beta^2 k_x^2 \rho^u(\mathbf{x}, \Delta t)\right] \quad (4.40)$$

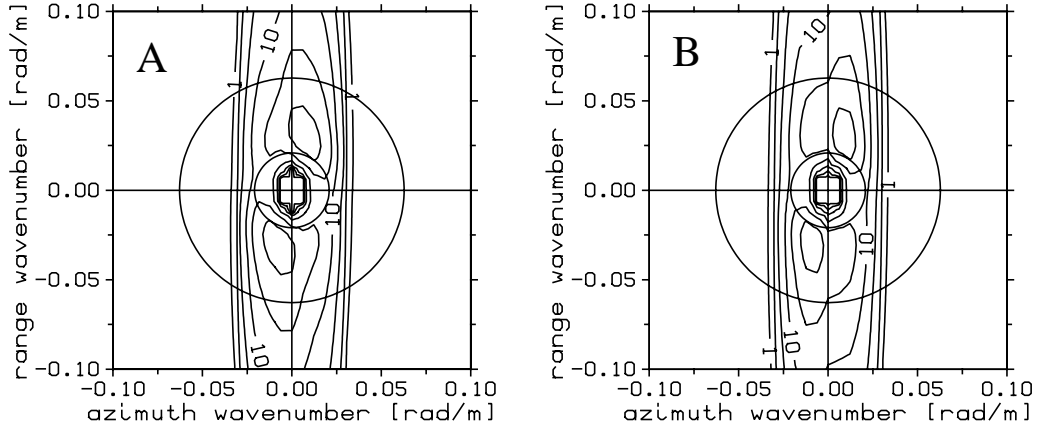


Fig. 4.6: (A) Modulus of cross spectrum simulated with the transform eq. 4.25, which is based on the linear model for the RAR image, using the JONSWAP spectrum shown in Fig. 4.3 (C) as input. (B) The same as (A), but using the modified integral transform eq. 4.33, which avoids the occurrence of negative NRCS values.

Here, we have used that

$$\langle \mathbf{X} \rangle = \mathbf{0} \quad . \quad (4.41)$$

Inserting eq. 4.40 into eq. 4.33 yields the nonlinear transform for the look cross spectrum based on the nonlinear RAR model.

Expanding the \mathbf{x} dependent part of G to first order with respect to the wave spectrum F yields a quasi-linear transform analogue to eq. 4.31

$$\Phi_k^{I^1 I^2} = 0.5 \exp[\alpha_2^2 \rho^{II}(\mathbf{0}, 0) - \beta^2 k_x^2 \rho^u(\mathbf{0})] \left(|T_k^S|^2 F_k + |T_{-k}^S|^2 F_{-k} \right) \quad (4.42)$$

with modified SAR transfer function

$$T_k^S = \alpha_1 (\alpha_2 T_k^R - i k_x \beta T_k^u) \quad . \quad (4.43)$$

Here, α_1, α_2 are functions of the RAR variance $\rho^{II}(0)$ (compare eqs. 4.13, 4.12).

The transform eq. 4.33 can be computed numerically using the following expansion

$$\begin{aligned} \Phi_k^{I^1 I^2} &= \frac{\alpha_1^2}{4 \pi^2} \exp[\alpha_2^2 \rho^{II}(\mathbf{0}, 0) - \beta^2 k_x^2 \rho^u(\mathbf{0})] \\ &\sum_{n=0}^{\infty} \sum_{j=0}^n \frac{(i \alpha_2)^j (\beta k_x)^{n+j}}{j! (n-j)!} Z_{j,n} \quad , \end{aligned} \quad (4.44)$$

with functions Z defined as

$$\begin{aligned} Z_{j,n} &= \int \exp[\alpha_2^2 \rho^{II}(\mathbf{x}, \Delta t)] \left(\rho^{Iu}(\mathbf{x}, \Delta t) - \rho^{Iu}(-\mathbf{x}, -\Delta t) \right)^j \\ &\cdot \left(\rho^{uu}(\mathbf{x}, \Delta t) \right)^{n-j} \exp[-i \mathbf{k} \cdot \mathbf{x}] \, d^2 x \quad , \end{aligned} \quad (4.45)$$

which can be computed efficiently using FFT methods.

Fig. 4.6 shows a comparison of the look cross spectrum real part computed with the transform eq. 4.25 (A) and eq. 4.33 (B) respectively using the JONSWAP spectrum in Fig. 4.3 (C) as input. The TerraSAR configuration is assumed in the simulation. It can be seen that the overall shape and energy levels of the spectrum are maintained. However, there are some obvious differences in the exact shape of the spectral peaks.

In conclusion one can say that for the ERS SAR and the ENVISAT ASAR the described shortcoming of the linear RAR model eq. 4.4 is tolerable at least for moderate sea states. The change of the SAR cross spectrum using the nonlinear RAR model eq. 4.10 is negligible if the overall uncertainties in the RAR model are taken into account. However, for high resolution systems like TerraSAR the linear model should be replaced in order to avoid artefacts caused by unrealistic distributions of image intensities.

4.3.3 Azimuthal cut-off

Finally, we return to the standard imaging theory as described in Section 4.3 and explain a SAR ocean wave imaging characteristic, which will be used in Chapter 7.

As could be seen in Fig. 4.5, an important feature of the SAR ocean wave imaging process is a low pass filtering of the image spectrum in the azimuth direction. On one hand the azimuthal cut-off leads to obvious information loss on shorter waves travelling in the flight direction, on the other hand the width of the cut-off contains valuable information about the orbital velocity variance $\rho^{uu}(0)$ caused by all ocean wave components together. This will fact will be used in Chapter 7 to measure damping of waves by sea ice.

The theoretical cut-off wavelength is given by [Mastenbroek and de Valk, 2000; Kerbaol et al., 1998]

$$\lambda_{cut} = 2\pi \sqrt{\left(\frac{R}{V}\right)^2 \rho^u(\mathbf{0}) + \frac{\hat{\rho}_a^2}{4\pi^2}} \quad (4.46)$$

with $\hat{\rho}_a$ as defined in eq. 4.20. The dependence of λ_{cut} on coherence time and orbital velocity variance for the ERS SAR and ENVISAT ASAR configuration is shown in Fig. 4.7 assuming an azimuthal resolution ρ_a of 20 m and respective integration time of 0.33 s, which represents the ERS SAR case if a look with half bandwidth is used. The plot is shown for half bandwidth looks, because a technique to estimate the cut-off, which is based on the multi-look technique is introduced in Chapter 7.

As can be seen, the dependence of λ_{cut} on coherence time τ_s is weak given the indicated coherence times for C-band radar and wind speeds of 5, 10 and 15 ms⁻¹ (compare table 4.1). The dependence of λ_{cut} on coherence time is stronger for airborne SAR as the R over V ratio is usually smaller in that case [Vachon et al., 1993].

4.4 Linear inversion

The chapter is closed with a simple linear inversion scheme, which will be applied to the data introduced Chapter 5 for a first consistency check. As the scheme has the SAR look cross spectrum as the only input, it is necessarily restricted to the low frequency part of the spectrum as explained in the previous sections. The objective

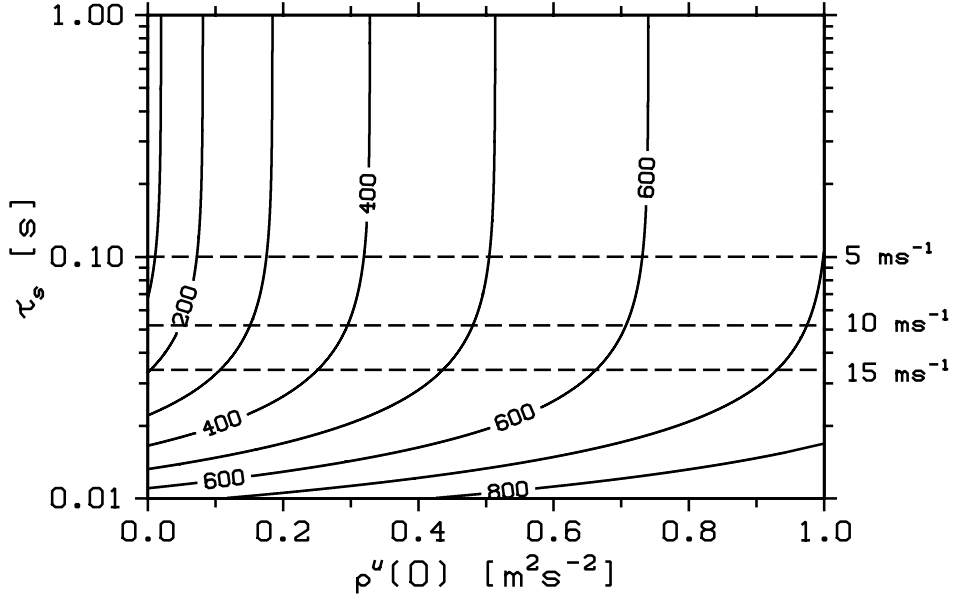


Fig. 4.7: Theoretical cut-off wavelength λ_{cut} (compare eq. 4.46) depending on coherence time τ_s and orbital velocity variance $\rho^u(0)$. The dashed lines represent coherence times for different wind speeds as given in *Milman et al.* [1993] for C-band radar.

is to have a simple analytical tool to analyse the ocean wave information contained in SAR look cross spectra. The method was particularly helpful in sorting out problems with regard to the processing of the first global data set of cross spectra. A more sophisticated scheme, which takes into account nonlinear effects and also deals with the azimuth cut-off problem will be presented in Chapter 9.

A simple inversion approach is to search for a wave spectrum, which minimises the cost function

$$J(F) = \int |\Phi_k^{sim} - \Phi_k^{obs}|^2 dk \quad (4.47)$$

under the side condition

$$F_k \geq 0 \quad . \quad (4.48)$$

Here, Φ^{sim} is the simulated and Φ^{obs} is the observed look cross spectrum. Using the linear forward model eq. 4.29 to describe the imaging process, it is straightforward to show that the free solution \bar{F} , i.e. neglecting the side condition eq. 4.48 is given by [Schulz-Stellenfleth and Lehner, 2000]

$$\bar{F}_k = \frac{\sin(\omega \Delta t) \operatorname{Re} \Phi_k^{I^1 I^2} + \cos(\omega \Delta t) \operatorname{Im} \Phi_k^{I^1 I^2}}{|T_k^S|^2 \cos(\omega \Delta t) \sin(\omega \Delta t)} \quad . \quad (4.49)$$

In fact, for this solution one has

$$J(\bar{F}) = 0 \quad . \quad (4.50)$$

In case the free solution has negative energy components for either \bar{F}_k or \bar{F}_{-k} , the least squares solution is obtained by orthogonal projection of the observed cross spectrum onto the set of feasible solutions as indicated in Fig. 4.8. As the wave

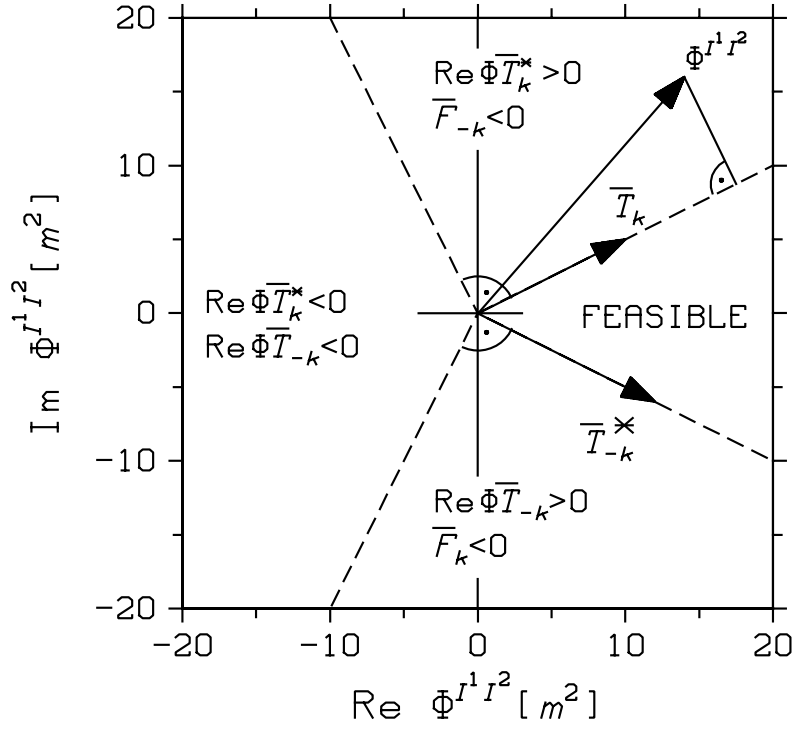


Fig. 4.8: Illustration of the sign condition $F_k \geq 0$ to be taken into account in the linear cross spectra inversion. In case the measured cross spectrum lies outside the feasible regime the free solution for the wave spectrum \bar{F} (compare eq. 4.49) has negative energy values. A least square solution is then found by the projection of the observation onto the set of feasible cross spectra components. The transfer function \bar{T} is defined in eq. 4.51.

components are decoupled in the linear forward model this approach minimises the cost function eq. 4.47. The transfer function \bar{T} indicated in Fig. 4.8 is defined as:

$$\bar{T}_k = 0.5 \exp(i \omega \Delta t) |T_k^S|^2 \quad (4.51)$$

As can be seen, one has to distinguish between the following three cases corresponding to the different regimes indicated in Fig. 4.8:

$$F_k = \begin{cases} \bar{F}_k & : \bar{F}_k \geq 0 \wedge \bar{F}_{-k} \geq 0 \\ 2 |T_k^S|^{-2} \operatorname{Re} \left(\exp(-i \omega \Delta t) \Phi_k^{I^1 I^2} \right) & : \operatorname{Re} \left(\Phi_k (\bar{T}_k)^* \right) \geq 0 \wedge \bar{F}_{-k} < 0 \\ 0 & : \operatorname{Re} \left(\Phi_k (\bar{T}_k)^* \right) < 0 \wedge \operatorname{Re} \left(\Phi_k (\bar{T}_{-k}) \right) < 0 \end{cases}$$

Results obtained by applying the above scheme to ERS-2 wave mode data are presented in Chapter 8.

Chapter 5

DESCRIPTION OF DATA

In this chapter different types of SAR and numerical model data used in the thesis are introduced. In the first part ERS-2 data acquired in wave mode and full swath mode are described. The wave mode data set used in this study is not an official ESA data product and therefore requires a more detailed introduction. Finally, information is given about ocean wave model data used for comparison with ERS-2 SAR data in Chapter 8 and used as prior information for the retrieval scheme presented in Chapter 9.

5.1 ERS SAR data

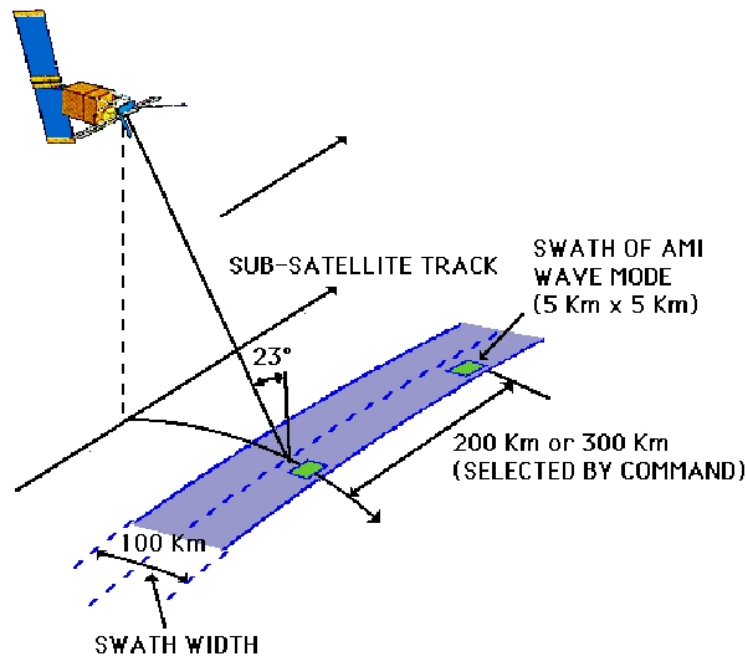


Fig. 5.1: Imaging geometry of the ERS-2 SAR in wave mode and full swath mode.

The SAR data used in this study were acquired by the European remote sensing satellite ERS-2, which was launched in 1995. The ERS-2 has a sun-synchronous orbit with an inclination of 21° , which permits data acquisitions up to 82° N/S latitude. The SAR onboard ERS-2 can be operated in two different modes, which

Parameter	Value
Radar frequency	5.300 GHz
Radar wavelength	5.7 cm
Polarisation	VV
Flight altitude	800 km
Velocity	7 km s ⁻¹
Orbit period	100 min
Azimuth resolution	≈ 5 m
Slant range resolution	≈ 10 m
PRF	1656 Hz
Antenna size	10 by 1 m
Range bandwidth	15.5 MHz
Azimuth bandwidth	1378 Hz
Look direction	right looking
Integration time (processed)	0.66 s

Tab. 5.1: General parameters of the ERS-2 SAR.

can be selected on demand (compare Fig. 5.1). The general technical parameters of the ERS-2 SAR are summarised in table 5.1. The special characteristics of the two acquisition modes will be explained in the following.

5.1.1 ERS-2 SAR wave mode

Operating in wave mode the ERS-2 provides 10×5 km² SAR images (imagettes) every 200 km along the track (compare Fig. 5.1). The data can be stored on an onboard tape recorder, so that acquisitions are possible independent of receiving stations. According to the standard procedure, the imagettes are processed to SAR image variance spectra at the European Space Agency (ESA) and delivered to users like the ECMWF in near real time. Several studies showing the potential of the standard ESA products for ocean wave measurements have been performed [Heimbach *et al.*, 1998; Mastenbroek and de Valk, 2000; Breivik *et al.*, 1998]. The main wave mode parameters are summarised in table 5.3.

The wave mode data presented in this study are not an ESA standard product, but were reprocessed from raw data using the DLR BSAR processor [Breit *et al.*,

Period	number	data volume
Aug 21, 1996 - Sep 9, 1996	26164	96 GB
Oct 4, 1996 - Oct 9, 1996	6594	26 GB
June 1, 1997 - June 2, 1997	1630	6 GB
27 days	34388	128 GB

Tab. 5.2: Periods of the reprocessed complex ERS-2 wave mode imagettes available for the study.

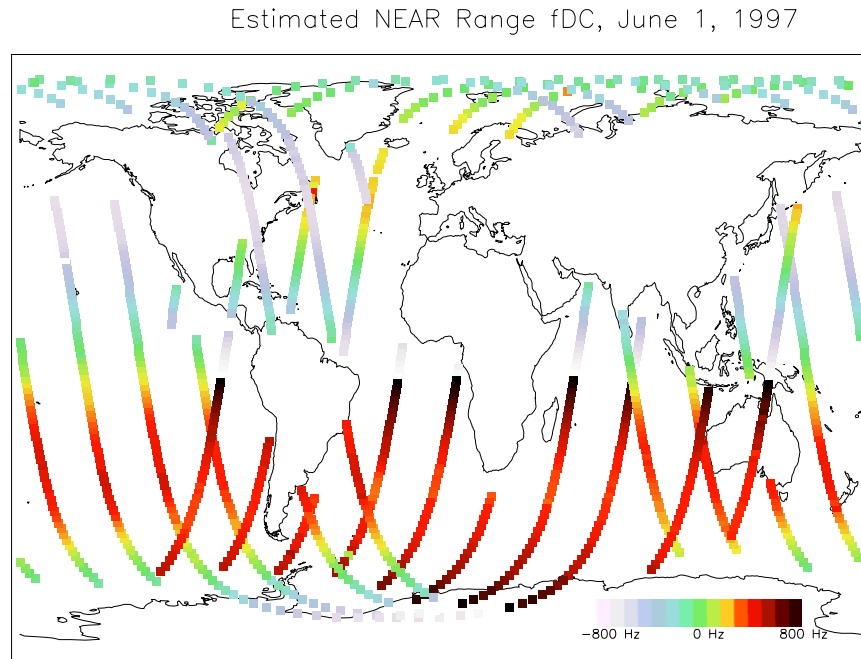


Fig. 5.2: Base band estimates of the Doppler centroid frequency f_{dc} for a global ERS-2 imager data set acquired on June 1, 1997, reprocessed with the DLR BSAR processor.

1997]. They represent the first global data set of complex wave mode imagerettes and thus allow a global statistical analysis of the cross spectra technique for the first time. About 35000 complex ERS-2 imagerettes with the exact periods summarised in table 5.2 are available up to now.

Details of the wave mode processing are given in [Lehner *et al.*, 2000]. The main adjustments required to apply the BSAR processor to wave mode data are as follows:

- An important extension to BSAR for complex wave mode data processing was the incorporation of a range-expansion step. Since BSAR uses the chirp-scaling algorithm [Raney *et al.*, 1994; Breit *et al.*, 1997], the on-board range-compressed wave mode data have to be expanded into chirp raw data required as input for the chirp-scaling algorithm. Moreover, the ERS on-board range compression, achieved by a dispersive surface acoustic wave delay line, causes an additional range time delay with respect to the ERS image mode, which has to be taken into account [Lehner *et al.*, 2000].
- Although several Doppler ambiguity resolving algorithms exist, which deal with low contrast scenes [Bamler, 1991; Bamler, 1993; Wong and Cumming, 1996], they usually require a significant amount of SAR signal samples to be analysed, exceeding by far the ERS wave mode cell size of about 2400 range lines with 528 range-compressed samples each. An analysis of about 25000 ERS-1 and 6000 ERS-2 SAR image mode products produced at the German PAF showed that the ERS image mode Doppler values obtained during the nominal ERS operation in yaw-steering mode (i.e. manoeuvre situations excluded), follow a nominal behaviour around an orbit [Lehner *et al.*, 2000]. Therefore, a Doppler

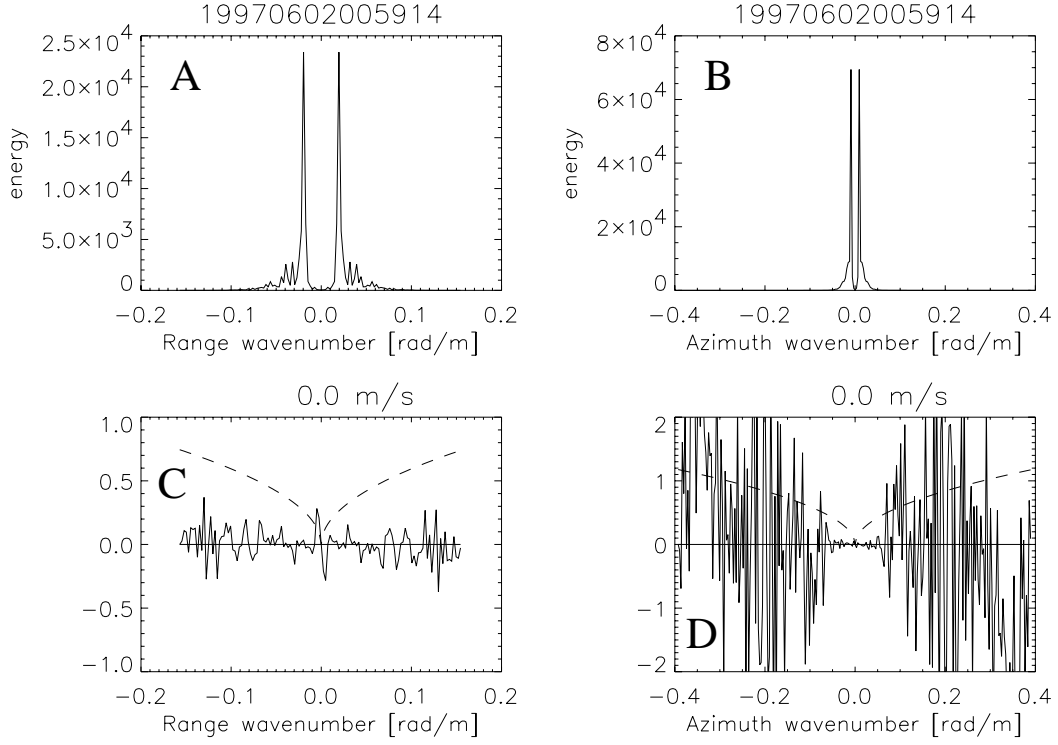


Fig. 5.3: Test of wave mode processing using an imagette acquired over land. The variance spectra in range and azimuth are shown in (A) and (B). The corresponding cross spectra phases are given in (C) and (D). The dashed lines indicate the expected phases for ocean waves (in deep water).

prediction table containing the expected Doppler value in dependence of the geographical latitude for ascending and descending orbits was incorporated into BSAR and used for the Doppler ambiguity resolving.

As an illustration of the last point, Fig. 5.2 shows the base bands estimates of the Doppler centroid for imagettes acquired on Sep 5, 1996. As one can see, f_{dc} is shifted into adjacent PRF bands at several locations. If this effect is not taken into account, i.e. the base band values as given in Fig. 5.2 are used for the processing, the resulting imagettes are strongly defocused. The effect was first detected by a simple test based on the computed look cross spectrum of imagettes acquired over land. In the case of accurate processing, the land should be stationary and thus the imaginary part of the cross spectrum is expected to be zero. For a better visualisation, the test is performed both in range and azimuth direction separately. For this purpose a one-dimensional range cross spectrum

$$\Phi^y = \int \Phi_k^{I^1 I^2} dx \quad (5.1)$$

and azimuth cross spectrum

$$\Phi^x = \int \Phi_k^{I^1 I^2} dy \quad (5.2)$$

is defined by integrating over the azimuth and range dimension x and y respec-

Parameter	Full swath	Wave mode
Pixel size slant range	7.9 m	7.9 m
Pixel size azimuth	4 m	4 m
Incidence angles	20.1° -25.9°	23.5° (since June 1995)
Image size azimuth	100 km	5 km
Image size range	100 km	10 km
I/Q quantisation	5 bit/5 bit	4 bit/4 bit

Tab. 5.3: Technical parameters of the ERS-2 SAR full swath mode and wave mode.

tively. Fig. 5.3 shows the phases of these spectra together with the respective one-dimensional image variance spectra for the imagette shown in Fig. 5.4 (B), which was acquired over Australia. The f_{dc} prediction table as described above was used to resolve the PRF ambiguity in this case. The dashed lines indicate the phase expected for ocean waves in deep water. As one can see, the phase is in fact negligible at least in the spectral regime with significant spectral energy in the image. For wavenumbers with low spectral energy the respective cross spectrum phase is strongly affected by noise. A detailed explanation of this effect will be given in Chapter 6.

The system transfer function for the reprocessed data was estimated using homogeneous imaggettes acquired over continental ice. Fig. 5.4 (A) shows an imagette acquired over Antarctica on Sep 7, 1996. The respective cuts through the variance spectrum in the range and azimuth direction are shown in Fig. 5.4 (C) and (D). The horizontal line indicates the theoretical speckle noise level Φ_k^S as given by eq. 3.40. One can see, that the transfer function is reasonably constant for wavelengths longer than 100 m ($\approx 0.06 \text{ rad s}^{-1}$), which is the important regime for typical SAR wave measurements.

A comparison of the UWA spectrum, which is the ESA wave mode standard product, and the reprocessed data is shown in Fig 5.5. The intensity of an imagette (A) acquired on Sep 1, 1996 at N 34.71°, W 22.92° is given together with the respective UWA spectrum (B) and the corresponding real part (C) and imaginary part (D) of the cross spectrum as derived from the reprocessed complex data. The cross spectrum is given on the polar grid, which is used for the standard ENVISAT ASAR wave mode product.

5.1.2 ERS SAR full swath mode

Operating in full swath mode, the ERS-2 SAR scans a swath of 100 km width (compare Fig. 5.1). The resulting standard ESA products are SAR images of 100 by 100 km size. In contrast to wave mode data, full swath scenes can only be acquired when receiving stations are in line of sight. The full swath acquisition time is limited to 12 minutes per orbit. Full swath mode specific imaging parameters are summarised in table 5.3.

The ERS scenes used in this study were acquired over the marginal ice zone of the Greenland Sea and the Weddell Sea. The data were downlinked to the respective receiving stations in Kiruna (Sweden) and O'Higgins (Antarctica).

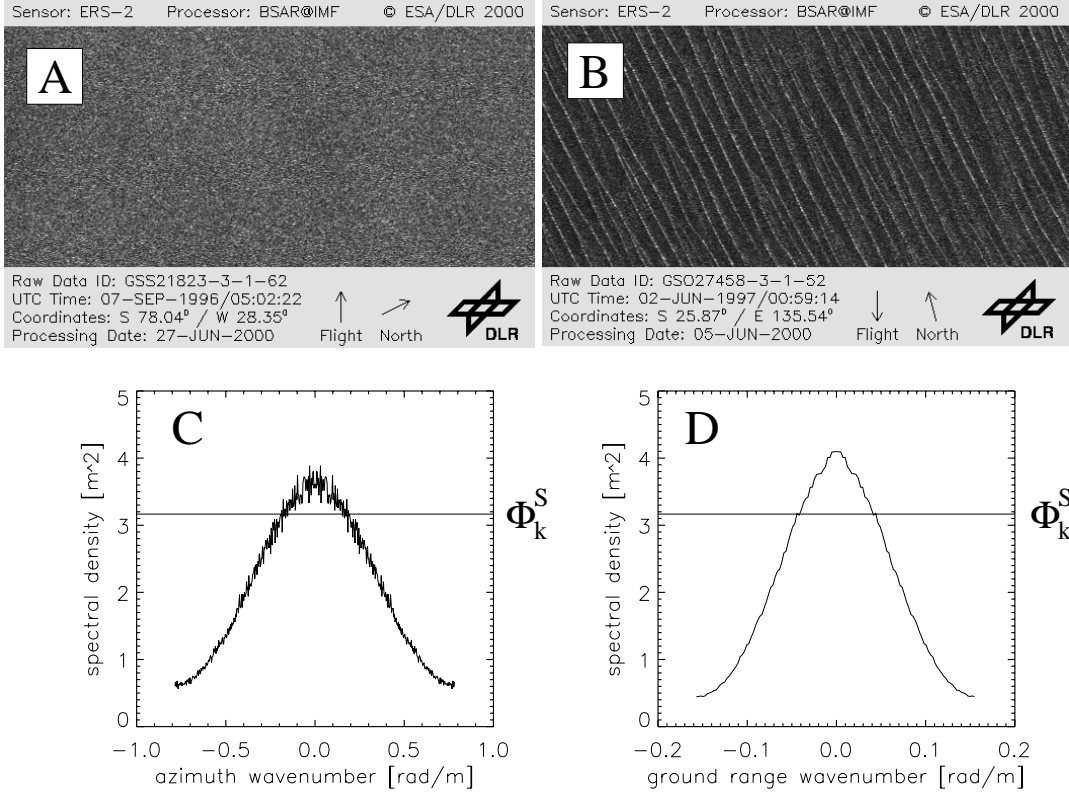


Fig. 5.4: Cut in range (C) and azimuth (D) direction through the speckle variance spectrum of the homogeneous ERS-2 wave mode imagerette (SLC) shown in (A) acquired over continental ice in Antarctica. The horizontal line represents the speckle noise level calculated according to eq. 3.40. The image shown in (B) was acquired over Australia.

5.2 Wave model data

In this thesis two types of wave model data are used. For the analysis of the reprocessed imagerette data set, collocated two-dimensional wave spectra were provided by the ECMWF. The data are standard output from the operational WAM model runs performed at ECMWF at the four synoptical hours 00:00, 06:00, 12:00, and 18:00 UTC. The temporal gap between WAM and SAR measurement is thus less than 3 hours. The model is driven by U_{10} wind fields computed with the atmospheric general circulation model (AGCM). The operational WAM model was run with a $1.5^\circ \times 1.5^\circ$ latitude-longitude grid. The collocation distance to the ERS-2 imagerettes is thus less than 0.75° . The internal time step of the model is 20 minutes.

The wave model data are given on a polar grid with 30° directional resolution and 25 frequencies with logarithmic spacing according to

$$f_i = f_0 1.1^i \quad i = 0, \dots, 24 \quad (5.3)$$

with lowest frequency bin f_0 given by

$$f_0 = 0.04177 \text{ Hz} \quad (5.4)$$

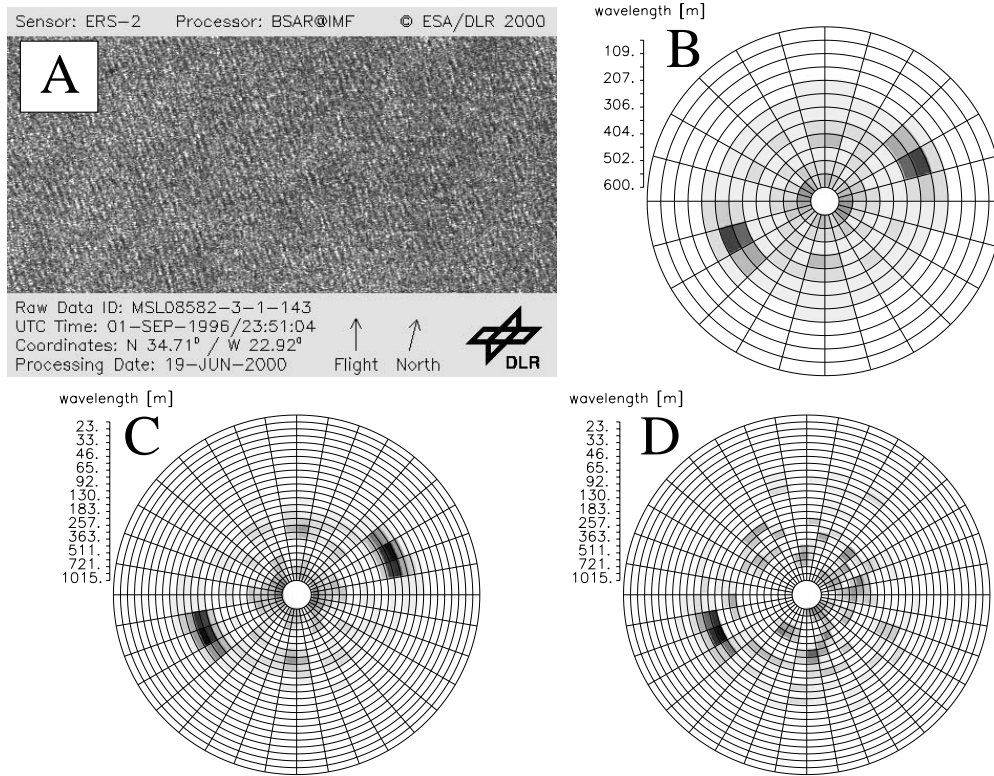


Fig. 5.5: (A) ERS-2 wave mode imagette (intensity) acquired on Sep 1, 1996 at 34.71°N , 22.92°W showing ocean waves. (B) Standard ERS-2 UWA spectrum computed from the imagette shown in (A). (C,D) Real part (C) and imaginary part (D) of the look cross spectrum computed from the respective complex imagette, which was processed with the DLR BSAR processor. The cross spectrum is shown on the polar grid, which is used for the standard ENVISAT wave mode product.

For deep water, these frequencies correspond to wavelengths between 9 m and 895 m.

For the analysis of ocean waves travelling into sea ice presented in Chapter 7, dedicated WAM model runs [WAMDI Group, 1988] were performed for the Atlantic. The WAM model was set up on a 1° grid using analysed ECMWF wind fields (e.g. with scatterometer data assimilated) as input.

Chapter 6

DISTRIBUTION OF THE ESTIMATED LOOK CROSS SPECTRUM

In this chapter a noise model for estimated SAR look cross spectra acquired over the ocean is presented, which was first introduced in *Schulz-Stellenfleth et al.* [2002]. The investigation is meant to contribute to a better understanding and quantification of the information contained in look cross spectra used for ocean wave measurements, which are now becoming available from the new satellite ENVISAT on an operational basis. The analysis has the following main objectives:

- Derive error bars for the estimated cross spectrum phase as well as the real and imaginary part.
- Identify the dominant factors in the estimation uncertainty, taking into account parameters of both the SAR system and the underlying ocean wave field.
- Use the derived model to optimise parameters like look separation time.

The analysis is based on a simple second order statistical model for the joint distribution of the discrete complex look spectra (compare eq. 3.26). The investigation uses results presented in *Tough et al.* [1995], where the same model was applied in

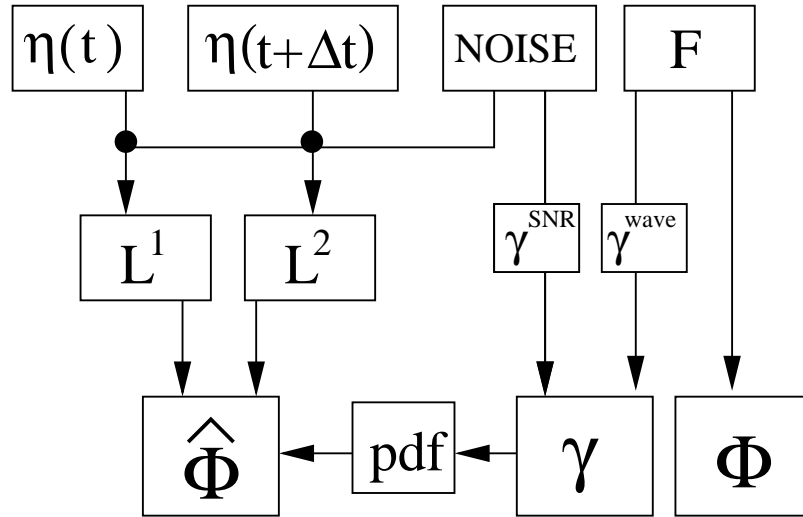


Fig. 6.1: Diagram illustrating the relationship between the sea surface elevation field η , the SAR looks L^1, L^2 , the estimated cross spectrum $\hat{\Phi}$, the ocean wave spectrum F , the expected cross spectrum Φ , the coherence γ , and the SAR speckle noise.

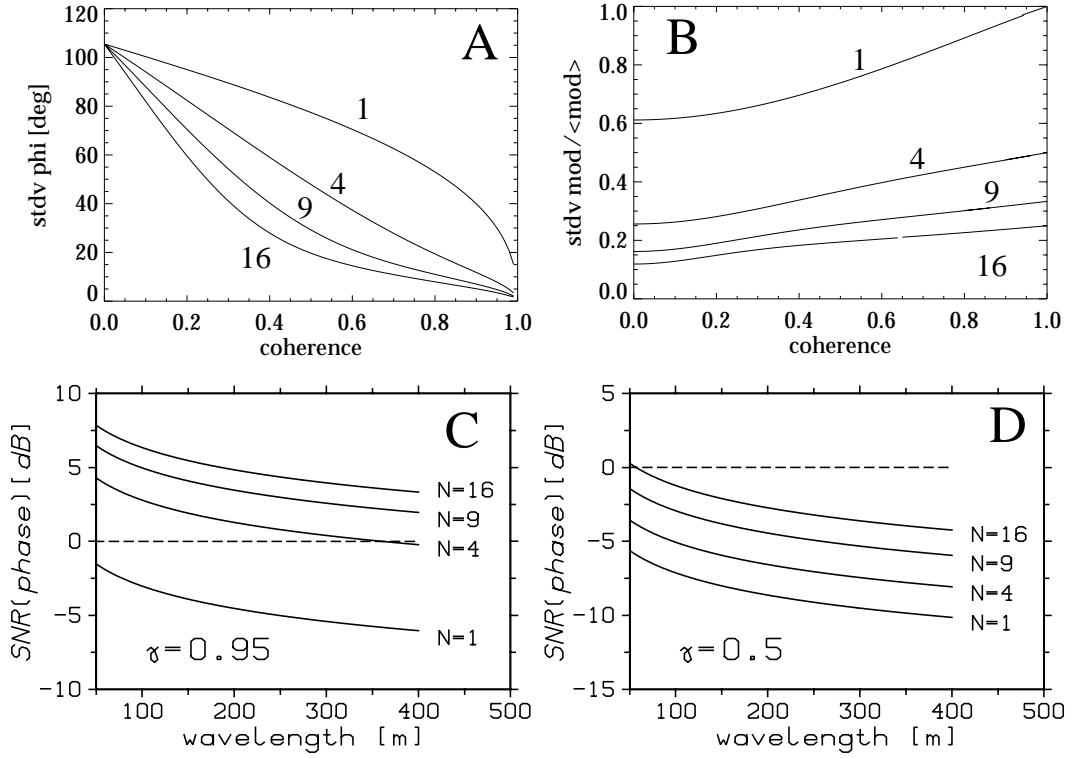


Fig. 6.2: (A) Standard deviation of the cross spectrum phase estimated by averaging $N=1,4,9,16$ complex samples. (B) The same as (A) for the normalised cross spectrum magnitude. (C,D) Theoretical signal to noise ratio of the cross spectrum phase as a function of wavelength for a coherence of $\gamma = 0.95$ (C) and $\gamma = 0.5$ (D). Deep water and a look separation time of $\Delta t = 0.33$ s is assumed.

a different context to describe phase statistics in SAR interferometry. A diagram illustrating the different components in the model is given in Fig. 6.1.

The chapter is structured as follows: First of all, the basic model is introduced, which has the cross spectrum coherence as a key parameter. Based on this model error estimates for the cross spectrum phase are given depending on coherence and the number of averaged samples used to estimate the cross spectrum. In the second step a product model is introduced, which relates the coherence to SAR system parameters like resolution as well as to the underlying ocean wave spectrum. The model enables the simulation of the phase statistics using a nonlinear integral transform to describe the ocean wave related decorrelation effect. Finally, the model is applied to optimise the look separation time.

6.1 A statistical model for the estimated cross spectrum

In this section a noise model for estimated look cross spectra is introduced. The model describes the statistics of an assemble of look cross spectra, which are generated by:

- Different realisations of the ocean surface for a fixed ocean wave spectrum.

- Different realisations of SAR image speckle.

The noise model is based on assumptions about the discrete complex spectrum of the two looks. It is assumed that both discrete look spectra \hat{I}_k^1, \hat{I}_k^2 (eq. 3.26) are circular Gaussian processes with identically distributed and independent real and imaginary part. These properties can be justified by looking at the equivalent properties of the corresponding phase and intensity:

- According to standard theory, the phase of the spectral components of the ocean wave field is uniformly distributed [Komen *et al.*, 1994]. It is therefore reasonable to assume that the phase of the complex Fourier spectra of the two looks are uniformly distributed, too.
- The squared magnitude of a circular Gaussian process has a negative exponential distribution. This is exactly what we expect for the periodogram, i.e. the squared magnitude of \hat{I}_k according to standard estimation theory [Honerkamp, 1993].

A simple second order model, which reproduces both properties, at the same time introducing a correlation between the two complex spectra \hat{I}_k^1, \hat{I}_k^2 is given by the following probability density function (pdf) [Tough *et al.*, 1995; Bamler and Hartl, 1998]

$$\text{pdf}\left[\begin{pmatrix} \hat{I}_k^1 \\ \hat{I}_k^2 \end{pmatrix}\right] = \frac{1}{\pi^2 |C_k|} \exp\left[-\begin{pmatrix} \hat{I}_k^1 \\ \hat{I}_k^2 \end{pmatrix}^{*T} C_k^{-1} \begin{pmatrix} \hat{I}_k^1 \\ \hat{I}_k^2 \end{pmatrix}\right] \quad , \quad (6.1)$$

with covariance matrix C_k given by

$$C_k = \begin{pmatrix} \langle |\hat{I}_k^1|^2 \rangle & \gamma_k \sqrt{\langle |\hat{I}_k^1|^2 \rangle \langle |\hat{I}_k^2|^2 \rangle} \\ \gamma_k^* \sqrt{\langle |\hat{I}_k^1|^2 \rangle \langle |\hat{I}_k^2|^2 \rangle} & \langle |\hat{I}_k^2|^2 \rangle \end{pmatrix} \quad (6.2)$$

and coherence γ_k defined as

$$\gamma_k = \frac{\langle \hat{I}_k^1 (\hat{I}_k^2)^* \rangle}{\sqrt{\langle |\hat{I}_k^1|^2 \rangle \langle |\hat{I}_k^2|^2 \rangle}} \quad . \quad (6.3)$$

In the framework of look cross spectra acquired over the ocean we can assume $\langle |\hat{I}_k^2|^2 \rangle = \langle |\hat{I}_k^1|^2 \rangle$ as explained in Chapter 3.

Depending on the coherence γ_k and the number of averaged periodograms, probability density functions can be derived [Tough *et al.*, 1995] for the real and imaginary part as well as the phase and magnitude of the cross spectrum estimator given in eq. 3.28. Analytical expressions for the pdfs can be found in Appendix A. Fig. 6.2 shows the standard deviations of phase (A) and normalised magnitude (B) of the estimator (eq. 3.28) as a function of coherence for different numbers of averaged cross periodograms. For example, one can see that a coherence of more than 0.9 is required if the standard deviation is supposed to be less than 40° in case no averaging is performed at all. The respective signal to noise ratio of the phase assuming a linear imaging model and a look separation time of $\Delta t = 0.33$ s is shown in Fig. 6.2 (C) and (D) for a coherence of 0.95 and 0.5 respectively. One can see that even in the case

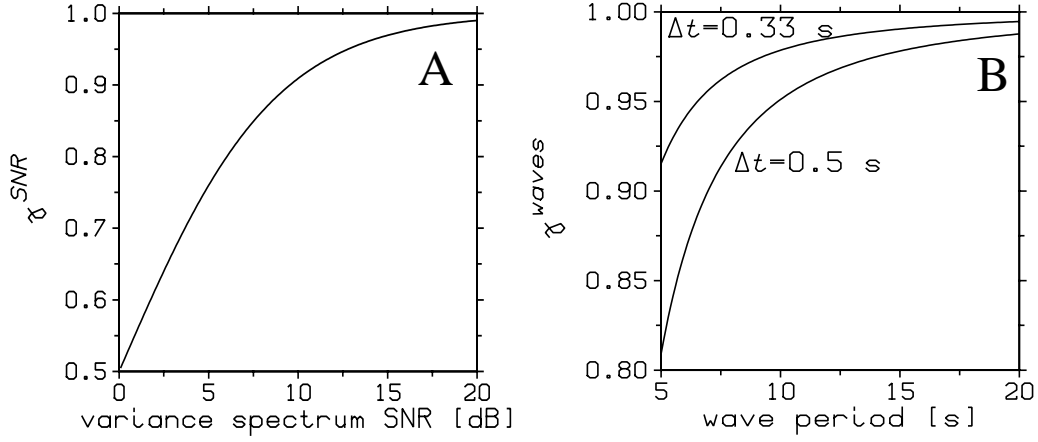


Fig. 6.3: (A) Dependence of the coherence γ^{SNR} on the signal to noise ratio (SNR) of the look variance spectrum SNR_k^{II} . (B) Coherence γ^{waves} in the case of standing waves as a function of wave period for two different look separation times.

of higher coherence smoothing is absolutely necessary to extract useful information from the cross spectrum phase, i.e. to make sure that the signal to noise ratio is above 0 dB.

6.2 A product model for the cross spectrum coherence

In this section a product model is proposed for the look cross spectrum coherence, which was first presented in *Schulz-Stellenfleth et al.* [2002]. The first part of the model describes decorrelation of the look wave patterns due to speckle noise. The second part explains decorrelation caused by wave motion.

As explained in Section 3.4, the first order effect of speckle in the look variance spectrum is an additive noise floor, i.e. for both looks one has

$$\langle |\tilde{I}_k|^2 \rangle = \Phi_k^{II} + \Phi_k^S, \quad (6.4)$$

where \tilde{I}_k is the estimated Fourier spectrum of the speckled looks and Φ^{II} is the variance spectrum of the noise-free looks. The coherence for the speckled images can then be written as

$$\gamma_k = \frac{\langle \tilde{I}_k^1 (\tilde{I}_k^2)^* \rangle}{\Phi_k^{II} + \Phi_k^S} = \frac{\Phi_k^{I^1 I^2}}{\Phi_k^{II} + \Phi_k^S}, \quad (6.5)$$

where we have used that the speckle noise cancels out in the cross spectrum as explained in Section 3.4. The last expression can be factored as

$$\gamma_k = \gamma_k^{SNR} \gamma_k^{waves} \quad (6.6)$$

with the factor γ_k^{SNR} describing the (non-coherent) impact of speckle noise defined as

$$\gamma_k^{SNR} = \frac{\Phi_k^{II}}{\Phi_k^{II} + \Phi_k^S} =: \frac{1}{1 + (SNR_k^{II})^{-1}}. \quad (6.7)$$

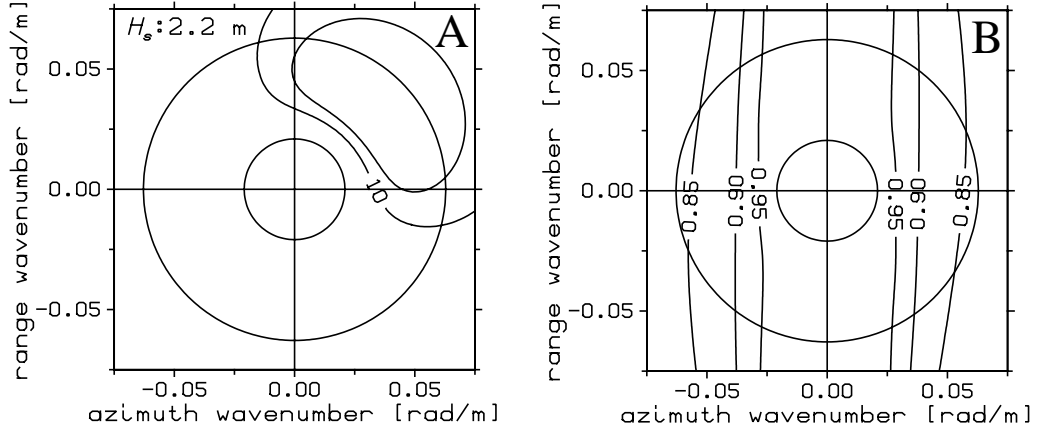


Fig. 6.4: (A) JONSWAP ocean wave spectrum representing a fully developed wind sea of 100 m length. (B) Simulated cross spectrum coherence γ^{waves} associated with the nonlinear SAR wave imaging mechanism.

Here, SNR^{II} is the signal to noise ratio in the look variance spectrum given by

$$\text{SNR}_k^{II} = \frac{\Phi_k^{II}}{\Phi_k^S} . \quad (6.8)$$

Fig. 6.3 (A) shows the dependence of γ^{SNR} on SNR_k^{II} . One can see that a signal to noise ratio of at least 10 dB is required to achieve a coherence of 0.9. The second factor γ^{waves}

$$\gamma_k^{waves} = \frac{\Phi_k^{I^1 I^2}}{\Phi_k^{II}} \quad (6.9)$$

describes the decorrelation effects associated with the motion of the sea surface. It has a complicated dependence on the ocean wave spectrum as explained in the next section.

6.3 Dependence of coherence on the ocean wave spectrum

In this section the dependence of γ^{waves} on the ocean wave spectrum is analysed. Using the forward model, which relates the ocean wave spectrum F to the SAR cross spectrum $\Phi^{I^1 I^2}$ derived in *Engen and Johnson* [1995] for the nominator in eq. 6.9 and the respective model for the SAR image variance spectrum developed in *Hasselmann and Hasselmann* [1991] for the denominator, one obtains a nonlinear forward model for the cross spectrum coherence

$$F \longrightarrow \gamma^{waves} . \quad (6.10)$$

The SAR image variance spectrum Φ^{II} is a special case of the cross spectrum with identical looks, i.e. zero look separation time Δt , and can therefore be readily calculated using the more general cross spectrum model transform given by eq. 4.25.

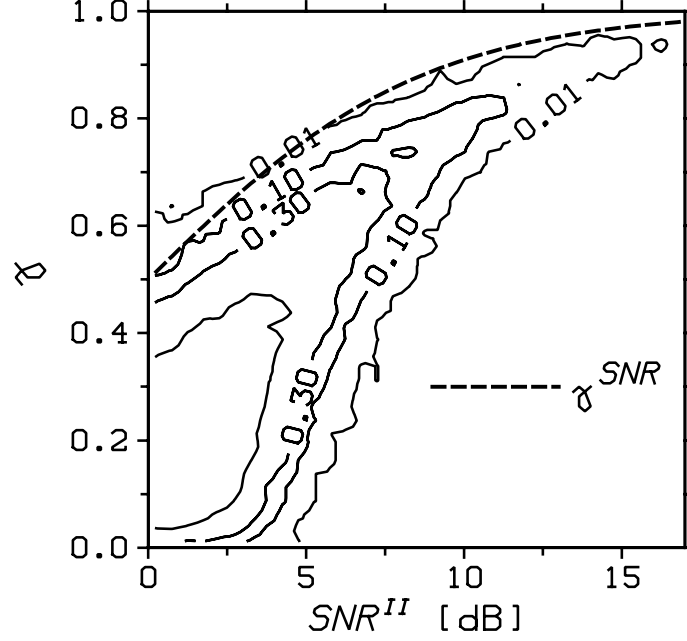


Fig. 6.5: Estimated coherence γ as a function of the signal to noise ratio of the look variance spectrum (compare eq. 6.17) derived from 1000 reprocessed ERS-2 wave mode im-
agettes. The dashed line represents the expected look decorrelation γ^{SNR} associated with speckle noise (compare eq. 6.7).

A first order analysis of the cross spectrum coherence is performed by using a quasi-linear approximation for both the image variance and the cross spectrum (compare eq. 4.31). This approach yields the following expression

$$\gamma_k^{waves}(F, \Delta t) = \frac{\exp(i\omega\Delta t) |T_k^S|^2 F_k + \exp(-i\omega\Delta t) |T_{-k}^S|^2 F_{-k}}{|T_k^S|^2 F_k + |T_{-k}^S|^2 F_{-k}} , \quad (6.11)$$

where T^S is the SAR transfer function as defined in eq. 4.30.

First assume that there are no wave components propagating in opposite direction, e.g. $F_k F_{-k} = 0$. In that case one has

$$|\gamma_k^{waves}| = 1 , \quad (6.12)$$

and hence there is no decorrelation between the looks at all. The other extreme case is $F_k = F_{-k}$, i.e. standing waves. In this situation eq. 6.11 becomes

$$\gamma_k^{waves}(F, \Delta t) \approx \cos(\omega\Delta t) , \quad (6.13)$$

which is an approximation because the SAR transfer function is not exactly symmetric. However, the last relationship shows that waves propagating in opposite

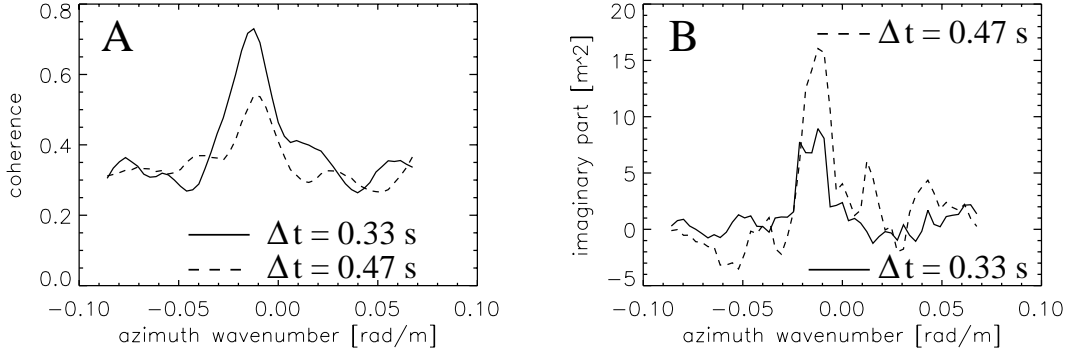


Fig. 6.6: (A) Azimuth cut through the peak of the coherence of the cross spectrum shown in Fig. 3.4 for look separation times of $\Delta t = 0.33$ s and $\Delta t = 0.45$ s. (B) The same as (A) for the imaginary part of the cross spectrum.

directions are one cause of reduced coherence and thus increased uncertainty in the cross spectra estimation. To illustrate the problem, one can for example think of a standing wave, which is imaged exactly at the time when both opposing waves cancel out at the first look, and which become visible a short moment later at the second look. The estimated cross spectrum is zero in this case and thus different to the expected “true” cross spectrum. Fig. 6.3 (B) shows the dependence of γ^{waves} on look separation time Δt in the case of standing waves.

More generally, look decorrelations are caused by the fact that ocean wave components with different phase speeds are coupling in the SAR image formation process. The above standing wave case is an extreme example, where the phase speeds have opposite signs. The more general case is a nonlinear coupling of waves with different wavelengths propagating in the same direction. This effect is illustrated in Fig. 6.4 where a simulation of the coherence γ^{waves} (B) is shown based on a fully developed wind sea spectrum (A) using the nonlinear forward model given by eq. 6.9. As can be seen, the nonlinear SAR imaging mechanism causes loss of coherence in particular for shorter waves propagating the azimuth direction.

As a first check of the noise model, the cross spectrum coherence was estimated for the global data set of reprocessed ERS-2 introduced in Chapter 5. Fig. 6.5 shows a scatter plot of coherence as a function of look variance spectrum SNR derived from cross spectra processed with a look separation time of 0.33 s. The dashed line represents the expected look decorrelation due to speckle noise represented by γ^{SNR} . One can see that the estimated coherence is reasonably close to γ^{SNR} for high signal to noise ratios. The additional decorrelation observed in particular for low signal to noise ratios is attributed to the nonlinear wave imaging process represented by the coherence factor γ^{waves} .

Furthermore, one should take into account that the deterministic relationship between the sea surface elevation and the corresponding radar cross section as given by the RAR model (eq. 4.4) is rather simplistic. More realistically, one would rather assume that the RAR modulation contains stochastic components, e.g. associated with turbulent flow of wind over the waves, which could be an additional factor in

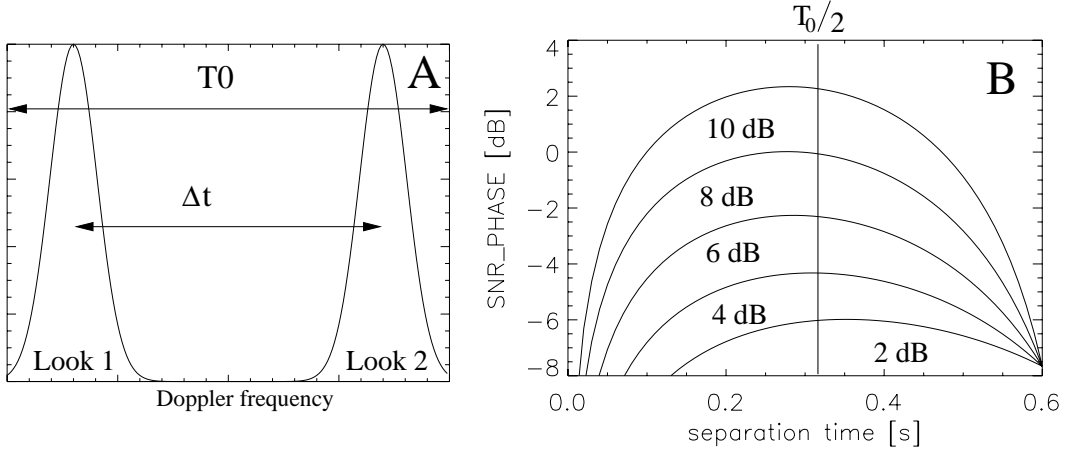


Fig. 6.7: (A) Illustration of the parameter Δt in the look extraction process. (B) Theoretical signal to noise ratios of the cross spectrum phase as a function of look separation time for different signal to noise ratios in the look variance spectrum.

the decorrelation observed in Fig. 6.5.

6.4 Optimal look separation time

In this section a strategy to find an optimal look separation time Δt is discussed using the theory presented above. The study extends the analysis presented in *Bao and Alpers* [1998] in the way that decorrelation effects are taken into account.

As discussed in *Bao and Alpers* [1998], the cross spectrum phase increases with increasing look separation time. This effect is demonstrated in Fig. 6.6, where cuts through the spectral peak of the cross spectrum in Fig. 3.4 are shown for look separation times of 0.33 s and 0.47 s. The imaginary part given in (B) clearly shows the increased signal for the longer separation time. However, due to the limited bandwidth the longer separation time is necessarily associated with a reduced look resolution (compare Fig. 6.7 (A)), which according to eq. 3.40 leads to higher speckle noise levels. The resulting decrease of coherence, which follows from eq. 6.7 is shown in Fig. 6.6 (A), where the coherence is reduced from about 0.75 to 0.55. The optimal choice of a look separation time thus has to be a compromise between the opposing requirements of low noise levels and strong signals.

A natural approach to optimise the look separation time is to maximise the signal to noise ratio of the cross spectrum phase φ , which is given by

$$SNR^\varphi = \frac{\varphi}{\sigma_\varphi}, \quad (6.14)$$

where σ_φ is the phase standard deviation. Neglecting nonlinear effects and discarding the case of wave components travelling in opposite directions one has (compare eq. 4.29)

$$\varphi \approx \omega \Delta t. \quad (6.15)$$

Furthermore, assuming white speckle noise the dependence of the speckle noise level in the look variance spectrum on the separation time is given by (compare Fig. 6.7

(A))

$$\Phi_k^S = \frac{T_0}{T_0 - \Delta t} \frac{\rho_a \rho_r}{4\pi^2} . \quad (6.16)$$

The signal to noise ratio in the look variance spectrum can then be written as

$$\text{SNR}^{II} = \frac{T_0 - \Delta t}{T_0} \text{SNR}_0^{II} \quad (6.17)$$

with SNR_0^{II} representing the look variance spectrum SNR for $\Delta t = 0$, i.e. using the full available bandwidth. For ERS SLC images we have $\rho_a \approx 10$ m and $\rho_r \approx 20$ m. Using the half bandwidth for each look thus yields $\Phi_k^S \approx 10$ m². Under the above assumptions, the dependence of coherence on the look separation time is approximately given by

$$\gamma_k \approx \left(1 + \frac{T_0}{\text{SNR}_0^{II} (T_0 - \Delta t)} \right)^{-1} . \quad (6.18)$$

For a given number of smoothed periodograms, the respective standard deviation of the cross spectrum phase needed in eq. 6.14 follows from the theory presented in the previous sections. For instance, assuming $N = 9$ and a wave period of 12 s the curves shown in Fig. 6.7 (B) represent the cross spectrum phase SNR as a function of look separation time for different values of SNR_0^{II} . One can see that all curves have a well defined maximum around $T_0/2$, which slightly shifts towards shorter separation times with increasing variance spectrum SNR. This finding somehow confirms the intuitive approach to make use of the entire available bandwidth. The cross spectra estimated for the ocean wave measurements presented in Chapter 8 and Chapter 9 are based on looks with half bandwidth as suggested by the above analysis.

The presented analysis should be regarded as a first approach to optimise the look separation time taking into account the effect of look decorrelation. It should be noted that the method can be extended in different ways, e.g. by taking into account that the speckle noise is not exactly white, or by allowing more sophisticated look extraction strategies than defined in Fig. 6.7 (A).

6.5 Distribution of the cross spectrum real and imaginary part

In this section the distribution of the real and imaginary part of the estimated cross spectrum following from the statistical model given by eq. 6.1 are summarised. The results are relevant for the formulation of the cost function, which is basis for the inversion scheme presented in Chapter 9.

It can be shown [Tough *et al.*, 1995] that the mean of the real and imaginary part of the estimated cross spectrum (compare eq. 3.28) is given by:

$$\langle \text{Re} \hat{\Phi}_k^{I_1 I_2} \rangle = \Phi_k^{I_1 I_1} |\gamma_k| \cos \varphi_k^0 \quad (6.19)$$

$$\langle \text{Im} \hat{\Phi}_k^{I_1 I_2} \rangle = \Phi_k^{I_1 I_1} |\gamma_k| \sin \varphi_k^0 \quad (6.20)$$

where φ_k^0 is the mean phase calculated as

$$\varphi_k^0 = \text{Arg}(\Phi_k^{I_1 I_2}) . \quad (6.21)$$

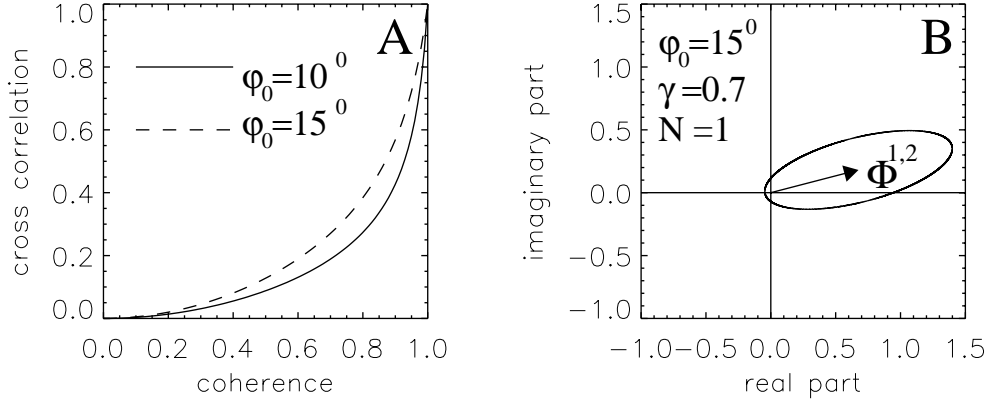


Fig. 6.8: (A) Correlation of real and imaginary part of the cross spectrum as a function of coherence for expected cross spectrum phases of $\varphi_0 = 10^\circ$ and $\varphi_0 = 15^\circ$ (B) Expected deviation from the exact cross spectrum for $N = 1$ (no smoothing), $\gamma = 0.7$, and expected phase $\varphi_0 = 15^\circ$.

Eq. 6.20 and eq. 6.19 show that the cross spectrum estimator (eq. 3.28) is unbiased. The covariance matrix of real and imaginary part is given by [Tough *et al.*, 1995]

$$\text{cov}(\text{Re}\hat{\Phi}_k^{I_1 I_2}, \text{Im}\hat{\Phi}_k^{I_1 I_2}) = \frac{(\Phi_k^{I_1 I_1})^2}{N} \begin{pmatrix} 0.5(1 + |\gamma_k|^2 a_k) & |\gamma_k|^2 b_k \\ |\gamma_k|^2 b_k & 0.5(1 - |\gamma_k|^2 a_k) \end{pmatrix} \quad (6.22)$$

with N denoting the number of averaged cross periodgrams (compare eq. 3.28) and a_k and b_k defined as follows:

$$a_k = \cos^2 \varphi_k^0 - \sin^2 \varphi_k^0 \quad (6.23)$$

$$b_k = \sin \varphi_k^0 \cos \varphi_k^0 \quad (6.24)$$

Fig. 6.8 (A) shows the resulting correlation of the real and imaginary part of the cross spectrum as a function of coherence for expected cross spectrum phases of $\varphi_k^0 = 10^\circ$ and $\varphi_k^0 = 15^\circ$, which are typical values (compare Fig. 3.5 (B)). As one can see the correlation is relatively small (< 0.5), for the majority of cases, which have a coherence of less than 0.8 (compare Fig. 6.5).

Chapter 7

SAR OBSERVATIONS OF OCEAN WAVES TRAVELLING INTO SEA ICE

In this chapter damping of ocean waves by sea ice is studied using complex ERS SAR data acquired in full swath mode. The main results of the analysis were presented in *Schulz-Stellenfleth and Lehner* [2002].

Sea ice covers an area which encompasses about two-thirds of the permanent global ice cover. It is an important factor in the climate system [*Hartmann, 1994; Wadhams, 2000*], as it has a strong impact on the albedo, the atmosphere-ocean heat and momentum exchange, and the oceanic salt flux. It plays an important role in shipping and offshore operations in the polar regions as well [*Johannessen et al., 1995*].

Sea ice responds sensitively to small changes of the oceanic or atmospheric conditions and is therefore a valuable indicator for climate change [*Wadhams, 2000*]. Therefore, continuous measurements of sea ice parameters like ice thickness and ice concentration is an urgent need for scientists as well as for mariners.

The work presented in this chapter is concerned with remote sensing of sea ice in the marginal ice zone (MIZ), which is the transition zone between open water and pack ice. Because of the tough environmental conditions in the MIZ, remote sensing is so far the only way to obtain sea ice information on a continuous basis. Due to their all weather capability, microwave sensors like SAR or the radiometer play an important role in this context. Radiometric systems like the Special Sensor Microwave Imager (SSM/I) [*Bjorgo et al., 1997*] with a resolution between 10 and 50 km (depending on frequency) are mainly used to measure sea ice coverage and sea ice type. SAR imagery as acquired by the ERS has a resolution of about 20 m and thus permits studies of processes in the MIZ on a much smaller scale.

In general, the analysis of ocean waves entering sea ice has two facets: the physical effects of waves on an ice cover or vice versa; and the use of waves as a diagnostic tool in ice mechanics. The present study analyses the impact of sea ice on the two-dimensional ocean wave spectrum and is therefore related to the second aspect. The main objectives of the analysis are as follows:

- Interpret observed SAR image spectra acquired in the MIZ based on standard SAR imaging theory, e.g.
 - The spiky appearance of waves within the sea ice.
 - Refraction phenomena at the ice boundary.
- Use SAR observations to measure parameters characterising the sea ice impact on ocean waves.

SAR observations of ocean waves in sea ice have been analysed in several studies [Vachon *et al.*, 1993; Lyzenga *et al.*, 1985; Wadhams and Holt, 1991; Liu *et al.*, 1991a, Liu *et al.*, 1991b] some of them discussing methods to estimate ice parameters [Shuchman and Rufenach, 1994]. Different models were proposed to explain phenomena like wave refraction at the ice edge. Whereas some studies consider hydrodynamic ocean wave sea ice interaction alone [Shuchman and Rufenach, 1994], others also discuss SAR imaging effects [Vachon *et al.*, 1993].

In the first part of the present analysis SAR imaging of waves propagating into sea ice is analysed theoretically. Typical imaging artefacts like spiky wave crests and wave refraction seen on SAR scenes of the MIZ are reproduced by simulation, assuming that sea ice acts like a low pass filter on the wave spectrum. The impact of sea ice on the azimuthal cut-off is studied by simulation of the azimuthal SAR image auto-correlation function as well as the two-dimensional SAR image spectrum. Sensitivity studies are performed using parametric models for wind sea and swell systems. The impact of a possible increase of the coherence time within sea ice as discussed in Vachon *et al.* [1993] for airborne data is analysed. It is shown that for the ERS SAR configuration the degraded azimuthal resolution is dominated by the orbital velocity variance, while coherence time has a minor impact. The azimuthal cut-off wavelength can therefore be used to gain information about the orbital sea surface motion in the open water as well as in sea ice.

A first order analysis of wave damping observed on SAR scenes acquired over the MIZ is carried out using a technique which was originally developed for wind estimation by Kerbaol *et al.* [1998]. The method does not require a priori information and is insensitive to the RAR modulation. The azimuthal SAR image cut-off wavelength is estimated and related to the orbital velocity variance of the sea surface by regression. The model is fitted based on a global set of model ocean wave spectra.

The technique is applied within the sea ice and in the open water in front of the ice boundary. Based on simple models for wind sea and swell, ocean wave attenuation rates are obtained from the observed orbital velocity decrease of waves entering the ice. The required wind information is derived from calibrated SAR data using a method originally developed for scatterometers [Lehner *et al.*, 1998].

Two case studies showing examples from the Greenland Sea and the Weddell Sea are presented. It is shown that the estimated wave damping is consistent with damping parameters found in earlier field campaigns carried out in the Weddell Sea and the Bering Sea.

An inversion technique providing estimates of the two-dimensional wave spectra behind and in front of the ice boundary as well as a two-dimensional filter function characterising the sea ice impact is introduced. The technique is based on simultaneous inversion of the two-dimensional image spectra in the open water and within the ice, using a priori information from an ocean wave model. It is shown that the technique gives results consistent with the first order analysis based on the cut-off estimation.

7.1 Ocean wave attenuation by sea ice

The attenuation of ocean waves by sea ice is a well known effect [Squire *et al.*, 1995]. Wadhams *et al.* [1988] reports about in situ wave measurements carried out in the

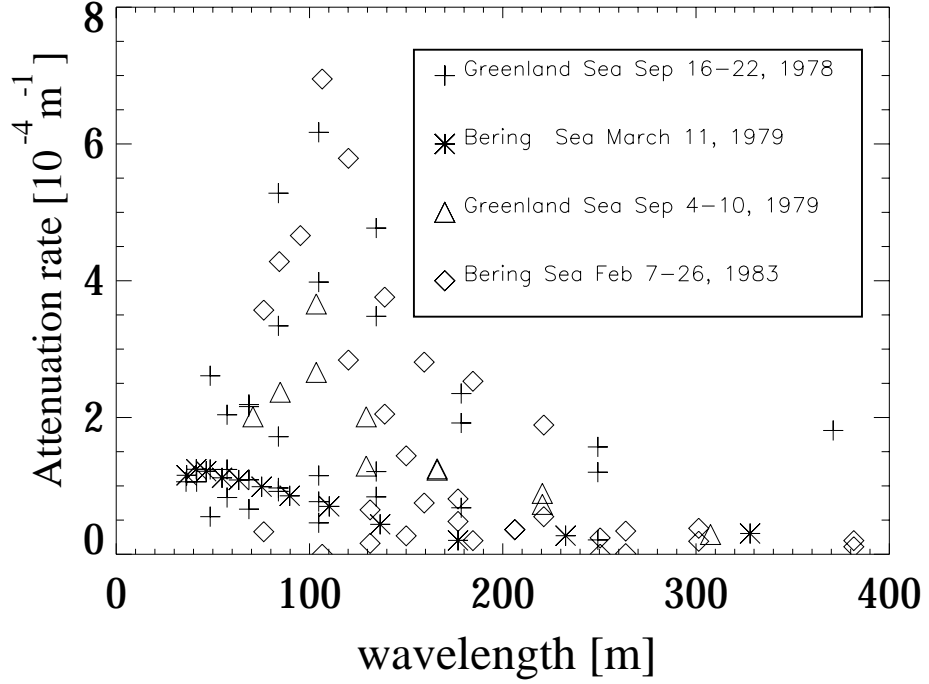


Fig. 7.1: Attenuation rates ρ_D of ocean waves damped by sea ice as reported in *Wadhams et al.* [1988] (compare eq. 7.1). The estimates were obtained under various ice conditions in the Greenland Sea and the Bering Sea.

Greenland and Bering Sea between 1978 and 1983. The experiments suggest that the wave energy decay is approximately negative exponential with increasing distance x_\perp from the ice boundary. For a given wave number k with wave energy $F_k(0)$ at the ice boundary, the wave energy within the sea ice is thus given by

$$F_k(x_\perp) = F_k(0) \exp(-\rho_D x_\perp) \quad (7.1)$$

with damping rate ρ_D . Attenuation rates for different wavelength reported in *Wadhams et al.* [1988] are shown in Fig. 7.1. Frequency was converted into wavelength using the dispersion relation for deep water (compare eq. 2.9). The highest frequency measured is about 0.2 Hz, which corresponds to about 40 m wavelength. Damping rate estimates were obtained under various ice conditions. As can be seen, ρ_D has a high variability especially for shorter waves. The experiments showed that the damping rates increase with decreasing wavelength except for some roll-over effects, which were observed at the shortest wavelength in some cases. The e-folding distance for a 100 m wave goes down to 1–2 km in some cases, while it is well over 20 km for most wave systems longer than 250 m.

Due to the complex mechanical properties of sea ice, wave damping is still not fully understood theoretically [*Squire et al.*, 1995]. A simple model, which is appropriate for frazil, brash and pancake ice, describes sea ice as a viscous layer of constant thickness

h and ice concentration c_I , is the mass-load-model [Wadhams *et al.*, 1988]. The model predicts an increase of the wavenumber component k_I^\perp defined as perpendicular to the ice boundary within the ice. Denoting the respective component in the open water with k_W^\perp one has:

$$k_I^\perp = \frac{k_W^\perp}{1 - c_I h k_W^\perp \rho_I / \rho_W} . \quad (7.2)$$

Here, $\rho_I \approx 900 \text{ kg m}^{-3}$ and $\rho_W \approx 1025 \text{ kg m}^{-3}$ are the densities of ice and water respectively. As the wave frequency is the same for both the water and the ice covered region (due to the boundary conditions at the ice edge), the waves have a reduced phase speed within the sea ice. There exists a critical wave frequency ω_c at which both the wavelength and phase speed is zero in the ice, and the waves are totally reflected at the ice boundary

$$\omega_c = \sqrt{\frac{\rho_W g}{\rho_I c_I h}} . \quad (7.3)$$

Cut-off wavelengths for a given product of c_I and h are shown in Fig. 7.2. The indicated intervals for the product $c_I h$ are typical for frazil and brash ice. It can be seen that under realistic sea ice conditions only waves shorter than about 25 m are totally reflected at the ice boundary.

Another consequence of the increase of the perpendicular wavenumber component in the mass-load-model is a refraction of waves towards the normal of the ice boundary. Denoting the incidence angle of the ocean waves with α and the angle of refraction with β , Snell's law reads [Wadhams *et al.*, 1988]

$$\frac{\sin \beta}{\sin \alpha} = \frac{k_W}{k_I} , \quad (7.4)$$

where k_W and k_I are the wave numbers in the open water and the sea ice respectively.

The simple mass-load-model is not able to reproduce the observed continuous energy decay of waves entering an ice region with individual ice floes. This problem is complicated, because it strongly depends on the size, distribution and mechanical properties of the ice floes. Several numerical models of much higher complexity exist, which try to describe this process. A model reproducing in situ measurements quite well except for the observed roll-over effect is the multiple scattering model [Squire *et al.*, 1995].

7.2 SAR imaging of ocean waves in ice

In this section the SAR imaging mechanism for ocean waves travelling into sea ice is discussed. As explained in Chapter 4, SAR wave imaging in open water is dominated by Bragg scattering leading to a relatively simple model for the RAR modulation. In the case of sea ice the situation is more complicated as different backscattering mechanisms are involved. Here, the scattering process is in general a combination of Bragg and volume scattering. In addition, scattering at the edges of ice floes can have a significant impact. The exact backscattering processes depend strongly on the detailed history of the sea ice. For example, for first year ice surface scattering dominates, whereas for multi-year ice volume scattering from air bubbles has to be taken into account as well.

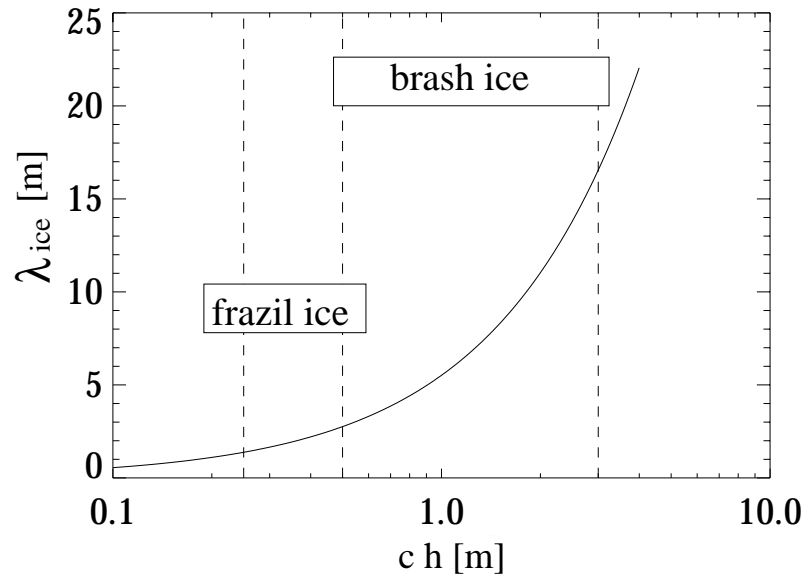


Fig. 7.2: The minimum wavelength λ_{ice} of wave components, which are able to propagate from the open water into the sea ice according to the mass-load-model (compare eq. 7.3). The ice cut-off wavelength is shown as a function of the product of ice thickness h and ice concentration c_I .

For the main part of this chapter, details about the backscattering process are not essential, because the presented technique is based on the Doppler shifts of the returned signals with the respective signal intensity having a minor impact. Only for the last section, where a retrieval method for two-dimensional wave spectra in the MIZ is presented, knowledge about the RAR transfer function within sea ice is required. As explained in the next section, an empirical transfer function reported in literature is used for this purpose.

Another aspect to be taken into account is the scene coherence time τ_c introduced in Chapter 3. There is some indication that the coherence time for sea ice is longer than for open water [Vachon *et al.*, 1993]. However, for the presented technique, which is based on the dependence of the azimuthal cut-off on the orbital velocity variance, this effect has a minor impact, at least for the ERS SAR configuration, as shown in Fig. 4.7.

7.2.1 Real aperture radar modulation in ice

Fig. 7.3 shows the modulus of the normalised MTF $k_y^{-1} T^R$ for an incidence angle of 23° and VV polarisation. The solid line represents the theoretical RAR MTF (compare eq. 4.5), while the dashed and dashed dotted lines refer to tilt MTF and range bunching MTF respectively. The lower dashed dot dotted line in Fig. 7.3 was calculated by extrapolating airborne tilt MTF measurements over ice performed by Vachon *et al.* [1993]. For incidence angles between 40° and 75° and VV polarisation

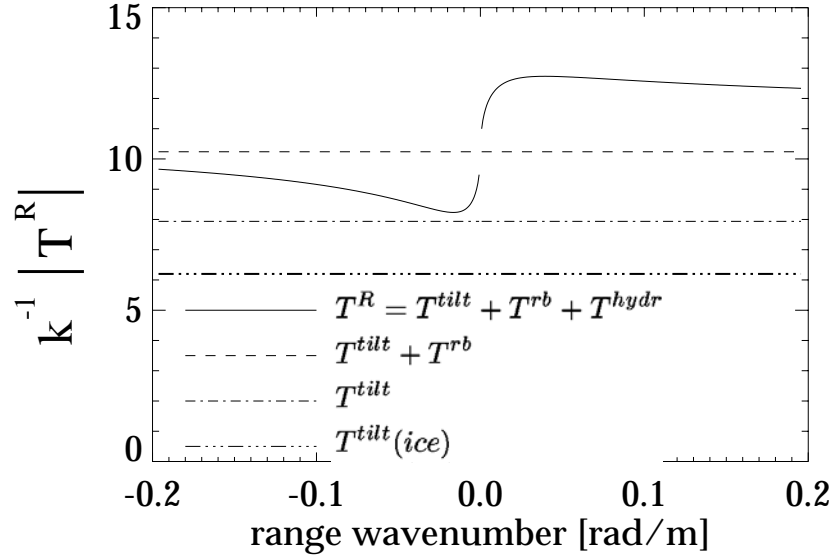


Fig. 7.3: Modulus of (normalised) tilt, range bunching and hydrodynamic modulation transfer functions. VV polarisation and 23° incidence angle are assumed. The tilt transfer function for ice was derived by extrapolating measurements reported in *Vachon and Krogstad* [1994].

the following tilt MTF was derived

$$\overline{T_k^{tilt}} = i k_y \frac{180 \log(10)}{10 \pi} (2A\theta + B) \quad (7.5)$$

with $A = 0.0022$, $B = -0.56$, and θ given in degree. As the estimation of the tilt MTF for 20° incidence angle by extrapolation is unlikely to give accurate results and the obtained value is only 20 % different from the theoretical value for the open sea we will use the theoretical tilt MTF for both open water and sea ice. Hydrodynamic modulation is believed to be negligible within sea ice and is therefore omitted for simulations in ice.

Like other authors [*Vachon et al.*, 1993], we assume that tilt and range bunching are the dominating RAR modulation mechanisms within sea ice. It is obvious that accurate estimates for the tilt MTF are difficult to obtain, as it is strongly dependent on the sea ice type. Therefore, the analysis of wave damping will start with a method, which is relatively insensitive to the RAR modulation. Only in the last section, where two-dimensional wave spectra within the sea ice are retrieved, T^R is required explicitly.

7.2.2 Higher harmonics

In this section the impact of wave damping on the ocean wave imaging process is analysed based on the model presented in Chapter 4.

As explained before, SAR imaging of range travelling waves within sea ice strongly depends on sea ice type as it is dominated by the RAR modulation mechanism. For this reason the analysis concentrates on SAR imaging of azimuth travelling waves, which is dominated by the orbital velocity of the waves. Lets imagine a single harmonic wave system propagating in the exact azimuth direction. The wave spectrum is thus given by

$$F_k = \frac{H_s^2}{16} \delta_{k-k'} \quad (7.6)$$

with Dirac delta function δ , significant wave height H_s and wave number $k' = (k'_x, 0)$. The auto-correlation function of the orbital velocity u_r for this wave system is given by (compare eq. 4.28):

$$\rho^u(x) = \cos(k'_x x) |T_{k'}^u|^2 \frac{H_s^2}{16} \quad (7.7)$$

Inserting the wave spectrum into the forward transform given by eq. 4.25 (with $\Delta t=0$) yields:

$$\begin{aligned} \Phi_k^{II} &= \exp[-k_x^2 \omega^2 H_s^2 (\frac{R}{V})^2] \sum_{n=0}^{\infty} \frac{(-1)^n (k_x \omega H_s \frac{R}{V})^{2n}}{16^n n!} \int \exp(i k x) \cos(k'_x x)^n dx \\ &= \exp[-k_x^2 \omega^2 H_s^2 (\frac{R}{V})^2] \sum_{n=0}^{\infty} \frac{(-1)^n (k_x \omega H_s \frac{R}{V})^{2n}}{32^n n!} \bigotimes_{j=1}^n (\delta_{k'-k} + \delta_{k'+k}) \end{aligned} \quad (7.8)$$

Here, the RAR modulation, which is very small for an azimuth travelling wave, was neglected and the exponential factor under the integral was expanded. Furthermore, it was used that $|T_k^u| \approx \omega_k$ for small incidence angles (compare eq. 4.22). The convolution operator is denoted by \bigotimes . The image spectrum has energy at wave numbers $k = j k'_x, j = \pm 1, \pm 2, \pm 3, \dots$ and extends out to $k = \pm n k'_x$ for nonlinearity order n . Furthermore, it can be seen that the higher harmonics increase with growing wave height, frequency, and R over V ratio until the cut-off factor in front of the integral starts to dominate.

A simulation based on eq. 7.8 is shown in Fig. 7.4. A swell system of 400 m wavelength is assumed to propagate in the azimuth direction. The solid and the dashed line represent the resulting azimuthal SAR image auto-correlation functions (calculated by taking the Fourier transform of eq. 7.8) for 1.5 m and 3 m wave height respectively. The orbital velocity variance caused by the swell is $0.02 \text{ m}^2\text{s}^{-2}$ and $0.1 \text{ m}^2\text{s}^{-2}$ respectively. The dashed dotted line indicates the correlation function if an additional wind sea system, which increases the orbital velocity variance by $0.15 \text{ m}^2\text{s}^{-2}$, is assumed. The latter case shows the typical situation in the open ocean, where the higher harmonics of the image of the swell system are suppressed by an additional wind sea system. The solid and dashed lines illustrate the situation within the sea ice, where wind seas are damped leading to a spiky appearance of the image of strong swell systems in sea ice.

7.2.3 Impact of sea ice on the orbital velocity variance

As explained in the last section, imaging of waves travelling in azimuth direction is strongly influenced by the orbital velocity variance of the sea surface. In this section

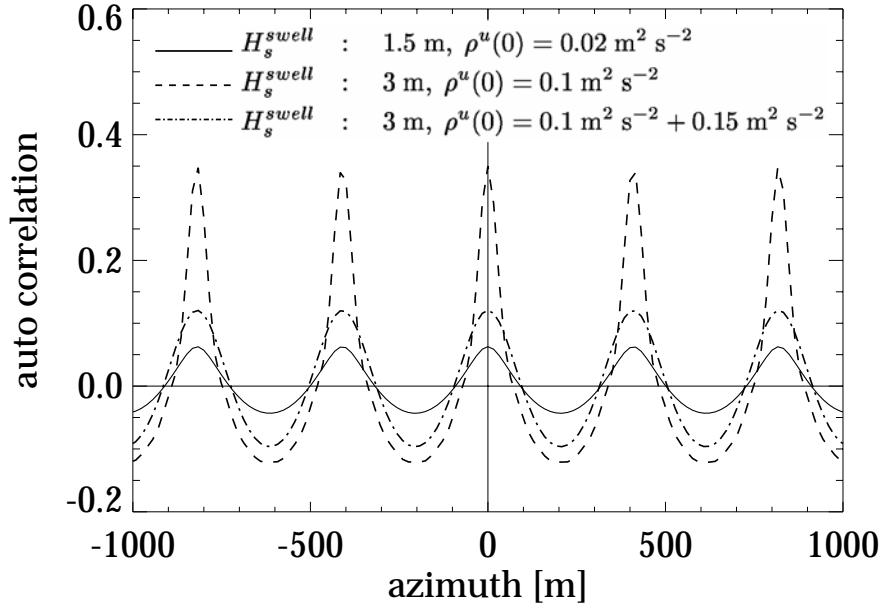


Fig. 7.4: Simulated azimuthal SAR image auto-correlation function assuming a harmonic swell system of 400 m wavelength with 1.5 (solid line) and 3 m significant wave height (dashed line) propagating in the exact azimuth direction. The dashed dotted line results if an additional wind sea system (7 ms^{-1} wind speed) is assumed.

the contribution to the orbital velocity of wind sea and swell systems is estimated using parametric models. The sea ice impact is taken into account by introducing an ice cut-off wavelength λ_{ice} .

For small incidence angles θ the orbital velocity variance $\rho^u(0)$ can be approximated as (compare eq. 4.23)

$$\rho^u(0) \approx \int \omega^2 F_{\mathbf{k}} d^2k. \quad (7.9)$$

Based on this relation a first order analysis of the impact of short wave damping on $\rho^u(0)$ can be carried out. A simple model for a wind sea spectrum with peak wave number k_p , which is chopped off by sea ice at some wave number k_{ice} , is given by

$$\int F_{\mathbf{k}} d\Phi = \begin{cases} 0 & : k \leq k_p \text{ or } k \geq k_{ice} \\ \alpha k^{-4} & : \text{else} \end{cases} \quad (7.10)$$

The k^{-4} decay assumed in this model corresponds to a ω^{-5} decay in the corresponding one-dimensional frequency spectrum (compare eq. 2.22 and Hasselmann [1973]). Inserting the model eq. 7.10 in eq. 7.9 gives

$$\rho^u(0) = \begin{cases} \alpha g \left(\frac{1}{k_p} - \frac{1}{k_{ice}} \right) & : k_p \leq k_{ice} \\ 0 & : \text{else} \end{cases} \quad (7.11)$$

It is further assumed that in the open water the wind sea is fully developed with

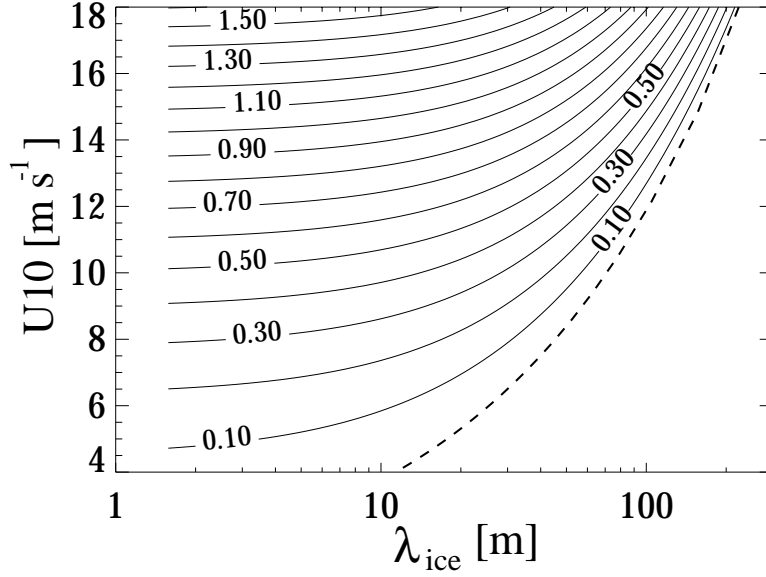


Fig. 7.5: Orbital velocity variance $\rho^u(0)$ for a fully developed wind sea as a function of wind speed U_{10} and ice cut-off wavelength λ_{ice} . The dashed line indicates the peak wavelength for a given wind speed. The unit of the isoline labels is m^2s^{-2} .

phase speed $c_p = \sqrt{g/k}$ (deep water) and wave age $U_{10}/c_p = 0.95$. Using the known relationship given by eq. 2.20 between wind speed U_{10} and significant wave height H_s the constant $\alpha = 4.5 \cdot 10^{-3}$ is obtained.

The dependence of $\rho^u(0)$ on U_{10} and the ice cut-off wavelength $\lambda_{ice} = 2\pi/k_{ice}$ is illustrated in Fig. 7.5. The dashed line indicates the peak wavelength for a fully developed wind sea in the open ocean. The orbital velocity variance of a 100 m system is about $0.6 \text{ m}^2\text{s}^{-2}$ in the open water. It decreases to $0.3 \text{ m}^2\text{s}^{-2}$ if waves shorter than 40 m are damped out by the ice.

As swell is concentrated in a relatively small region of the 2d wave spectrum eq. 7.9 can be approximated as

$$\rho^u(0) \approx \frac{\pi g}{8 \lambda_{swell}} (H_s^{swell})^2 \quad (7.12)$$

with swell wavelength λ_{swell} and swell wave height H_s^{swell} . The wavelength and wave height dependence of $\rho^u(0)$ for swell is illustrated in Fig. 7.6. A 400 m meter swell system with 3 m wave height contributes about $0.1 \text{ m}^2\text{s}^{-2}$ to the orbital velocity variance of the sea surface. Thus, in the open ocean the swell contribution to $\rho^u(0)$ is in general smaller than the contribution coming from the wind sea. The azimuthal cut-off is therefore highly dependent on the local wind field.

7.3 Azimuthal cut-off estimation

Neglecting the small influence of the coherence time τ_s , the orbital velocity variance is directly connected to the theoretical cut-off wavelength λ_{cut} . This means, the SAR

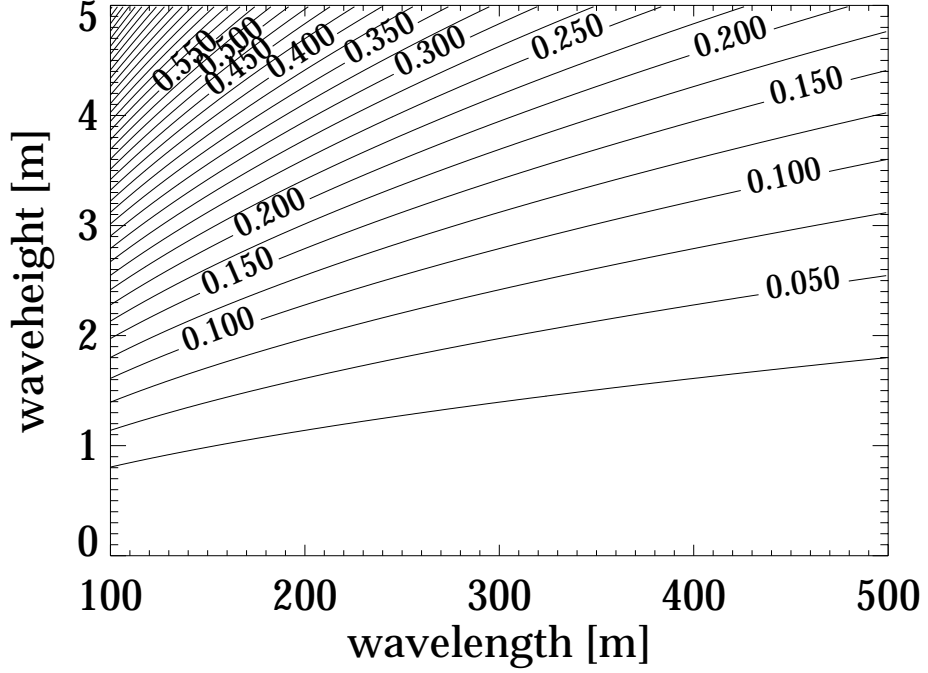


Fig. 7.6: Orbital velocity variance $\rho^u(0)$ caused by swell as a function of wavelength and significant wave height H_s . The unit of the isoline labels is m^2s^{-2} .

measurement of $\rho^u(0)$ is basically a cut-off estimation problem.

Different definitions and estimation techniques have been proposed for empirical cut-off wavelengths [Kerbaol *et al.*, 1998; Vachon *et al.*, 1997; Hasselmann *et al.*, 1996]. In this study we follow the approach introduced by Kerbaol *et al.* [1998], where a cut-off wavelength is estimated in the spatial domain. For this purpose an exponential model function of the form

$$C(x) = \exp\left[-\frac{16 \ln 2}{\lambda_{3dB}^2} x^2\right] \quad (7.13)$$

is fitted to the azimuthal cross-correlation function of two looks processed from the azimuth spectrum of complex SAR data [Kerbaol *et al.*, 1998]. The multi-look technique is used to remove the speckle contribution as explained in Chapter 3. The cut-off wavelength λ_{3dB} introduced here is exactly two times the 3dB width of the cross-correlation function and thus a reasonable measure for the minimum wavelength resolved in the SAR flight direction. In order to relate the empirical λ_{3dB} to the theoretical cut-off wavelength λ_{cut} (compare eq. 4.46), a global data set of 3000 WAM ocean wave model spectra provided by the the ECMWF was used to calculate a linear regression between both parameters. For each wave spectrum the model eq. 7.13 was fitted to the simulated cross-correlation function calculated by taking the Fourier transform of eq. 4.25. As the highest frequency in the WAM model is $f_{max} = 0.4$ Hz corresponding to about 10 m wavelength, the net contribution to $\rho^u(0)$ from waves

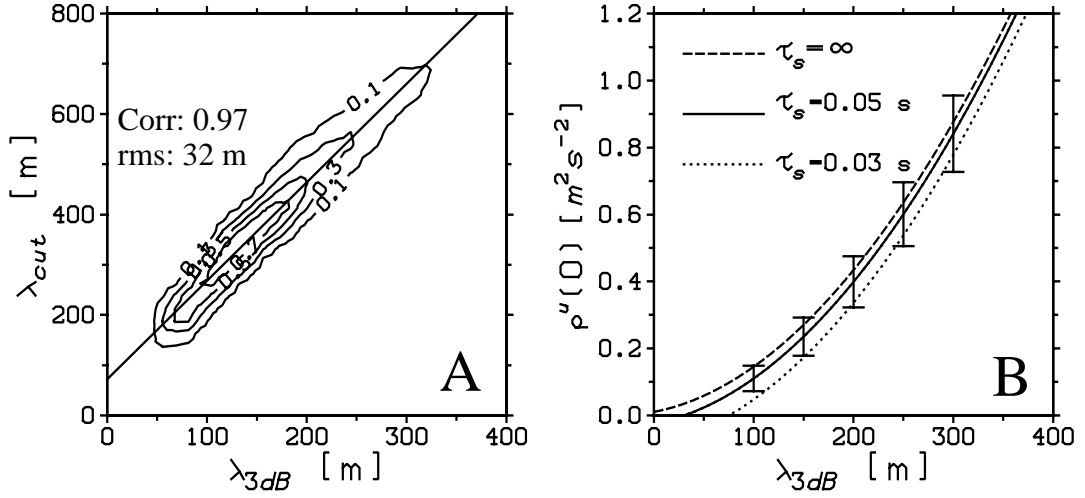


Fig. 7.7: (A) Empirical cut-off wavelength λ_{3dB} measured according to eq. 7.13 versus theoretical cut-off wavelength defined by eq. 4.46. The plot is based on simulations using a global data set of 3000 ECMWF wave model spectra. (B) Resulting relationship between λ_{3dB} and the orbital velocity variance assuming coherence times τ_s of 0.03 s, 0.05 s and infinity. The error bars refer to the curve for $\tau_s = 0.05$ s.

shorter than 10 m was calculated by extrapolating the one-dimensional frequency spectrum with a f^{-5} tail. Using the approximation given in eq. 7.9, the following term then has to be added to $\rho^u(0)$:

$$\langle u_r^2 \rangle_{Hf} = 2\pi^2 F(f_{max}) f_{max}^3 \quad (7.14)$$

Here, $F(f_{max})$ is the spectral density of the one-dimensional frequency spectrum at the shortest period. The corresponding scatter plot is shown in Fig. 7.7 (A). The linear regression with a correlation of 0.97 is given by:

$$\lambda_{cut} = 1.95 \cdot \lambda_{3dB} + 74 \text{ m} \quad (7.15)$$

The resulting empirical relation between λ_{3dB} and the orbital velocity variance $\rho^u(0)$ is shown in Fig. 7.7 (B).

7.4 Case studies

7.4.1 Case study in the Weddell Sea

Fig. 7.8 (left) shows a 5×10 km ERS-2 SAR scene acquired over the Weddell Sea on July 18, 1992, 12:41 UTC (Orbit 5264, Frame 4815). The image is centred at 58.98°S 52.9°W with flight direction (205°) upwards. Following the bright open water area two different types of sea ice with significantly different NRCS values can be seen. The typical situation at the ice boundary is that the open water is followed by grease or brash ice, which completely damps out the short Bragg waves, leading to the low radar backscatter observed on the SAR image. The grease ice area is then usually followed by a region with small ice floes (pancake ice) with slightly higher radar cross section than grease ice.

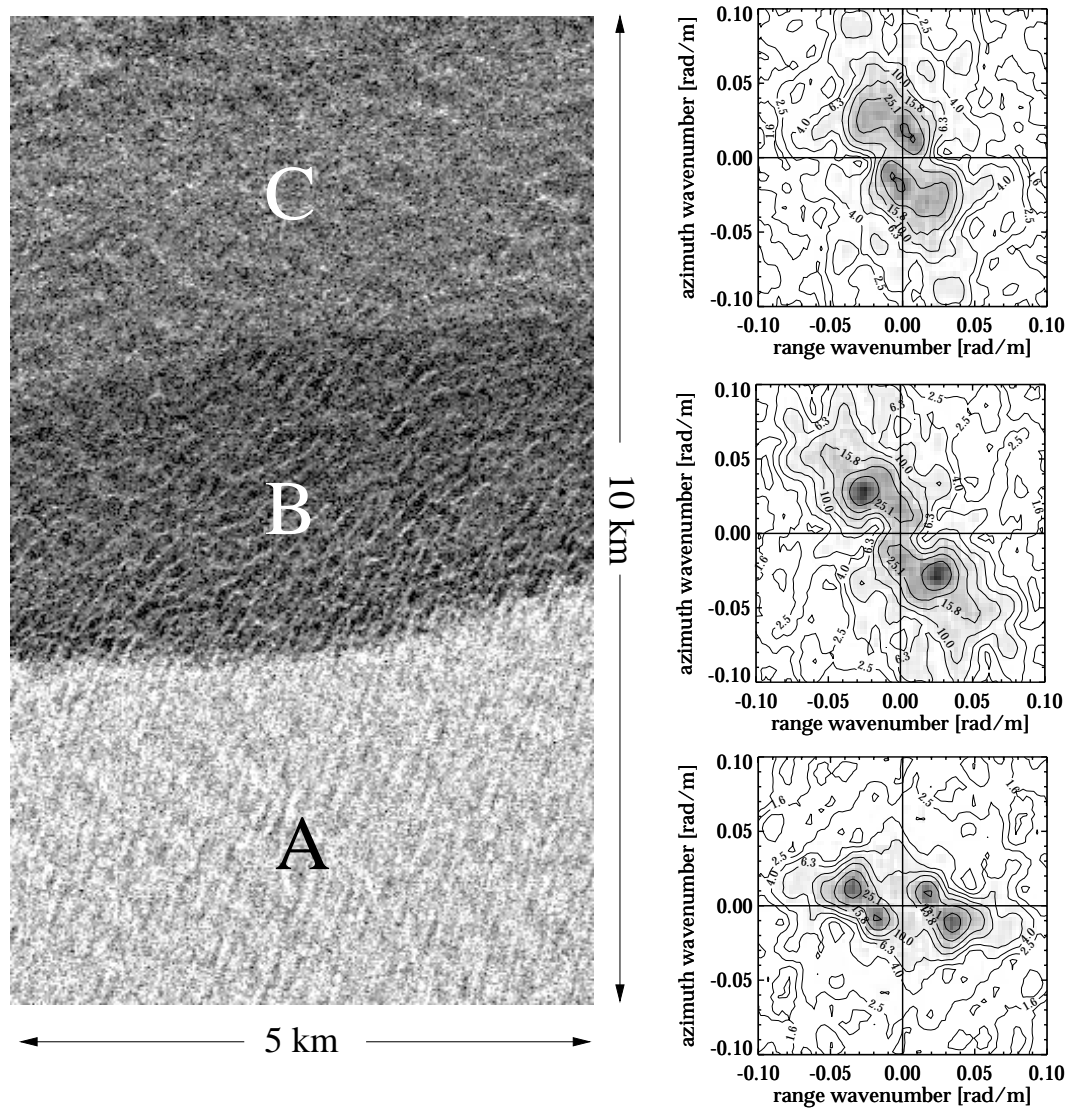


Fig. 7.8: (left) 5×10 km subimage of an ERS-2 SAR full swath scene acquired over the Weddell Sea on July, 18, 1992 at 12:41 UTC. The image is centred at 58.98° S 52.9° W with flight direction (205°) upwards. The bright region at the bottom is open water followed by two darker regions, which are covered by two different types of sea ice. (Right) Image spectra calculated for regions A, B and C (from bottom to top).

The SAR wind measurement technique described in *Lehner et al.* [1998], *Horstmann et al.* [2000] or *Horstmann et al.* [2003] was applied yielding about 11 ms^{-1} wind speed. The method is based on the CMOD4 model originally developed for the scatterometer and requires calibration of the SAR images. The wind direction of about 340° (coming from) can be derived from wind streaks observed in the open water. The wind direction is confirmed by the observation of a very sharp ice boundary, which is typical if strong wind is blowing from the open ocean towards the sea ice.

The SAR image spectra on the right hand side of Fig. 7.8 show two wave systems

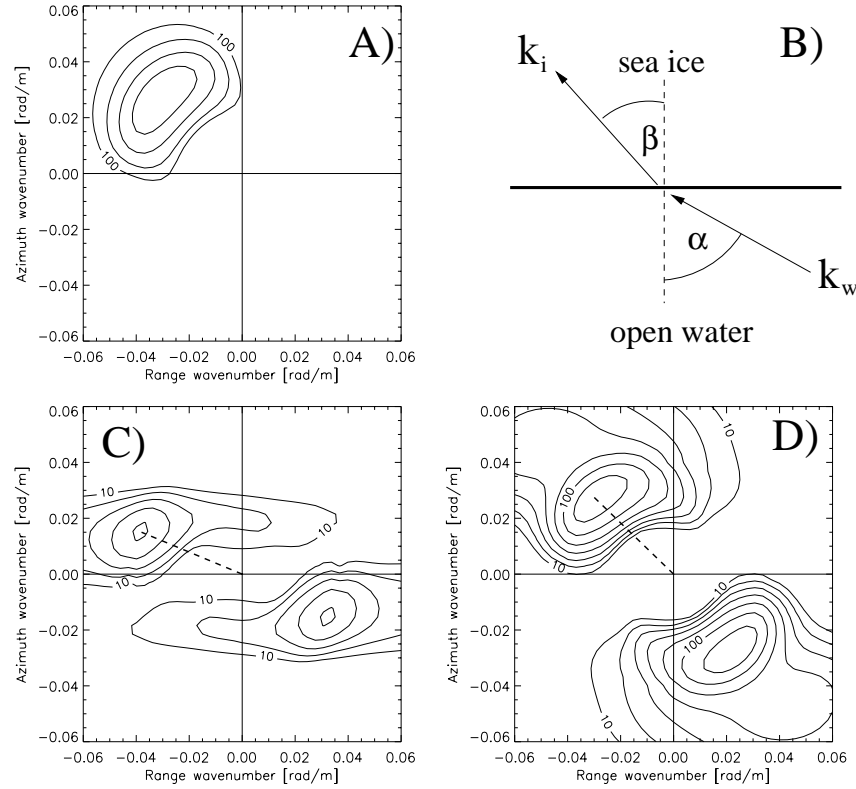


Fig. 7.9: Simulation showing that refraction phenomena at the ice boundary observed on SAR images can be explained by imaging artefacts associated with the damping of short ocean waves. (A) Parameterised ocean wave spectrum (JONSWAP) representing a 150 m ocean wave system. (B) Schematic illustration of refraction mechanism (compare eq. 7.4). (C) Simulated SAR image spectrum in open water. (D) SAR image spectrum in sea ice, simulated by removing ocean wave components shorter than 80 m.

of about 180 m and 300 m wavelength propagating into the ice. A linear inversion of the spectrum in the open water gave about 2 m wave height for the 180 m wave and 1 m wave height for the 300 m wave system. In the grease and brash ice region one can see the 180 m wave being refracted towards the normal of the ice boundary by about 15° . The image modulation is increased by about 3 dB at the same time. In the upper ice area the 180 m wave is almost invisible in the image.

In some studies refraction phenomena like the observed one are interpreted as a real refraction of the ocean waves at the ice boundary [Shuchman and Rufenach, 1994]. However, applying the mass-load-model described in Section 7.1 to the observed refraction yields an unrealistic ice coverage with a product of ice concentration c_I and ice thickness h of about 5 m. This indicates that the observed refraction is in fact mainly a SAR imaging artefact, which is due to damping of short waves by the ice. Fig. 7.9 shows a simulation, which illustrates this refraction effect. SAR image spectra were simulated in open water (C) as well as in sea ice (D) using a parameterised

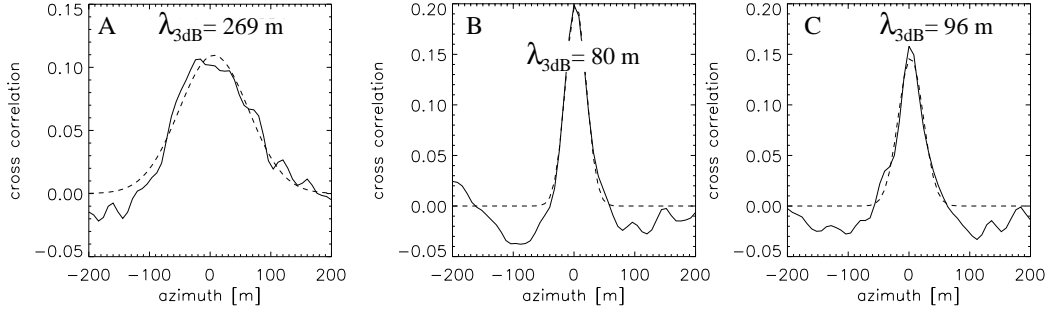


Fig. 7.10: Azimuthal look cross-correlation functions calculated in regions A, B and C as indicated in Fig. 7.8.

JONSWAP (compare Chapter 2) ocean wave spectrum (A) representing a 150 m wave system. The simulations are based on the forward model (eq. 4.25), where the sea ice impact was simulated by removing all waves shorter than 80 m. Comparing the SAR spectra in water and ice, one can see that short wave damping is in fact able to cause refraction phenomena like the observed one. The inversion scheme presented in Section 7.5 will use the change of the two-dimensional SAR spectrum to gain quantitative information on the ice damping characteristics.

To study the wave damping a cut-off analysis as described in Section 7.3 was performed. The azimuthal auto-correlation functions calculated for regions (A), (B), and (C) are shown in Fig. 7.10. In the open water a cut-off wavelength of $\lambda_{3dB} = 269$ m was found. From the relationship between λ_{3dB} and $\rho^u(0)$ derived in Section 7.3 (compare Fig. 7.7 (B)) the orbital velocity in the open water is estimated as $0.7 \text{ m}^2\text{s}^{-2}$. This is consistent with the general theoretical findings about the orbital velocity variance of wind seas and swell systems presented in Section 7.2.3; the contribution of the two long wave systems to the orbital velocity variance is about $0.1 \text{ m}^2\text{s}^{-2}$ with the main contribution coming from the 180 m wave system (compare Fig. 7.6). Assuming a fully developed wind sea, the measured wind speed leads to a wind sea system of about 2 m wave height and 80 m wavelength, which contributes another $0.6 \text{ m}^2\text{s}^{-2}$ to the orbital velocity variance (compare Fig. 7.7). This results in a total velocity variance of about $0.7 \text{ m}^2\text{s}^{-2}$ confirming the value obtained by the cut-off estimation technique. Note, that the wind sea is not visible on the SAR image as it is propagating in the approximate azimuth direction and therefore suppressed by the azimuthal cut-off.

In region (B) of Fig. 7.8 the cut-off wavelength decreases to 80 m, which corresponds to an orbital velocity variance of about $0.05 \text{ m}^2\text{s}^{-2}$. This decrease can only be explained if it is assumed that the wind sea is almost completely damped out by the ice. As explained in Section 7.1 this is realistic, as e-folding distances of down to 1-2 km have been observed in earlier field campaigns reported by *Wadhams et al.* [1988] (compare Fig. 7.1). As a complete damping of the wind sea still leaves about $0.1 \text{ m}^2\text{s}^{-2}$ velocity variance it can be concluded that also the wave height of the 180 m wave must have been reduced by about 3 dB to obtain the observed value for $\rho^u(0)$ within region (B) (compare Fig. 7.6). In fact, looking at the image in Fig. 7.8 one can actually see how the wave slowly disappears as it propagates through the ice region

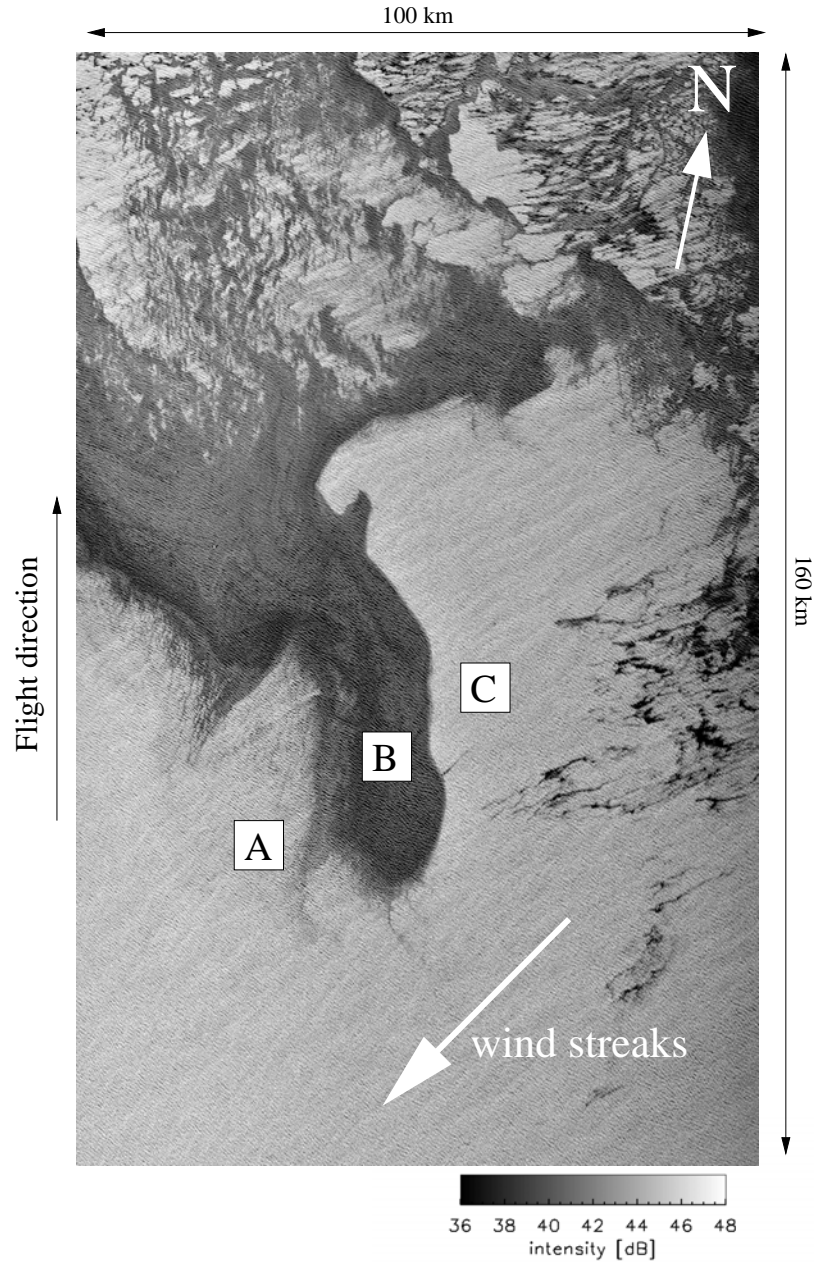


Fig. 7.11: 100×130 km ERS-2 SAR scene acquired over the Greenland Sea on Feb 1, 1992, 23:32 UTC, showing the marginal ice zone. The image is centred at 66°45'0"N, 28°47'49"W. The bright region is open water, while the darker areas are covered with sea ice.

(B).

In region (C) the observed cut-off wavelength is 96 m, which corresponds to about $0.05 \text{ m}^2\text{s}^{-2}$ as in region (B). Although, the difference to the cut-off wavelength of 80 m observed in region (B) is at the limit of the measurement accuracy (compare Fig. 7.6), a slight increase of the orbital velocity is not unrealistic. In fact an increase of

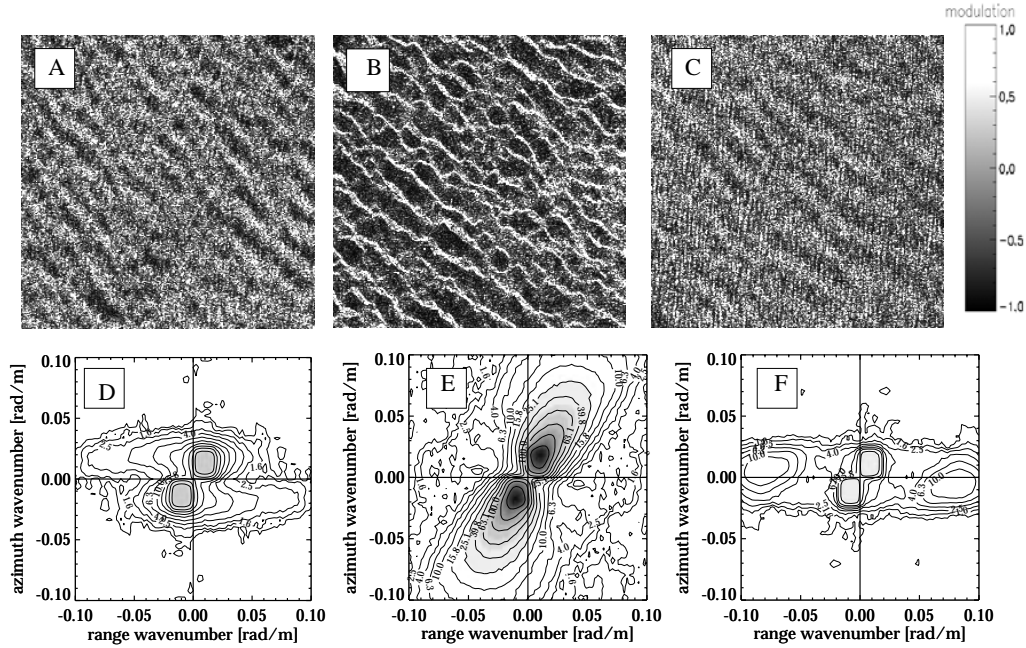


Fig. 7.12: (Top) 5 km by 5 km subimages extracted from locations A,B,C indicated in Fig. 7.11. Grey values correspond to the SAR image modulation (compare eq. 3.36). (Bottom) Modulus of corresponding SAR cross spectra with identical scaling of grey values. The isolines are logarithmically spaced with 5 isolines per decade and labels given in m^2 .

spectral energy at higher frequencies has been observed in field campaigns in some cases. The mechanism, which is not yet fully understood up to now [Squire *et al.*, 1995], is known as roll-over effect, and could be an explanation for the small increase of the cut-off wave length.

7.4.2 Case study in the Greenland Sea

Fig. 7.11 shows a 100×130 km ERS-2 SAR scene (Orbit 2856, Frame 1341 and part of Frame 1359) acquired over the Greenland Sea on Feb 1, 1992, 23:32 UTC. The image is centred at $66^\circ 45' 0''\text{N}$, $28^\circ 47' 49''\text{W}$ with flight direction (342°) upwards and shows the marginal ice zone with dark areas corresponding to sea ice and bright areas indicating open water.

The SAR wind measurement technique described in [Lehner *et al.*, 1998] was applied, giving about 12 ms^{-1} wind speed. The wind direction of about 70° (coming from) can be derived from wind streaks observed in the open water area and is indicated by an arrow in Fig. 7.11. The directional ambiguity of wind direction was resolved comparing to ECMWF wind fields. The indicated wind direction is also suggested by the observation of a very sharp ice edge on the east side of the ice covered area and a more fuzzy appearance of the westerly ice boundary.

Three 5×5 km subimages taken from locations (A), (B), and (C) indicated in

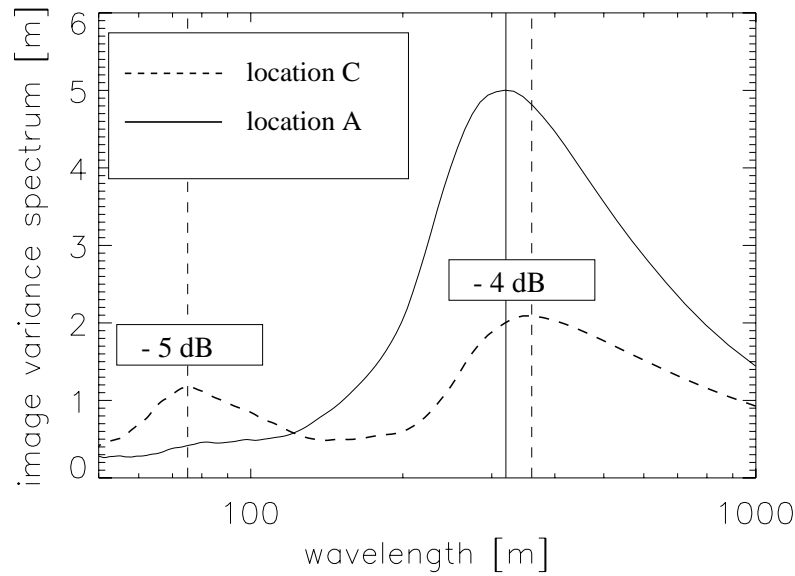


Fig. 7.13: One-dimensional SAR image variance wave number spectra for locations (A) (solid) and (C) (dashed) indicated in Fig. 7.11.

Fig. 7.11 are shown in Fig. 7.12 together with the modulus of the corresponding cross spectra. At location (C) a wind sea system of about 80 m and a swell system of about 350 m wavelength can be seen travelling in easterly and north-westerly direction respectively. The directional propagation ambiguity was resolved by inspection of the imaginary part of the cross spectrum. The wind sea system is not visible in the sea ice (location (B)) nor in the open water at location (A). For the swell a significant reduction of image modulation of about -4 dB is observed comparing locations (A) and (C). This effect becomes more obvious looking at the one-dimensional wave number spectra shown in Fig. 7.13.

A wind speed of 12 ms^{-1} results in a fully developed wind sea of about 100 m wavelength and 3 m significant wave height. The observed wavelength of 80 m is in reasonable agreement with the theoretical value indicating that the wind sea is almost fully developed. As the wind sea is not visible in area (A) it can be assumed that it is damped out completely by the ice. This finding is again consistent with in situ measurements, which yield e-folding distances down to 1-2 km for 100 m waves (compare Fig. 7.1).

Applying the cut-off estimation technique described in Section 7.3 gives $\lambda_{3dB} = 223 \text{ m}$ for area (A), $\lambda_{3dB} = 98 \text{ m}$ for the ice covered region (B) and $\lambda_{3dB} = 314 \text{ m}$ for region (C). For area (C), where both wave systems are visible, this yields an orbital velocity variance of $0.9 \text{ m}^2\text{s}^{-2}$ (compare Fig. 7.7 (B)). Assuming that the wind sea contributes between 0.7 and $0.8 \text{ m}^2\text{s}^{-2}$ to $\rho^u(0)$ (compare Fig. 7.5), it can be concluded that the swell contributes between $0.1 \text{ m}^2\text{s}^{-2}$ and $0.2 \text{ m}^2\text{s}^{-2}$ and thus has a wave height between 3 and 4 m (compare Fig. 7.6).

In the ice $\rho^u(0)$ decrease to about $0.1 \text{ m}^2\text{s}^{-2}$, which is consistent with the as-

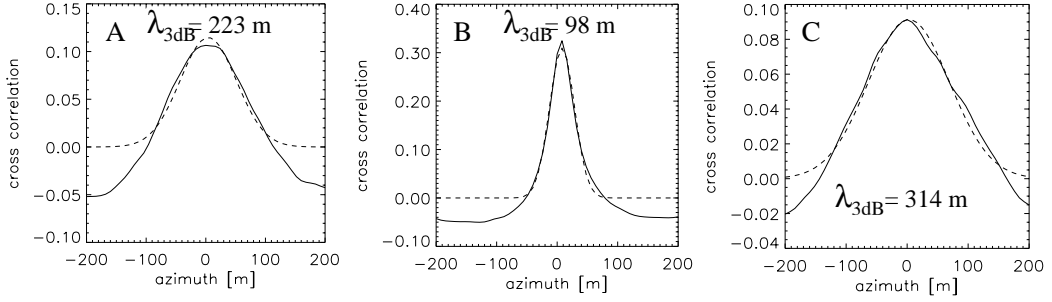


Fig. 7.14: Azimuthal look cross-correlation functions with fitted Gaussians calculated from subimages shown in Fig. 7.12. Cut-Off wavelengths were estimated using the model given by eq. 7.13.

sumption that the wind sea is damped out completely and that the long swell is only slightly affected.

In region (A), where only the swell system is visible on the SAR image, the estimated orbital velocity variance is about $0.5 \text{ m}^2\text{s}^{-2}$. This is due to the generation of new short waves by the wind, which contribute about $0.4 \text{ m}^2\text{s}^{-2}$ to $\rho^u(0)$. Note that the new waves are too short to be visible on the SAR image; the range resolution of the ERS SAR is about 30 m (near range), i.e. waves must have wavelength well over 60 m to be imaged by the system. However, at 11 ms^{-1} wind speed a fetch between 50 and 100 km is required to generate waves of such length [Apel, 1995]. As there is only about 30 km open water visible on the SAR image left of the ice region, the new waves cannot be detected.

7.5 A SAR ocean wave inversion scheme for the MIZ

In this section a new SAR inversion scheme for ocean waves in ice is presented. The method is based on studies of short ocean wave attenuation described in the previous chapters. The algorithm uses models and techniques which have already been successfully used for ocean waves in open water.

The method derives damping parameters of the sea ice by combined use of SAR information from the ice region, the open water in front of the ice, and information from an ocean wave model. The output of the algorithm is a two-dimensional ocean wave spectrum in front and behind the ice boundary as well as a two-dimensional filter function characterising the sea ice impact on the wave spectrum.

Similar to the approach presented in [Hasselmann and Hasselmann, 1991], the inversion scheme is based on a minimisation of the following cost function:

$$J(F, \tilde{\rho}) = \int G_k (\tilde{\Phi}_k^W - \Phi_k^W(F))^2 + \overline{G}_k (\tilde{\Phi}_k^I - \Phi_k^I(B^{\tilde{\rho}} F))^2 + H_k (\hat{F}_k - F_k)^2 + V_k (\hat{F}_k F_{-k} - \hat{F}_{-k} F_k)^2 dk \quad (7.16)$$

Here G_k , \overline{G}_k , H_k and V_k are weighting functions and $B^{\tilde{\rho}}$ is a parameterised filter function describing the sea ice impact on the ocean wave spectrum. An ocean wave

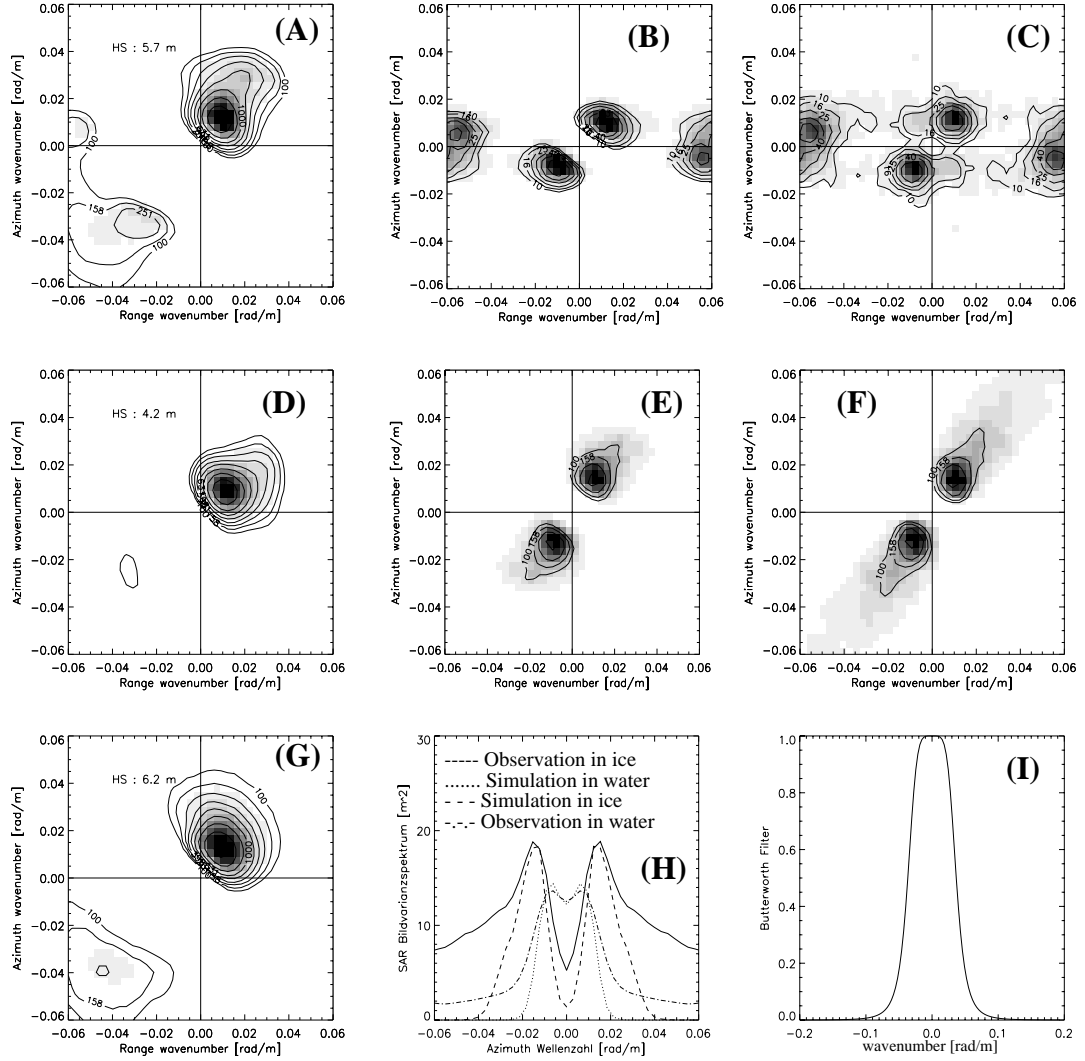


Fig. 7.15: (A) Inverted ocean wave spectrum in open water. (B) Simulated SAR image spectrum in open water. (C) SAR image spectrum observed in open water. (D) Inverted ocean wave spectrum in sea ice. (E) Simulated SAR image spectrum in sea ice region. (F) SAR image spectrum observed in sea ice. (G) First guess ocean wave spectrum computed with the WAM model. (H) Comparison of simulated and observed cut-off in open water and sea ice. (I) Calculated Butterworth filter with $\gamma = 10$ and $\tilde{k} = 0.036 \text{ rad m}^{-1}$.

spectrum F and damping parameters $\tilde{\rho} = (\rho_1, \dots, \rho_l)$ are determined such that the deviation between the simulated SAR spectra $\Phi_k^W(F)$ and $\Phi_k^I(B^{\tilde{\rho}} F)$ in open water and sea ice and the corresponding observations $\tilde{\Phi}_k^W$ and $\tilde{\Phi}_k^I$ is small. In a first approach, Φ_k^W and Φ_k^I were calculated by using the quasi-linear approximation (eq. 4.31). The only difference between Φ_k^I and $\tilde{\Phi}_k^W$ is the neglect of the hydrodynamic modulation for waves in ice (compare Section 7.2.1).

In addition, eq. 7.16 contains two regularisation terms. By appropriate choice of the weighting functions, the first term ensures that missing information on short

azimuthal waves is taken from the first guess ocean wave spectrum \hat{F} . The second term forces the algorithm to take the propagation direction of the long ocean waves, or more precisely the ratio of F_k and F_{-k} from the first guess.

The filter function $B_k^{\tilde{\rho}}$ was in a first approach taken as a Butterworth filter, assuming that sea ice acts like a filter with relatively steep flanks as suggested by the mass-load-model (compare Section 7.1).

$$B_k^{(\gamma, \tilde{k})} = \left(1 + \left(\frac{|k|}{\tilde{k}} \right)^\gamma \right)^{-1} \quad (7.17)$$

The filter is isotropic with 3dB width given by \tilde{k} . The flank steepness can be controlled by appropriate choice of γ .

To solve the minimisation problem given by eq. 7.16 a new technique was developed using the quasi-linear approximation (eq. 4.31) of the SAR imaging model. The approach is based on the following Lagrange function [Spellucci, 1993]:

$$\begin{aligned} L(F, \tilde{\rho}, \alpha, \bar{\alpha}, \lambda_\alpha, \lambda_{\bar{\alpha}}) = & J(F, \tilde{\rho}) - \lambda_\alpha \left(\alpha - \int |T_k^u|^2 F_k d^2k \right) \\ & - \lambda_{\bar{\alpha}} \left(\bar{\alpha} - \int |T_k^u|^2 B_k^{\tilde{\rho}} F_k d^2k \right) \end{aligned} \quad (7.18)$$

The new state variables $\alpha, \bar{\alpha}$ represent the orbital velocity variance in open water and in the sea ice region respectively (compare eq. 4.28). Introducing the Lagrange parameters λ_α and $\lambda_{\bar{\alpha}}$, the derivative of eq. 7.16 with respect to F becomes linear. Using the necessary conditions for a solution of the optimisation problem, F can therefore be expressed as a function of $\alpha, \bar{\alpha}, \tilde{\rho}, \lambda_\alpha, \lambda_{\bar{\alpha}}$. Denoting the number of filter parameters with l , the remaining equations lead to a $4 + l$ -dimensional zero crossing problem, which can be solved very efficiently using a Newton method.

The method was applied to the ERS SAR scene discussed in Section 7.4.2. Fig. 7.15 shows results of the inversion. The SAR spectra observed in the ice and the open water are shown in (C) and (F) respectively. The first guess ocean wave spectrum calculated with the WAM model can be seen in (G). In this first example only the filter width \tilde{k} was optimised, while the second parameter was fixed to $\gamma = 10$, assuming a nearly rectangular filter shape.

The inverted ocean wave spectra in sea ice and open water are shown in (A) and (D). The wave spectrum behind the ice boundary is calculated by applying the Butterworth filter shown in (I) to the open water wave spectrum. The algorithm calculated a filter width of $\tilde{k} = 0.036 \text{ rad m}^{-1}$, leading to a reduction of the orbital velocity variance from $\alpha = 1 \text{ m}^2\text{s}^{-2}$ in the open water, down to $\bar{\alpha} = 0.13 \text{ m}^2\text{s}^{-2}$ in sea ice. Note that the estimated orbital velocity variance is in good agreement with the estimates of $\rho^u(0) = 0.9 \text{ m}^2\text{s}^{-2}$ and $\rho^u(0) = 0.1 \text{ m}^2\text{s}^{-2}$ found by the simple cut-off estimation technique (compare Section 7.4.2). As can be seen, there is good agreement between the simulated and the observed SAR image spectra in open water as well as in sea ice. Although the cut-off comparison shown in (H) indicates an underestimation of energy contained in short azimuth waves, the azimuthal broadening of the spectrum as well as the long wave energy increase are reproduced by the simulation.

The presented algorithm can be extended for use with SAR cross spectra [Engen and Johnson, 1995] using standard methods. In this case, the second regularisation

term can be omitted, as the propagation direction of the long waves is contained in the complex SAR data. In addition the approach described in *Hasselmann and Hasselmann* [1991] can be used to introduce the full nonlinear SAR imaging model into the algorithm. It is expected that this extension will lead to an even better reproduction of the observed cut-off change (compare Fig. 4.5).

It is planned to apply the above techniques on a statistical basis using complex wave mode data acquired by the ENVISAT satellite. The ENVISAT ASAR provides images of 10×5 km size every 100 km along the track and thus allows to study wave damping by sea ice on a continuous basis.

A statistical analysis will provide more detailed information on the wave damping mechanism and its dependence on sea ice type. In particular, this will allow to develop techniques for the estimation of classical sea ice parameters, like ice thickness or ice concentration, which are needed for the validation and assimilation of sea ice models.

Chapter 8

STATISTICAL ANALYSIS OF COMPLEX ERS-2 WAVE MODE DATA

In this chapter an analysis of the global data set of reprocessed complex ERS-2 imagerettes introduced in Chapter 5 is given. As explained before, the data permit the application of the cross spectra technique described in Chapter 3 and Chapter 4 on a global and statistical basis for the first time. The analysis can be regarded as a demonstration of the information content of complex imagerettes, which will be available from the ENVISAT ASAR as a standard product. The main results of the analysis were published in *Lehner et al.* [2000]. The points investigated in this thesis are the following:

- It is shown that the reprocessed high resolution images contain additional information compared to SAR image variance spectra, or SAR cross spectra which can, e.g. be used to:
 - detect imagerettes, which are contaminated by atmospheric effects or sea ice and are thus not suitable for wave measurements;
 - detect inhomogeneous wave fields, which are not properly described by a wave spectrum.
- It is shown that the propagation direction indicated by the cross spectrum phase is consistent with wave model calculations.
- It is shown that the cross spectrum phase are at least on average in good agreement with the values predicted by linear wave theory.

It should be pointed out that the analysis presented here is not supposed to give a complete overview of the information contained in complex imagerettes. In particular, an investigation of the following two aspects can be found elsewhere:

- An analysis of a global data set of intensity imagerettes was first presented in *Kerbaol et al.* [1998], showing a good correlation between mean image intensity and collocated scatterometer measurements of wind speed.
- An approach to estimate two-dimensional sea surface elevation fields from complex imagerettes was proposed in *Schulz-Stellenfleth and Lehner* [2003]. The technique enables the study of parameters which are not provided by the wave spectrum like the ratio of maximum and significant wave height on a global scale for the first time.

The proposed analysis tools like the inhomogeneity parameter introduced in Section 8.1 were also applied to simulated ENVISAT wave mode data provided by ESA in the

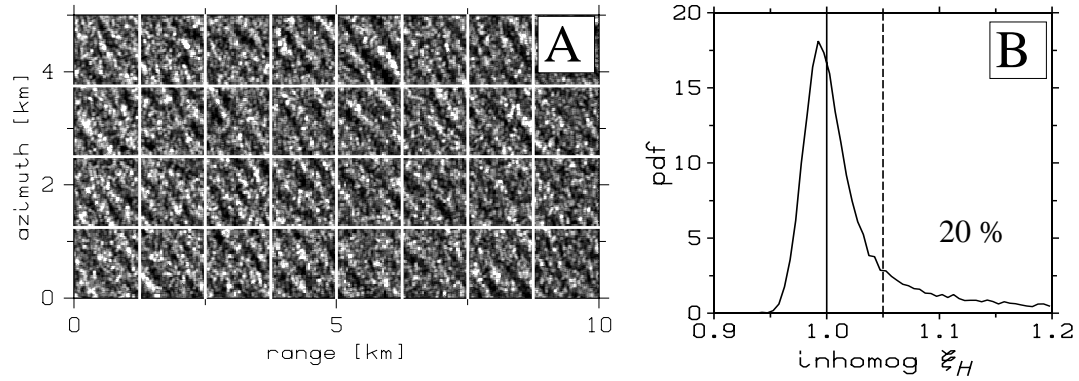


Fig. 8.1: (A) Boxes used to estimate the inhomogeneity parameter from wave mode imagerettes. (B) Histogram of the inhomogeneity parameter estimated from a global data set of 30000 imagerettes including land and sea ice.

framework of the calibration and validation activities. They turned out to be useful to sort out problems in the ENVISAT wave mode processing chain.

8.1 Detection of inhomogeneous images

On a spatial scale of a few kilometres ocean wave fields should be approximately homogeneous at least in cases where the boundary conditions are constant (constant water depth, constant currents). This means that the statistical moments describing the wave field, e.g. the wave spectrum are shift invariant. The same should then also be true for the SAR image and the respective SAR image variance spectrum. In this section a method is presented which identifies cases where this basic property is violated using ERS-2 imagerette data. One motivation for this investigation is to detect imagerettes, which are contaminated by

- atmospheric phenomena like boundary layer rolls [Alpers and Brümmer, 1994], atmospheric fronts, or rain cells [Melsheimer et al., 1998];
- surface slicks of antropogenic or biological origin [Gade et al., 1998];
- sea ice.

Furthermore, the method is able to detect ocean wave fields with strong spatial dynamics, which are not properly described by a spectrum. These inhomogeneities can be due to different phenomena like e.g.:

- changing water depth;
- inhomogeneous current fields;
- extreme wave grouping, i.e. large distances between wave groups.

All these features spoil SAR wave measurements and must be detected with high reliability.

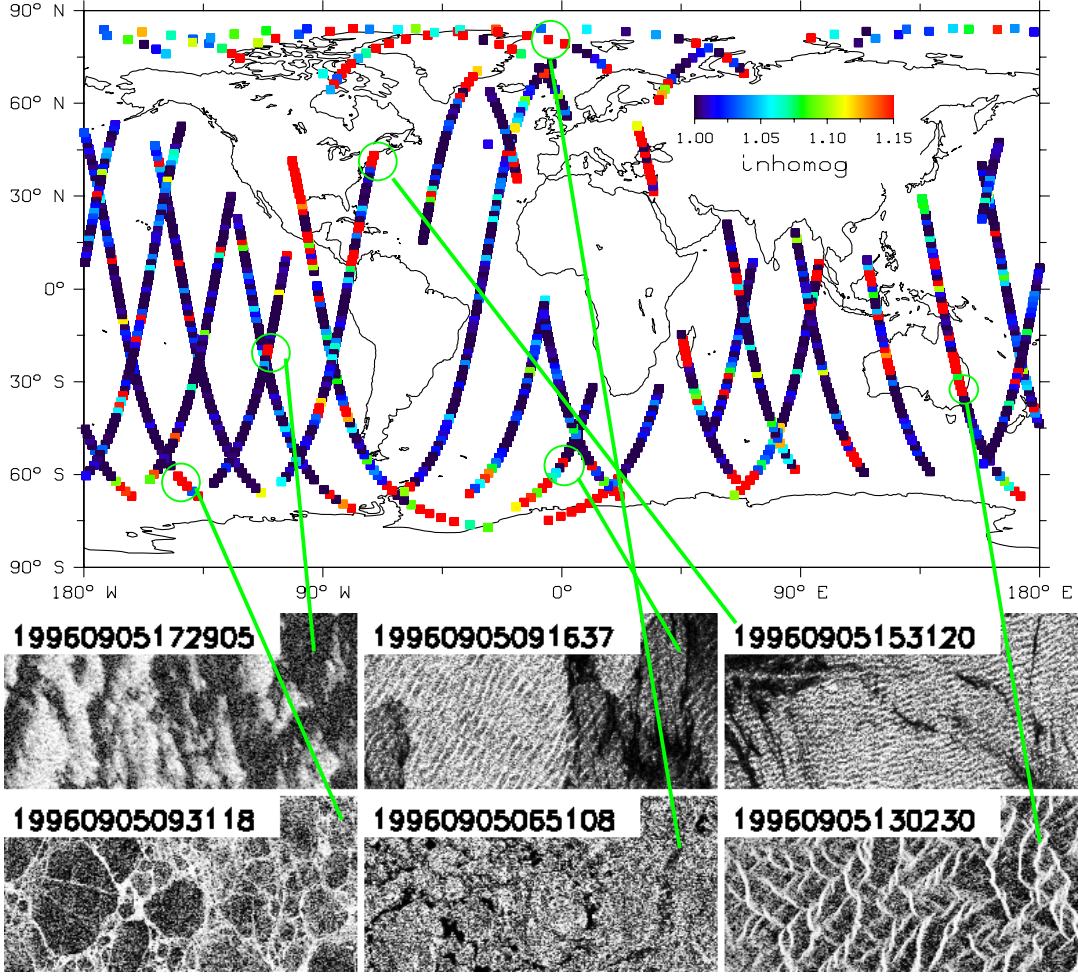


Fig. 8.2: (Top) Global map with inhomogeneity parameter ξ_H derived from ERS-2 wave mode imagettes acquired on Sep 5, 1996. (Bottom) Examples of ERS-2 imagettes, which failed the homogeneity test (i.e. $\xi_H > 1.05$) due to atmospheric and sea ice features as well as land structures.

According to standard spectral estimation theory spectral densities estimated from a single periodogram $\hat{\Phi}$ [Honerkamp, 1993] are negative exponentially distributed, i.e. $\text{var}(\hat{\Phi}_k)$ is equal to $\text{mean}(\hat{\Phi}_k)^2$ for all wavenumber components k . A standard approach to reduce the variance of the spectral estimator is to average periodograms estimated from subimages. To check the homogeneity of wave mode imagettes $N = 32$ subimages of about 1 by 1 km size were used to estimate the mean and variance of the periodogram and to test the above relation between mean and variance of the periodogram. The boxes used for the estimation are shown in Fig. 8.1. The box size is still large enough to resolve even swell systems. The basic idea of the test is to check, whether

$$\frac{\overline{\text{var}(\hat{\Phi}_k)}}{(\overline{\text{mean}(\hat{\Phi}_k)})^2} \approx 1 \quad \text{for all wave number bins } k \quad (8.1)$$

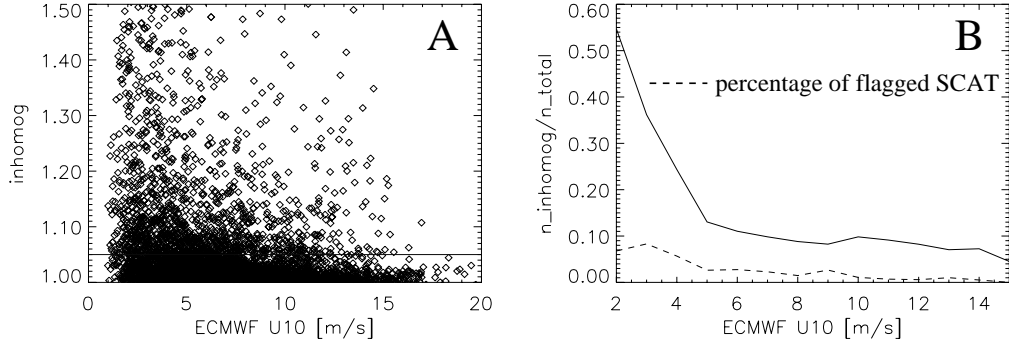


Fig. 8.3: (A) Scatterplot of the inhomogeneity parameter ξ_H versus ECMWF wind speeds. The horizontal line was used as a classification threshold. (B) Percentage of inhomogeneous imageries as a function of ECMWF wind speed (solid line). The dashed line is the respective percentage of flagged ERS scatterometer measurements.

holds. Here, $\overline{\text{mean}}$ denotes the standard estimator for the mean and $\overline{\text{var}}$ is an estimator for the variance of the periodogram defined as

$$\overline{\text{var}}(\hat{\Phi}_k) = \frac{1}{N} \sum_{j=1}^N (\hat{\Phi}_k^j)^2 - \overline{\text{mean}}(\hat{\Phi}_k)^2, \quad (8.2)$$

where $\hat{\Phi}_k^j$ denotes the periodogram of the j th subimage. It should be noted that eq. 8.1 is approximative even if the mean value is taken on the left side. In fact, it can be shown that the expression is slightly biased towards values smaller than one [Oliver and Quegan, 1998].

To avoid the test to be dominated by speckle noise (which is homogeneous) a weighting with spectral energies is introduced leading to the following definition of an inhomogeneity parameter ξ_H :

$$\xi_H = \left(\sum_k \overline{\text{mean}}(\hat{\Phi}_k) \right)^{-1} \sum_k \frac{\overline{\text{var}}(\hat{\Phi}_k)}{\overline{\text{mean}}(\hat{\Phi}_k)} \quad (8.3)$$

The parameter is a weighted average of the expressions given in eq. 8.1 over all wave components k .

Fig. 8.1 (B) shows the histogram of the inhomogeneity parameter estimated from 30000 imageries including land and sea ice. It can be seen that the peak of the distribution is slightly smaller than one, which is consistent with the known bias of the expression in eq. 8.1. To classify the imageries into classes of homogeneous and non-homogeneous cases a threshold of 1.05 was chosen by visual inspection. It turned out that this choice results in a reliable detection of atmospheric fronts, slicks and sea ice.

Fig. 8.2 (top) shows a global map with the inhomogeneity parameter derived from ERS-2 imageries acquired on Sep 5, 1996 given in color coding. It can be seen that the strongest inhomogeneities occur over land and over sea ice. However, inhomogeneous

features are also found in the open ocean. The imagerettes shown at the bottom of Fig. 8.2 are examples, which failed the homogeneity test. The imagerettes on the bottom centre and left and the top centre and right show sea ice with ocean wave patterns visible in the two latter case. The imagerette at the top left shows typical patterns associated with atmospheric phenomena. The remaining imagerette on the lower right was acquired over Australia and shows mountains.

A closer investigation showed that a lot of irregular sea surface features are due to atmospheric phenomena in particular at very low wind speeds. This effect was investigated using collocated ECMWF wind speeds for comparison. Fig. 8.3 (A) shows a scatterplot of the inhomogeneity parameter as a function of wind speed with the threshold introduced above indicated by a horizontal line. The plot in Fig. 8.3 (B) gives the respective percentage of non-homogeneous imagerettes (solid line). One can clearly see, that the ratio increases strongly as the wind speed drops below 5 ms^{-1} . The phenomenon is attributed to the fact that due to surface tension the response of Bragg waves, which dominate the radar return (compare Chapter 4), to the wind is not continuous at very low wind speed. In other words a minimum wind speed is required to produce centimetre waves and these waves disappear abruptly as the wind speed drops below a certain limit. The inhomogeneous image features are thus in many cases believed to be due to small spatial variations of the wind speed around these thresholds. The dashed line in Fig. 8.3 (B) indicates the percentage of collocated ERS-2 scatterometer measurement, which are flagged as unusable. As the dashed line is below the solid line, it seems that a significant number of scatterometer measurements is taken as usable, although the NRCS of the sea surface is strongly inhomogeneous. SAR data thus have the potential to improve the quality of scatterometer measurements as well.

8.2 Comparison of linear SAR measurements with wave model output

For a first check of the global data set of complex imagerettes, the linear inversion scheme described in Chapter 3 is used to obtain a rough estimate of the low wavenumber part of the wave spectrum.

As the linear model is known to be adequate only for longer waves, the comparison of the SAR derived spectra with the WAM model is restricted to waves with periods longer than 10 s, which corresponds to about 160 m in deep water. The corresponding waveheight H_{10} is then calculated from the wave spectrum F_k as

$$H_{10} = 4 \sqrt{\int_{T>10s} F_k d^2k} . \quad (8.4)$$

Likewise, a vector $\bar{\mathbf{k}}$, which contains information about the mean propagation, and wavelength is defined as follows:

$$\bar{\mathbf{k}} = \frac{16}{H_{10}^2} \int_{T>10s} \mathbf{k} F_k d^2k \quad (8.5)$$

In order to compare the mean wave directions of the wave model and the linear SAR measurement, for each pair of collocated spectra a complex number W defined as

$$W = \exp \left[i \left(\text{atan}(\bar{k}_y^{WAM}, \bar{k}_x^{WAM}) - \text{atan}(\bar{k}_y^{SAR}, \bar{k}_x^{SAR}) \right) \right] H_{10}^{SAR} \quad (8.6)$$

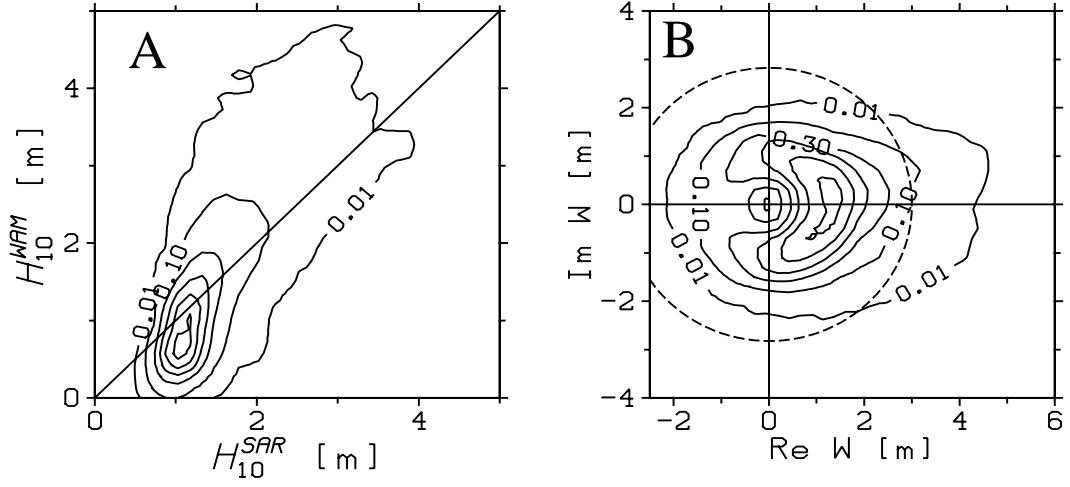


Fig. 8.4: (A) Scatterplot of wave height H_{10}^{SAR} derived from SAR cross spectra using a linear inversion technique without prior information and respective wave height H_{10}^{WAM} calculated with the WAM model. (B) Scatterplot of the function W defined in eq. 8.6. The distance to the origin indicates the wave height H_{10}^{SAR} derived from SAR, whereas the direction gives the difference of the mean wave propagation directions as derived from SAR and WAM. The difference is zero for points on the positive part of the horizontal axis.

is calculated.

Wave spectra were retrieved from 15000 imagerettes, which passed the homogeneity test and for which collocated ECMWF spectra were available. The time gap between SAR observations and model spectra is less than 3 hours and the spatial distance is less than 100 km.

Fig. 8.4 (A) shows a scatterplot of SAR derived wave height H_{10}^{SAR} versus the respective WAM wave height H_{10}^{WAM} . One can see that, although the measurement is restricted to longer waves, the linear SAR measurement still underestimates with respect to the WAM model, apparently due to the azimuthal cut-off. The observed problem will be addressed in Section 9, where an inversion scheme is introduced, which takes into account nonlinear imaging effects and adds missing information beyond the azimuthal cut-off wavenumber. Fig. 8.4 (B) shows the distribution of the numbers W defined in eq. 8.6 in the complex plane. The modulus of W corresponds to the waveheight H_{10} as derived from SAR, whereas the phase of W indicates the difference of mean directions derived from the SAR spectrum and the corresponding ECMWF spectrum. The points on the positive part of the real axis indicate perfect agreement. It can be seen that for waveheights less than 1 m the phase of W has a more or less isotropic distribution, i.e. there is hardly any correlation between the propagation directions in the model and the respective SAR measurement. However, for higher waves W is clearly clustering around the positive real axis, showing that the propagation directions derived from SAR are in good agreement with the model in this case. The above observation is consistent with the theoretical investigation presented in Chapter 6. The lack of agreement between model and SAR measurement at low wave heights can be explained by the low signal to noise ratio expected for the

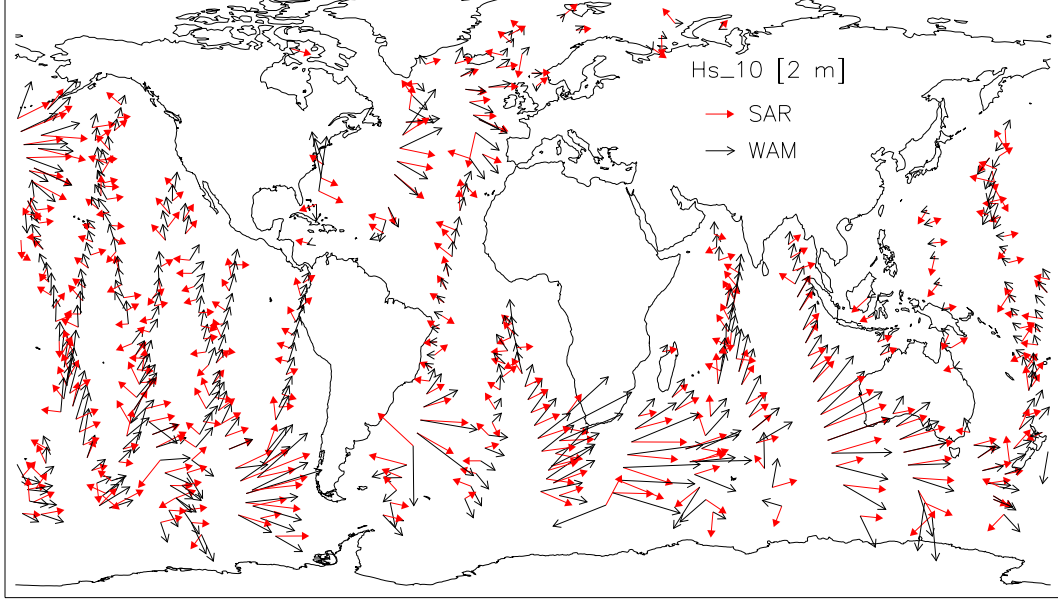


Fig. 8.5: Global map showing mean propagation directions (red arrows) derived from complex ERS-2 wave mode imagerettes acquired on Sep 5, 1996. The black arrows indicated the respective direction derived from collocated WAM model data. For the computation of the mean direction only waves with periods longer than 10 s were taken into account. The arrow length corresponds to the waveheight H_{10} defined in eq. 8.4.

SAR spectrum in these cases. The low coherence predicted under these circumstances (compare eq. 6.7) necessarily leads to high phase noise in the cross spectrum (compare Fig. 6.2).

A global map with the mean directions and waveheights derived from SAR and model data is given in Fig. 8.5 for imagerettes acquired on Sep 5, 1996. One can see that there is in fact good agreement of wave propagation directions in case of higher waves, in particular for the storm generated wind seas in the “rolling fourties”. The few cases where stronger deviations are seen are mostly due to complex sea states with more than one wave system. In these cases the mean direction strongly depends on the relative weighting of the different wave components. The map also exhibits a clear limitation of the linear inversion technique, which is obviously not able to fully reverse the velocity bunching effect. This shortcoming leads to the obvious tendency of the mean SAR direction to be rotated in the range direction with respect to the respective model direction.

One should point out however that the dominance of range travelling waves in the observed SAR spectra is not solely due to the SAR imaging process. To demonstrate this, Fig. 8.6 (A) shows the average cross spectrum energy computed as

$$\eta_k = \frac{1}{N} \sum_{\text{Im}(\Phi^i(k)) > 0} |\Phi_k^i| \quad (8.7)$$

in the range azimuth reference system of the sensor. The azimuthal low pass filtering of the cross spectra is clearly visible. In addition, the average spectrum is nearly

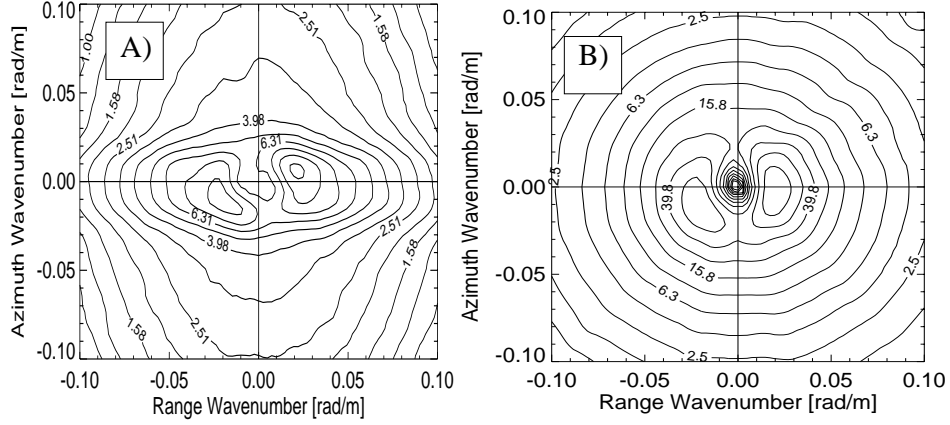


Fig. 8.6: (A) Distribution of cross spectrum energy as defined in eq. 8.7 derived from 1000 ERS-2 imageries. (B) Respective average of the collocated ECMWF ocean wave spectra.

symmetric indicating wavesystems of about 300 m wavelength propagating in approximate range direction. The corresponding average ECMWF ocean wave spectrum is given in Fig. 8.6 (B), showing remarkable agreement with the observed cross spectra. In particular one can see that range travelling waves, which are mainly associated with the strong westerly winds at the southern hemisphere, are dominating in the ocean wave model, too.

8.3 Comparison of cross spectra phase with linear wave theory

To study the statistics of the measured cross spectrum phase, the respective energy distribution was analysed. The range and azimuth dimensions are investigated separately by computing the following functions:

$$Q_x(k_x, \varphi) = \sum_i \delta_\epsilon \left(\arg(\Phi^i(k_x, 0)) - \varphi \right) |\Phi^i(k_x, 0)| \quad (8.8)$$

$$Q_y(k_y, \varphi) = \sum_i \delta_\epsilon \left(\arg(\Phi^i(0, k_y)) - \varphi \right) |\Phi^i(0, k_y)| \quad (8.9)$$

Here, δ_ϵ is a box function given by

$$\delta_\epsilon(x) = \begin{cases} 1 & : |x| \leq \epsilon \\ 0 & : \text{else} \end{cases}, \quad (8.10)$$

and N is a counter for the global data set of cross spectra. For the computation presented here, ϵ was chosen as 1° resulting in a reasonable resolution of the phase. Q_x and Q_y provide the energy distribution over the phase interval $[0, 2\pi]$ for different range and azimuth travelling wave components respectively. Fig. 8.7 shows contour plots of the two functions estimated from $N=10000$ complex imageries. Only imageries passing the inhomogeneity test were used to avoid artefacts associated with

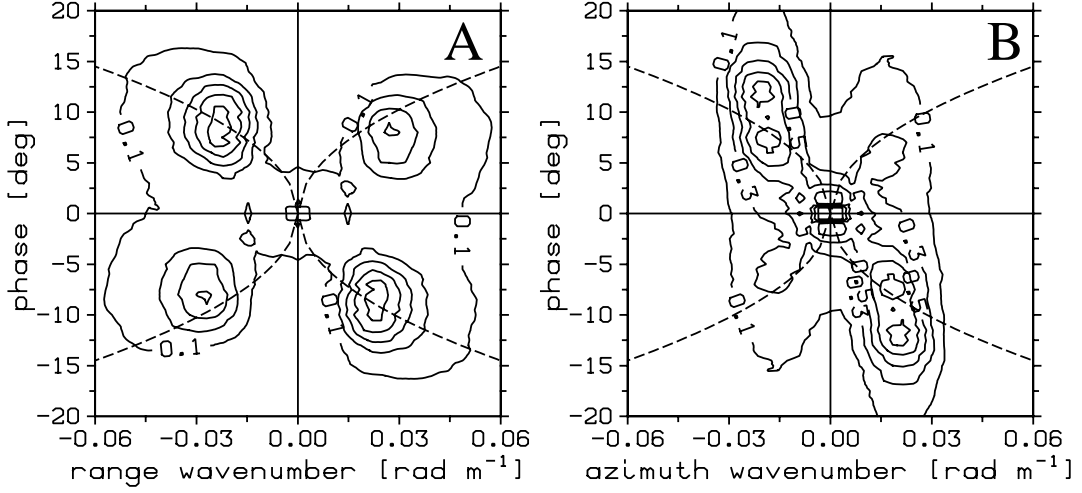


Fig. 8.7: Distribution of cross spectrum energy in the wavenumber/phase plane for range travelling waves (A) and azimuth travelling waves (B) respectively (compare eq. 8.8 and eq. 8.9). The distribution was estimated from a global data set of 10000 cross spectra with a look separation time of $\Delta t = 0.33$ s. The dashed curves represent the theoretical phase for ocean waves propagating in deep water (compare eq. 2.10).

sea ice or atmospheric phenomena. The dashed curves in both plots represent the theoretical phase expected within the linear theory for deep water. One can see that for both range and azimuth travelling waves there is reasonable agreement between the theoretical and measured phase. For the range case we see that the maxima of Q_y are located at wavelengths between 200 m to 250 m. The maxima are only slightly below the theoretical values. There are two possible explanation for the remaining deviations:

- The data set contains shallow water cases, which have a reduced phase speed (compare eq. 2.10).
- The simple definition of the look separation time Δt , which refers to the centre (compare Fig. 6.7) of the extracted frequency bands, does not take into account the weighting associated with the azimuth antenna pattern. As the neighbouring parts of the look bands have a higher signal to noise ratio than the remaining part, the effective look separation is likely to be slightly shorter than the distance of the look centres.

For the azimuth case shown in Fig. 8.7 (B), one can see that the energy is stretched over a longer interval of phases exceeding the theoretical value. This finding can be attributed to non-linear imaging effects, which dominate in the azimuth direction; shorter waves travelling in flight direction are “bunched” towards the range axis, i.e. they appear with longer wavelength on the SAR image.

Chapter 9

AN OCEAN WAVE RETRIEVAL SCHEME FOR SAR CROSS SPECTRA

As demonstrated in the previous chapters, the information SAR provides on the two-dimensional ocean wave spectrum has limitations in particular for shorter waves propagating in the azimuth direction. SAR look cross spectra have shown their capability to resolve the ambiguity of wave propagation direction present in conventional SAR image variance spectra, but the information loss caused by nonlinear SAR imaging effects, like the azimuthal cut-off still exists. One can of course try to restrict the SAR measurement to the long wave regime, which is less affected by nonlinear mechanism as shown in the previous chapter, however for practical applications like, e.g. wave model assimilation this approach is not really satisfactory. The main reason is the fact that due to the strong coupling of different wave components in the imaging process there is no obvious separation of the spectral regime in regions of linear and nonlinear wave mapping.

The type of ill conditioned problem described above is very common in remote sensing and is usually solved by using some a priori information from other sources, like numerical models or different sensors. Attempts to find solutions without prior information have been made [Lyzenga, 2002], but the applicability seems to be very limited and a statistical analysis was not carried out. For conventional SAR image variance spectra different approaches have been proposed to blend SAR measurement and prior knowledge. Hasselmann *et al.* [1996] and Krogstad *et al.* [1994] used model spectra as prior information, whereas Mastenbroek and de Valk [2000] took collocated ERS-2 scatterometer measurements as additional input. Several studies showing the performance of the schemes have been carried out [Heimbach *et al.*, 1998; Mastenbroek and de Valk, 2000; Breivik *et al.*, 1998].

In this section a retrieval scheme for the derivation of two-dimensional ocean wave spectra from look cross spectra as, e.g. provided by the ENVISAT ASAR operating in wave mode is presented using prior information. A first very general study on this issue without statistical analysis was presented in Dowd and Vachon [2001], where discontinuities of the retrieved spectra at the cut-off wavenumber were identified as the main problem. As we will show, the scheme presented in this chapter is able to solve this problem. The method proposed here extends the basic concepts of the inversion scheme introduced in Hasselmann *et al.* [1996], which are:

- The scheme uses two-dimensional wave spectra provided by numerical models as a priori information.
- The method is based on a parameterisation of the prior wave spectrum using a partitioning approach.

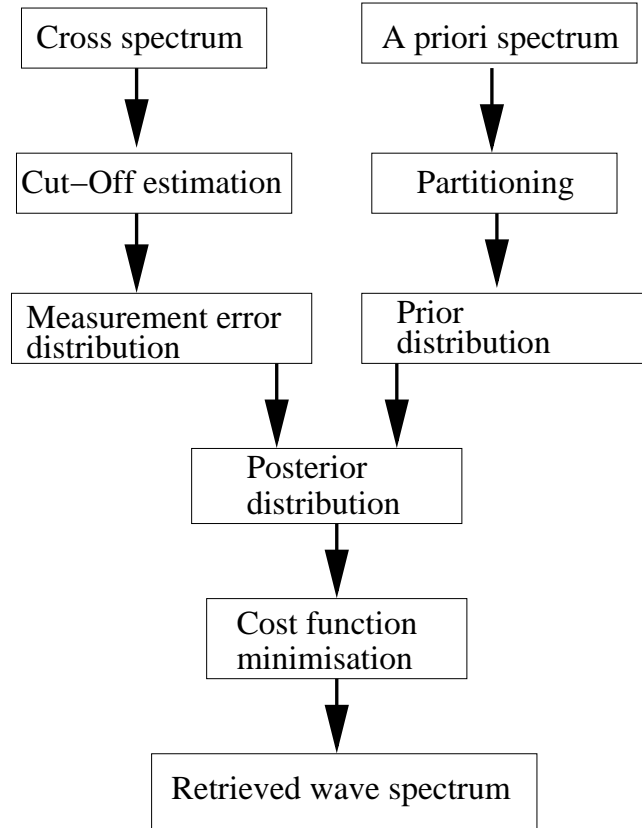


Fig. 9.1: Flowchart of the PARSA retrieval scheme

The method described in this chapter is referred to as PARSA (**partition rescale and shift algorithm**) in the following. It has several additional features compared to the scheme described in *Hasselmann et al.* [1996]:

- The scheme has the directional spreading of the different wave systems as an additional parameter.
- The algorithm is based on explicit models for the measurement error, errors in the forward model, and uncertainties in the prior wave spectrum.
- The scheme is based on a maximum a posteriori approach. The second iteration loop used in *Hasselmann et al.* [1996], where the prior wave spectrum is adjusted and fed back into the optimal estimation problem is avoided. This approach has two advantages:
 - The sensitive cross assignment procedure used in *Hasselmann et al.* [1996] is not required.
 - Based on the rigorous formulation as an optimal estimation problem it is possible to estimate the error covariance of the retrieved parameters.
- The scheme makes use of the phase information contained in cross spectra to resolve ambiguities in wave propagation direction.

- The side condition $F_k \geq 0$ is treated in a rigorous way.

The design of the PARSA scheme was guided by the requirements of wave model assimilation, which is regarded as the most important application of global SAR data as provided by the ENVISAT ASAR.

The chapter is structured as follows. In the first section the basic formulation of SAR ocean wave retrieval as an optimal estimation problem is introduced. A model for the measurement error based on results obtained in Chapter 6 as well as for errors in the forward model and uncertainties in the prior wave spectrum are presented in Section 9.2. Section 9.3 is about the numerical retrieval procedure, which is based on a Levenberg-Marquard method. The discussion includes criteria for the termination of the iteration and the computation of error covariance matrices for the retrieved wave parameters. In Section 9.4 the performance of the scheme is illustrated using simulated data. In particular, the benefit of the phase information contained in cross spectra is demonstrated. In the final section the PARSA scheme is applied to the global data set of reprocessed ERS-2 cross spectra introduced in Chapter 5. Global maps as well as scatterplots comparing retrieved and prior wave spectra are presented.

9.1 Retrieval strategy

As explained above, one essential task in SAR ocean wave retrieval is to blend SAR information and prior knowledge in some consistent way. The strategy followed in this study is based on the so called maximum a posteriori approach. The objective of this concept is to maximise the conditional probability of the retrieved wave spectrum given the SAR measurement and the prior information. Using the Bayes theorem the respective probability density function (pdf) can be written as

$$\text{pdf}(F_k, \alpha | \Phi_k) = \frac{\text{pdf}(\Phi_k | F_k, \alpha) \text{pdf}(\alpha) \text{pdf}(F_k)}{\text{pdf}(\Phi_k)}, \quad (9.1)$$

where the factors in this equation have the following meanings:

- $\text{pdf}(\Phi_k | F_k, \alpha)$: conditional distribution of the measured cross spectrum Φ_k given an ocean wave spectrum F_k and a forward model, which contains a stochastic parameter vector α .
- $\text{pdf}(\alpha)$: prior distribution of parameters in the forward model
- $\text{pdf}(F_k)$: prior distribution of the ocean wave spectrum F_k .
- $\text{pdf}(\Phi_k)$: prior distribution of the cross spectrum, which is irrelevant for the inversion procedure.

The overall structure of the retrieval scheme based on eq. 9.1 is depicted in a flowchart in Fig. 9.1. The different components will be explained going from top to bottom, starting with probability models for both cross spectra estimation errors and uncertainties in the prior wave spectrum.

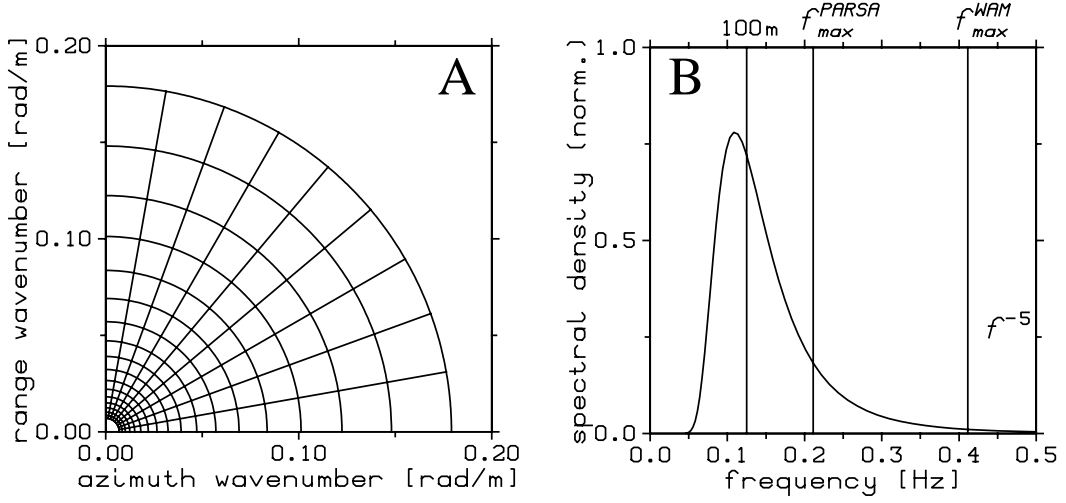


Fig. 9.2: (A) Polar grid used in the PARSA retrieval scheme with 10° directional resolution and wavenumber spacing equivalent to the frequency grid used in the WAM model (for deep water). (B) Relevant spectral regimes in the frequency domain. The maximum frequencies in the WAM model and the PARSA scheme are denoted by f_{max}^{PARSA} and f_{max}^{WAM} respectively. For the computation of the orbital velocity variance $\rho^u(\mathbf{0})$ spectral energy above f_{max}^{PARSA} is taken into account.

9.2 Error models

9.2.1 Measurement errors

For an optimal wave spectra retrieval it is necessary to quantify the potential errors contained in the cross spectra measurement. The analysis in Section 6 showed that the correlation of the errors of the real and imaginary part of the cross spectrum is low (<0.5) for typical coherence values and wave phase speeds. Using a second order model for the measurement error we therefore neglect the off-diagonal elements in the covariance matrix and only take into account the variances of the real and imaginary part as given by the diagonal elements of the matrix given in eq. 6.22. Denoting the exact cross spectrum with $\overline{\Phi}_k^{obs}$, the estimated spectrum is written as

$$\Phi_k^{obs} = \overline{\Phi}_k^{obs} + \epsilon_k^S \quad (9.2)$$

where ϵ_k^S is a zero mean complex Gaussian process with standard deviation given by

$$\text{stdv}(\epsilon_k^S) \approx \frac{|\Phi_k^{I^1 I^1}|}{N} (0.75, 0.25) =: (\sigma_k^{RS}, \sigma_k^{IS}), \quad (9.3)$$

which has to satisfy $\epsilon_k^S = (\epsilon_{-k}^S)^*$. Here, N is the number of averaged samples used in the cross spectrum estimation. For simplicity, we have furthermore assumed an average coherence of 0.7, which is regarded as typical. Alternatively, the coherence can be estimated for each measurement separately as discussed in Chapter 6.

To keep the computational effort low, the PARSA scheme uses a polar grid as shown in Fig. 9.2 (A) with $n_k = 18$ wavenumbers, which for deep water corresponds

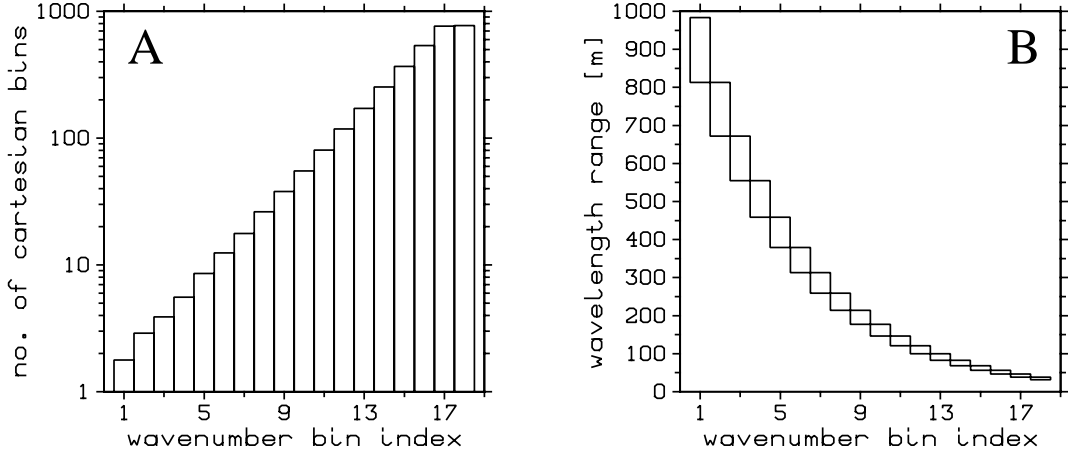


Fig. 9.3: (A) Average number N of cartesian grid points contained in the wavenumber bins used in the PARSA scheme (compare eq. 9.4). An image size of 10 by 5 km was assumed corresponding to the ERS wave mode. (B) Respective range of wavelength for each bin.

to the frequencies in the polar grid of the WAM model, i.e.

$$k_j = \frac{4\pi^2 f_0^2}{g} 1.1^{j-1} \quad j = 1, \dots, n_k \quad (9.4)$$

with f_0 defined in eq. 5.4. The range of wavelength is between 35 m and 895 m. The grid has $n_\Phi = 36$ equally spaced directions, which is in agreement with the grid of the official ENVISAT cross spectra product (compare Fig. 5.5). Fig. 9.3 (A) shows the average number N of cartesian grid points contained in the logarithmic wavenumber bins. The respective range of wavelengths is given in Fig. 9.3 (B). One can see that for shorter waves the number of averaged spectral bins is so high that the impact of estimation errors on the retrieval (compare eq. 9.3) becomes negligible. However, for longer swell it has to be taken into account.

9.2.2 Uncertainties in the forward model

It is well known that the SAR ocean wave imaging model contains significant uncertainties. In particular, the phase and magnitude of the RAR modulation mechanism is known only with low accuracy [Brüning *et al.*, 1994; Schmidt, 1995]. This circumstance is only to some degree due to the lack of respective measurements, but there is some indication that the RAR modulation mechanism itself has stochastic components [Schmidt, 1995].

To take into account uncertainties in the forward model, we assume that the simulated cross spectrum Φ^{sim} calculated according to the nonlinear integral transform given by eq. 4.25 can deviate from the “true” cross spectrum denoted by $\bar{\Phi}$. The proposed error model has three components, which refer to different characteristic features of the cross spectrum and can be written as:

$$\bar{\Phi}_k = \alpha_1 \exp[-k_x^2 \alpha_2] \Phi_k^{sim} + \epsilon_k^F \quad (9.5)$$

σ_{α_1}	σ_{α_2}	$\sigma_{\nu_{RF}}$	$\sigma_{\nu_{IF}}$
0.2	250 m ²	0.1	0.1

Tab. 9.1: Standard deviations of the parameters α_1 , α_2 , ν_{RF} and ν_{IF} used to describe errors in the SAR ocean wave imaging model (compare eq. 9.5).

Here, α_1, α_2 and ϵ_k^F have the following meanings:

- α_1 is a Gaussian distributed variable with unit mean and standard deviation σ_{α_1} , which describes errors in the overall energy level of the spectrum, as e.g. caused by uncertainties in the magnitude of the RAR MTF.
- α_2 is a Gaussian distributed variable with zero mean and standard deviation σ_{α_2} , which describes uncertainties in the cut-off wavelength of the forward model.
- ϵ_k^F is additive white Gaussian noise with independent real and imaginary part and zero mean, which has to satisfy $\epsilon_k^F = (\epsilon_{-k}^F)^*$. It is supposed to take into account errors in the fine scale structure of the spectrum, e.g. caused by errors in the phase of the RAR MTF

For the standard deviation of ϵ^F we assume relative errors for both real and imaginary part of the cross spectrum, i.e.

$$\text{stdv } \epsilon_k^F = (\sigma_k^{RF}, \sigma_k^{IF}) = (\nu_{RF} \max_k |\text{Re}\Phi_k^{obs}|, \nu_{IF} \max_k |\text{Im}\Phi_k^{obs}|) . \quad (9.6)$$

Here, ν_{RF} and ν_{IF} denote the expected error in the fine scale structure of the real and imaginary part expressed as a fraction of the respective maximum values.

Combining the models for estimation errors and uncertainties in the forward model, the conditional probability of the measured cross spectrum given an ocean wave spectrum F_k and a parameter vector α is given by

$$\begin{aligned} \text{pdf}(\Phi_k | F_k, \alpha) \sim & \prod_k \exp \left[-\frac{(\text{Re}(\alpha_1 e^{-k_x^2} \alpha_2 \Phi_k^{sim} - \Phi_k))^2}{2 (\sigma_k^{RF})^2 + 2 (\sigma_k^{RS})^2} \right] \\ & \prod_k \exp \left[-\frac{(\text{Im}(\alpha_1 e^{-k_x^2} \alpha_2 \Phi_k^{sim} - \Phi_k))^2}{2 (\sigma_k^{IF})^2 + 2 (\sigma_k^{IS})^2} \right] , \end{aligned} \quad (9.7)$$

where it was assumed that both error contributions are independent. Table 9.1 summarises the standard deviations assumed for the model describing uncertainties in the cross spectrum forward model. As the standard deviation defines the 65% confidence interval for a Gaussian distributed variable, it is thus expected, that the given deviations of the parameters from their mean values will be exceeded in about 35% of the cases.

The values given in table 9.1 represent estimates of the uncertainties, which are regarded as reasonable. They should be seen as a first guess of more accurate estimates, which are expected from a statistical analysis of the retrieval results. The problem of a straightforward estimation of the parameters by, e.g. comparing cross spectra simulated from wave model data with the collocated SAR measurements lies in the fact that the observed deviations are due to both the errors in the imaging model and the wave model.

9.2.3 Statistical model for the ocean wave model spectrum

The prior information needed for the SAR wave spectra retrieval can be either taken from collocated measurements of other sensors [Mastenbroek and de Valk, 2000] or from models [Hasselmann et al., 1996; Krogstad et al., 1994]. In Mastenbroek and de Valk [2000] ERS scatterometer measurements, which are exactly collocated in time and space with the corresponding wave mode acquisition were used to add the missing information beyond the cut-off wavelength. Although, it is certainly reasonable to use additional and independent measurements, the approach is not followed in this study mainly for two reasons:

- The most important application of the presented retrieval scheme is the inversion of ASAR wave mode data provided by ENVISAT, which does not carry a scatterometer.
- The method proposed in Mastenbroek and de Valk [2000] is based on a simple parametric JONSWAP type model describing the relation between wind speed U_{10} and the corresponding wind sea. In this study wind sea spectra calculated with a third generation numerical ocean wave model are used as prior information. These spectra are believed to be more realistic, because they contain the best available information about the history of the wind field and the wave dynamics.

The approach of this study is to take the overall shape of the spectrum from a numerical ocean wave model and to use the SAR information to adjust parameters like wavelength, wave height, directional spreading and propagation direction. The statistical model used for the prior spectrum is based on a partitioning scheme, where the wave spectrum F is split into different wave systems B^i using the inverted catchment algorithm proposed in Gerling [1992]. The wave spectrum can then be written as

$$F_k = \sum_{i=1}^{n_p} B_k^i, \quad (9.8)$$

where n_p is the number of partitions. The method is defined by a simple induction rule, which connects every grid point with the neighbouring point of highest energy.

For each subsystem a stochastic model is used, which prescribes the probability that the energy, the propagation direction, the wavelength, or the directional spreading deviates from the prior spectrum. Using a polar grid (Φ, k) for the partitions B^i , the corresponding processes \tilde{B}^i can be written as

$$\tilde{B}^i(\Phi, k) = X_E^i X_{\Delta\Phi} X_k^i B^i\left(\Phi_0^i + (\Phi - X_{\Phi}^i - \Phi_0^i) X_{\Delta\Phi}, X_k^i k\right) \quad i = 1, \dots, n_p \quad (9.9)$$

where Φ_0^i is the peak direction of the i th partition. The definition of the partition process ensures that

$$\int \tilde{B}^i(\Phi, k) d\Phi dk = X_E^i \int B_k^i d\Phi dk \quad i = 1, \dots, n_p \quad (9.10)$$

i.e. rotations, shifts, and changes in directional spread keep the total energy constant. The variance contribution from the i th partition is thus solely controlled by the

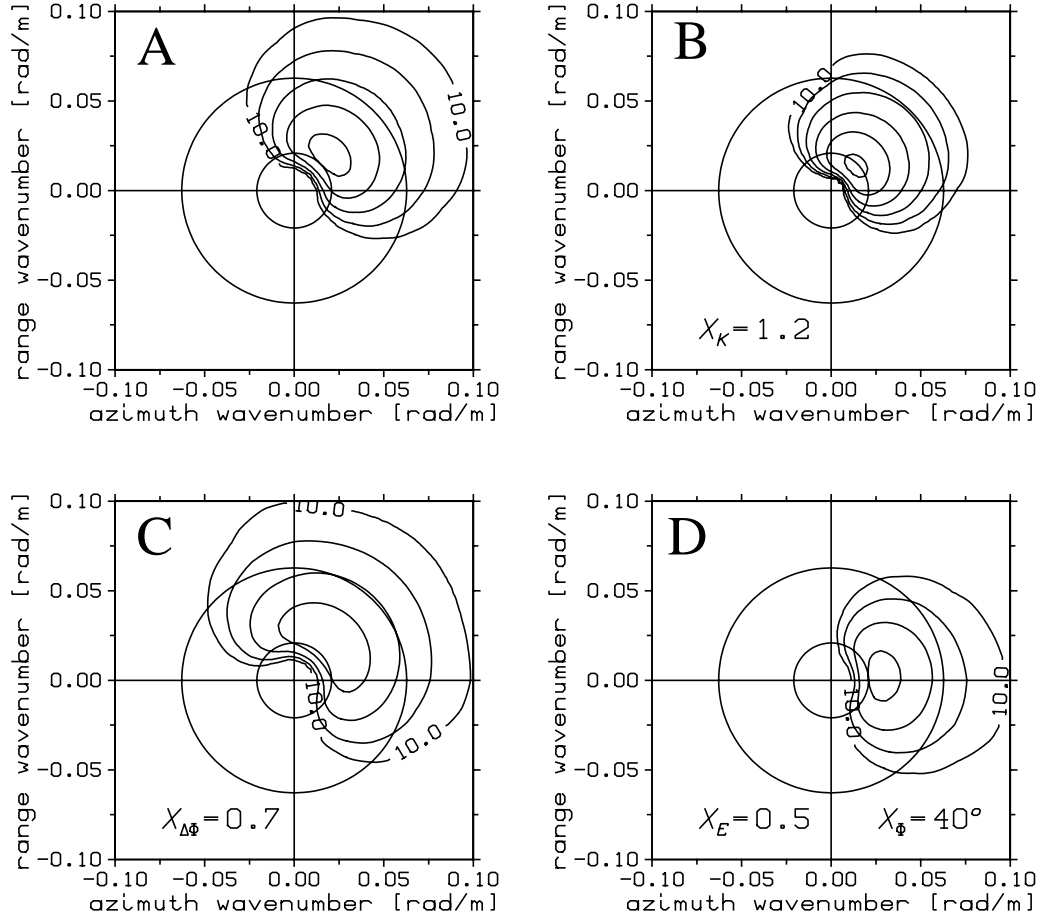


Fig. 9.4: Transformations of wave systems used in the PARSA retrieval scheme (compare eq. 9.9). (A) Prior wave system with 250 m peak wavelength. (B-D) Transformed wave spectra with wavenumbers rescaled (B), directional spreading changed (C) and simultaneous rotation and energy rescaling (D).

parameter X_E^i . Furthermore, the approach of changing the wavelength by rescaling of the wavenumber ensures that power laws in k , e.g. the k^{-4} high frequency tail of wind seas, is maintained by the transformation (compare eq. 2.26).

For a given set of transformation parameters the corresponding spectrum is computed with a bilinear interpolation method, which turned out to give sufficiently smooth results. Fig. 9.4 illustrates the different transformations used in the PARSA scheme. The prior spectrum with a single wave system of 250 m wavelength is shown in Fig. 9.4 (A). The four possible transformations applied to this system are demonstrated in Fig. 9.4 (B)-(D). One can see that the wavenumber rescaling factor of $X_k = 1.2$ shifts the peak wavelength from 250 m to 300 m. The directional spreading is increased if the parameter $X_{\Delta\Phi}$ is less than one and vice versa.

σ_E	σ_k	σ_Φ	$\sigma_{\Delta\Phi}$
0.1	0.1	20°	0.1

Tab. 9.2: Standard deviations of the parameters used for the model describing errors in the prior wave spectrum (compare eq. 9.9).

The 4 transformation parameters for each partition are collected in a vector $\hat{\mathbf{X}}^i$

$$\hat{\mathbf{X}}^i = (X_E^i, X_k^i, X_\Phi^i, X_{\Delta\Phi}^i) \quad i = 1, \dots, n_p \quad . \quad (9.11)$$

The vector $\hat{\mathbf{X}}^i$ is assumed to be Gaussian distributed with independent components, and with mean given by:

$$\boldsymbol{\nu}^i = \langle (X_E^i, X_k^i, X_\Phi^i, X_{\Delta\Phi}^i) \rangle = (1, 1, 0, 1) \quad i = 1, \dots, n_p \quad (9.12)$$

The standard deviation is defined as:

$$\text{stdv}\left((X_E^i, X_k^i, X_\Phi^i, X_{\Delta\Phi}^i)\right) = (\sigma_E^i, \sigma_k^i, \sigma_\Phi^i, \sigma_{\Delta\Phi}^i) \quad i = 1, \dots, n_p \quad (9.13)$$

The different partition processes are in a first approximation assumed to be independent. This is justified, because in the typical situation one has a wind sea driven by the local wind field and swell systems, which were generated by storm events far away in time and space. The prior wave spectrum can then be expressed as:

$$\tilde{F}(\hat{\mathbf{X}}^1, \dots, \hat{\mathbf{X}}^{n_p}) = \sum_{i=1}^{n_p} \tilde{B}^i(\hat{\mathbf{X}}^i) \quad (9.14)$$

In summary, the prior pdf of the wave spectrum can be written as

$$\text{pdf}(\overline{\mathbf{X}}) \sim \prod_{i=1}^{4n_p} \exp\left[-\frac{(\overline{\mathbf{X}}_i - \overline{\nu}_i)^2}{2\overline{\sigma}_i^2}\right] \quad , \quad (9.15)$$

where the partition parameters $\hat{\mathbf{X}}^i$ were collected into a vector $\overline{\mathbf{X}}$ of dimension $4n_p$.

$$\overline{\mathbf{X}} = (\hat{\mathbf{X}}^1, \dots, \hat{\mathbf{X}}^{n_p}) \quad (9.16)$$

The respective mean and standard deviation are defined accordingly:

$$\begin{aligned} \overline{\nu} &= \langle \overline{\mathbf{X}} \rangle \\ \overline{\sigma} &= \text{stdv}(\overline{\mathbf{X}}) \end{aligned} \quad (9.17)$$

The statistical parameters used for the model describing errors in the prior model are summarised in table 9.2. Again the given parameters are regarded as reasonable, however it is clear that the values strongly depend on the performance of the numerical model used to compute the prior wave spectrum, as well as the quality of the driving wind fields. It is obvious that any user of wave model data would benefit from knowledge about parameters like the ones used in this study and we think that it is simply a question of time until such information will be provided by weather centres on a routinely basis.

9.3 Numerical inversion procedure

Inserting eq. 9.7 and eq. 9.15 in eq. 9.1 and taking the logarithm we see that maximising the conditional probability density pdf($F_k, \alpha | \Phi_k$) is equivalent to minimising the following cost function

$$J(\mathbf{X}) = \sum_k \frac{(\text{Re}(\alpha_1 e^{-k_x^2 \alpha_2} \Phi_k^{sim} - \Phi_k^{obs}))^2}{(\sigma_k^{\text{Re}\Phi})^2} + \frac{(\text{Im}(\alpha_1 e^{-k_x^2 \alpha_2} \Phi_k^{sim} - \Phi_k^{obs}))^2}{(\sigma_k^{\text{Im}\Phi})^2} + \sum_{i=1}^{4n_p+2} \frac{(\mathbf{X}_i - \mathbf{X}_i^a)^2}{\sigma_i^2}, \quad (9.18)$$

where $\sigma^{\text{Re}\Phi}$ and $\sigma^{\text{Im}\Phi}$ are defined by (compare eq. 9.6 and eq. 9.3)

$$\begin{aligned} (\sigma^{\text{Re}\Phi})^2 &= (\sigma_k^{RS})^2 + (\sigma_k^{RF})^2 \\ (\sigma^{\text{Im}\Phi})^2 &= (\sigma_k^{IS})^2 + (\sigma_k^{IF})^2. \end{aligned}$$

The state vector \mathbf{X} is given by (compare eq. 9.16 and eq. 9.5)

$$\mathbf{X} = (\bar{\mathbf{X}}, \alpha_1, \alpha_2), \quad (9.19)$$

and mean and standard deviation are defined accordingly as

$$\begin{aligned} \mathbf{X}^a &= (\bar{\nu}, 1, 0) \\ \sigma &= (\bar{\sigma}, \sigma_{\alpha_1}, \sigma_{\alpha_2}). \end{aligned}$$

Eq. 9.18 represents a nonlinear minimisation problem with $4n_p + 2$ variables, which is solved on the grid introduced in Section 9.2.1, i.e. the index k in the summation refers to the bins of the polar grid.

Fig. 9.2 (B) shows the range of frequencies covered by the PARSA grid and the WAM grid. It is important to note that the ocean wave imaging process is influenced by waves with frequencies higher than f^{PARSA} and f^{WAM} . This is simply due to the fact that these waves contribute significantly to the orbital velocity variance as already discussed in Chapter 7. To take these waves into account the variance contribution of waves between f^{PARSA} and f^{WAM} is taken from the model spectrum. The effect of waves shorter than f^{WAM} is estimated assuming a f^{-5} power law as explained before (compare eq. 7.14).

9.3.1 Levenberg Marquardt Method

The inversion procedure is based on an iterative correction of the unknown vector \mathbf{X}

$$\mathbf{X}^{(n+1)} = \mathbf{X}^{(n)} + \Delta \mathbf{X}, \quad (9.20)$$

in each step replacing the non-linear minimisation problem eq. 9.18 by a quadratic approximation, which is equivalent to a system of linear equations.

The inversion is performed on a polar grid with $n_\phi \times n_k = 18 \times 36 = 648$ bins, which is an order of magnitude lower than the typical number of spectral bins of

cartesian grids (e.g. $128 \times 128 = 16384$) used in *Hasselmann et al.* [1996] or *Krogstad et al.* [1994]. The reduced dimension is a key point in the proposed retrieval scheme as the numerical solution of the resulting linear equations becomes feasible even if there is a coupling between different wave components, i.e. the respective matrices are non-diagonal.

The moderate dimension of the polar grid is, e.g. beneficial for the linearisation of the forward model. The most straightforward approach would be to replace the full nonlinear model with the quasi-linear approximation eq. 4.31 as done in *Hasselmann and Hasselmann* [1991]. A disadvantage of this approach is the fact that the change of the cut-off factor resulting from a correction of the wave spectrum is not represented in the resulting quadratic problem. A way to deal with this problem was later presented in *Hasselmann et al.* [1996] adding an explicite cut-off term in the cost function. In this study we try to avoid the problem right away by extending the quasi-linear approximation, such that the change of the azimuthal cut-off is explicitly contained. The following non-diagonal approximation of the Jacobian matrix is used to achieve this:

$$\begin{aligned} \frac{\partial \Phi_k}{\partial F_{k'}} \approx & 0.5 \exp[-k_x^2 \langle \xi^2 \rangle] |T_{k'}^S|^2 (\delta_{k-k'} \exp[i \omega_k \Delta t] + \delta_{k+k'} \exp[-i \omega_k \Delta t]) \\ & - \beta^2 k_x^2 |T_{k'}^u|^2 \Phi_k d\mathbf{k} \end{aligned} \quad (9.21)$$

Here, T^S and T^u are the SAR and orbital velocity transfer functions as defined in eq. 4.30 and eq. 4.22 respectively. The approximation follows by applying the product rule to eq. 4.25 and approximating the derivative of the integral expression by the respective derivative at $F = 0$.

Denoting the correction of the vector \mathbf{X} at the n th iteration step with $\Delta \mathbf{X}$ the resulting change ΔF^n of the wave spectrum F is given by

$$\Delta F_k^n = \sum_{i=1}^{4n_p} \Delta \mathbf{X}_i \frac{\partial F_k}{\partial \mathbf{X}_i} . \quad (9.22)$$

The partial derivatives of the wave spectrum with respect to the parameter vector \mathbf{X} are estimated based on eq. 9.9 using a bilinear interpolation method. For each wave spectrum F_k^n a simulated cross spectrum Φ_k^n is calculated according to eq. 4.25. As the transform is defined on a cartesian grid the spectrum F_k is transformed accordingly using a bilinear interpolation method. The simulated cross spectrum Φ_k^{n+1} of the next iteration step can then be written as

$$\begin{aligned} \Phi_k^{n+1} \approx & \alpha_1^n e^{-k_x^2 \alpha_2^n} \Phi_k^n + \alpha_1^n e^{-k_x^2 \alpha_2^n} \sum_{k'} \frac{\partial \Phi_k}{\partial F_{k'}} \Delta F_{k'}^n + e^{-k_x^2 \alpha_2^n} \Phi_k^n \Delta \alpha_1 \\ & - \alpha_1^n k_x^2 e^{-k_x^2 \alpha_2^n} \Phi_k^n \Delta \alpha_2 . \end{aligned} \quad (9.23)$$

Based on the above approximations, the following cost function has to be minimised

in each iteration step:

$$\begin{aligned}
 J(\Delta \mathbf{X}) = & \sum_k \frac{\text{Re}[e^{-k_x^2 \alpha_2} (\alpha_1^n + \Delta \alpha_1 - \alpha_1 k_x^2 \Delta \alpha_2) \Phi_k^n + \sum_i^{4n_p} Z_k^i \Delta \mathbf{X}_i - \Phi_k^{obs}]^2}{(\sigma_k^{\text{Re}\Phi})^2} \\
 & \sum_k \frac{\text{Im}[e^{-k_x^2 \alpha_2} (\alpha_1^n + \Delta \alpha_1 - \alpha_1 k_x^2 \Delta \alpha_2) \Phi_k^n + \sum_i^{4n_p} Z_k^i \Delta \mathbf{X}_i - \Phi_k^{obs}]^2}{(\sigma_k^{\text{Im}\Phi})^2} \\
 & + \sum_i^{4n_p+2} \frac{(\mathbf{X}_i^n + \Delta \mathbf{X}_i - \mathbf{X}_i^a)^2}{\sigma_i^2}
 \end{aligned} \tag{9.24}$$

with complex valued functions Z defined as

$$Z_k^i = e^{-k_x^2 \alpha_2} \alpha_1^n \sum_{k'} \frac{\partial \Phi_k}{\partial F_{k'}} \frac{\partial F_{k'}}{\partial X_i} \quad i = 1, \dots, 4n_p \tag{9.25}$$

Eq. 9.24 represents a quadratic minimisation problem with respect to the unknown vector $\Delta \mathbf{X}$. To simplify the further discussion, the equation is rewritten in matrix notation as

$$\begin{aligned}
 J(\Delta \mathbf{X}) = & (\Phi^{obs} - \Phi^n - D^n \Delta \mathbf{X})^T S_\epsilon^{-1} (\Phi^{obs} - \Phi^n - D^n \Delta \mathbf{X}) \\
 & + (\Delta \mathbf{X} + \mathbf{X}^n - \mathbf{X}^a)^T S_a^{-1} (\Delta \mathbf{X} + \mathbf{X}^n - \mathbf{X}^a)
 \end{aligned} \tag{9.26}$$

with Jacobian matrix D^n of dimension $2N \times N_X$ given by

$$D^n = \begin{pmatrix} \text{Re } Z_{k_1}^1 & \cdots & \text{Re } Z_{k_1}^{4n_p} & \text{Re } A_{k_1} & \text{Re } B_{k_1} \\ \vdots & \vdots & \vdots & \vdots & \vdots \\ \text{Re } Z_{k_N}^1 & \cdots & \text{Re } Z_{k_N}^{4n_p} & \text{Re } A_{k_N} & \text{Re } B_{k_N} \\ \text{Im } Z_{k_1}^1 & \cdots & \text{Im } Z_{k_1}^{4n_p} & \text{Im } A_{k_1} & \text{Im } B_{k_1} \\ \vdots & \vdots & \vdots & \vdots & \vdots \\ \text{Im } Z_{k_N}^1 & \cdots & \text{Im } Z_{k_N}^{4n_p} & \text{Im } A_{k_N} & \text{Im } B_{k_N} \end{pmatrix} \tag{9.27}$$

where $N = n_\Phi n_k$ is the dimension of the polar grid and $N_X := 4n_p + 2$ is the dimension of the unknown parameter vector. The wavenumbers k_1, \dots, k_N define an arbitrary ordering of the bins of the polar grid. The functions A_k, B_k are defined as

$$\begin{aligned}
 A_k &= e^{-k_x^2 \alpha_2} \Phi_k^n \\
 B_k &= -\alpha_1^n k_x^2 e^{-k_x^2 \alpha_2} \Phi_k^n
 \end{aligned} \tag{9.28}$$

and the error covariance matrix S_ϵ of dimension $2N \times 2N$ is given by

$$S_\epsilon = \begin{pmatrix} \sigma_{k_1}^{\text{Re}\Phi} & 0 & 0 & 0 & 0 & 0 \\ 0 & \ddots & 0 & 0 & 0 & 0 \\ 0 & 0 & \sigma_{k_N}^{\text{Re}\Phi} & 0 & 0 & 0 \\ 0 & 0 & 0 & \sigma_{k_1}^{\text{Im}\Phi} & 0 & 0 \\ 0 & 0 & 0 & 0 & \ddots & 0 \\ 0 & 0 & 0 & 0 & 0 & \sigma_{k_N}^{\text{Im}\Phi} \end{pmatrix}. \tag{9.29}$$

Finally, the prior covariance matrix S_a of dimension $N_X \times N_X$ is defined as

$$S_a = \begin{pmatrix} (\sigma_1)^2 & 0 & 0 \\ 0 & \ddots & 0 \\ 0 & 0 & (\sigma_{4n_p+2})^2 \end{pmatrix} . \quad (9.30)$$

Using the matrix notation eq. 9.26 of the quadratic minimisation problem, it can be shown [Rodgers, 2001] (compare Appendix B) that the next iterate \mathbf{X}^{n+1} following from eq. 9.24 can be written as

$$\begin{aligned} \mathbf{X}^{n+1} &= \mathbf{X}^n + C_X \left((D^n)^T S_\epsilon^{-1} (\Phi^{obs} - \Phi^{sim}) - S_a^{-1} (\mathbf{X}^n - \mathbf{X}^a) \right) \\ &= \mathbf{X}^a + C_X (D^n)^T S_\epsilon^{-1} \left(\Phi^{obs} - \Phi^{sim} + D^n (\mathbf{X}^n - \mathbf{X}^a) \right) , \end{aligned} \quad (9.31)$$

where C_X is the estimated covariance matrix of \mathbf{X} at the n th iteration step given by the following expression:

$$C_X = ((D^n)^T S_\epsilon^{-1} D^n + S_a^{-1})^{-1} \quad (9.32)$$

To improve the convergence of the iteration scheme given by eq. 9.31 in case of strong nonlinearities, a Levenberg Marquard approach is used. The idea is to blend the search direction given by the solution of the quadratic minimisation problem, which might not reduce the cost function of the nonlinear problem in some cases, with the steepest descent direction [Rodgers, 2001]. The resulting scheme is given by

$$\begin{aligned} \mathbf{X}^{n+1} &= \mathbf{X}^n + (C_X^{-1} + \lambda^n I_{N_X})^{-1} \\ &\quad \left((D^n)^T S_\epsilon^{-1} (\Phi^{obs} - \Phi^{sim}) - S_a^{-1} (\mathbf{X}^n - \mathbf{X}^a) \right) \end{aligned} \quad (9.33)$$

where I_{N_X} is the identity matrix of dimension N_X and the parameter λ^n is adjusted during the iteration depending on the cost function values. In the PARSA scheme the strategy

$$\lambda^{n+1} = \begin{cases} 0.25 \lambda^n & : J(\mathbf{X}^n) < J(\mathbf{X}^{n-1}) \\ 4 \lambda^n & : J(\mathbf{X}^n) \geq J(\mathbf{X}^{n-1}) \end{cases} \quad (9.34)$$

turned out to be efficient.

9.3.2 Termination Criteria

One important aspect of the numerical inversion scheme is the criterium used to terminate the iteration. For the PARSA scheme an approach proposed in [Rodgers, 2001] is used. Let the exact solution be denoted by \mathbf{X}^s . Because of the quadratic convergence of the inverse Hessian method one has

$$|\mathbf{X}^n - \mathbf{X}^{n-1}| \geq |\mathbf{X}^n - \mathbf{X}^s| |1 - |\mathbf{X}^n - \mathbf{X}^s|| , \quad (9.35)$$

and thus the difference of the solutions in the steps n and $n + 1$ is a reasonable approximation of the error $|\mathbf{X}^n - \mathbf{X}^s|$ at stage n . A straightforward termination criterion then follows from the requirement that the estimated error should be an

order of magnitude smaller than the expected error as given by the prior distribution. This condition can be written as [Rodgers, 2001]

$$(\mathbf{X}^n - \mathbf{X}^{n-1})^T C_X^{-1} (\mathbf{X}^n - \mathbf{X}^{n-1}) \ll 4n_p + 1 \quad . \quad (9.36)$$

The exact value for the termination threshold is necessarily a compromise between accuracy and computational effort. For the retrievals shown in this study the value $(4n_p + 1)/15$ turned out to be reasonable choice.

9.4 Test of retrieval using synthetic data

In a first step the PARSA scheme was tested using synthetic data, i.e. the observation was simulated from a known ocean wave spectrum. The same ocean wave spectrum was then transformed in different ways and used as a prior information for the retrieval. The ERS-2 SAR imaging parameters for wave mode as summarised in table 5.3 are used for the tests. A necessary requirement for the retrieval performance is the ability of the scheme to reproduce the original wave spectrum. At the same time the scheme should avoid very strong corrections of the prior wave spectrum, which would lead to dynamical inconsistencies in a later assimilation of the retrieved spectra.

Fig. 9.5 shows a retrieval example with a single wind sea system. A parametric JONSWAP spectrum (fully developed) was taken as a prior spectrum (lower right). The respective simulation of the real and imaginary part of the cross spectrum is shown on the bottom left. The observation to be used for the retrieval was simulated by transforming the prior spectrum with the parameters

$$(X_E, X_k, X_\Phi, X_{\Delta\Phi}) = (1.3, 1.1, 25^\circ, 1.2) \quad (9.37)$$

yielding the test spectrum F^{test} shown on the centre right, and subsequent application of the full non-linear cross spectra transform (eq. 4.25). The resulting real and imaginary parts of the observation are shown on the centre left of Fig. 9.5. Applying the PARSA scheme to the synthetic input data gave a retrieved wave spectrum F^{retr} (upper right) and imaging parameters α_1, α_2 after $N_{iterate} = 9$ iteration steps using the termination criterium described above. The respective simulated cross spectrum Φ^{retr} (upper left) was calculated using the retrieved wave spectrum as input to the transform eq. 4.25 and subsequent correction of the energy level and cut-off wavelength according to

$$\Phi^{retr} = \alpha_1 \exp[-k_x^2 \alpha_2] \Phi_k^{sim} \quad . \quad (9.38)$$

As one can see, the simulated cross spectrum Φ^{retr} shows almost perfect agreement with the observation Φ^{obs} . This is the case, although the parameters used to simulate the observation are not exactly reproduced as can be seen from the table given at the bottom of Fig. 9.5. The small deviations become also visible comparing the retrieved wave spectrum F^{retr} with the test spectrum F^{test} . This behaviour makes sense, because the PARSA scheme is designed such that it tries to explain deviations between the observed and simulated cross spectra by both errors in the wave model and in the SAR imaging model. In the present case the scheme attributes the higher energy level of the observation to an underestimation of the integral transform (eq. 4.25), represented by the parameter $\alpha_1 = 1.04$ and at the same time to an energy

underestimation of the wave model represented by the parameter $X_E = 1.19$. Both the rotation parameter X_Φ and the wavenumber rescaling parameter X_k are reproduced with good accuracy. Furthermore, the correction of the cut-off wavelength in the forward model is about 9 m and thus very small. The directional spreading parameter $X_{\Delta\Phi}$ is slightly lower than the prescribed value. Again this behaviour makes sense, because the retrieval avoids any departure from the prior wave spectrum, which does not lead to an improved agreement between observed and simulated cross spectrum. As the agreement is already perfect with the lower value for $X_{\Delta\Phi}$, there is no reason for stronger corrections of the prior spectrum.

The error statistics of the retrieval can be derived from the covariance matrix defined in eq. 9.32. The following values were obtained for the standard deviations and correlations of the retrieved parameters for the present example:

$$\begin{pmatrix} \text{stdv}X_E & \text{cor}(X_E, X_k) & \text{cor}(X_E, X_\Phi) & \text{cor}(X_E, X_{\Delta\Phi}) \\ \cdot & \text{stdv}X_k & \text{cor}(X_k, X_\Phi) & \text{cor}(X_k, X_{\Delta\Phi}) \\ \cdot & \cdot & \text{stdv}X_\Phi & \text{cor}(X_\Phi, X_{\Delta\Phi}) \\ \cdot & \cdot & \cdot & \text{stdv}X_{\Delta\Phi} \end{pmatrix} = \begin{pmatrix} 0.05 & 0.3 & 0.7 & 0.3 \\ \cdot & 0.004 & 0.3 & -0.1 \\ \cdot & \cdot & 1.8^\circ & -0.1 \\ \cdot & \cdot & \cdot & 0.04 \end{pmatrix}$$

In particular, one can see that the standard deviations of the retrieved parameters are smaller than the respective values of the prior distribution (compare table 9.2). This means that despite the significant errors assumed in the cross spectra estimation and the imaging model, the SAR measurement does add information to the knowledge already provided by the ocean wave model.

Another retrieval example based on synthetic data, which is supposed to demonstrate the benefit of the additional complex information represented by the imaginary part of the cross spectrum is shown in Fig. 9.6. As one can see, the prior spectrum contains two wave systems with almost opposite propagation directions in this case. As in the first example an observation was generated by simulation. In this case the following parameters were used to transform the spectrum

$$(X_E^1, X_k^1, X_\Phi^1, X_{\Delta\Phi}^1, X_E^2, X_k^2, X_\Phi^2, X_{\Delta\Phi}^2) = (1.1, 1.03, -40^\circ, 1, 0.9, 0.97, 40^\circ, 1) \quad (9.39)$$

Here, the first index refers to the wave system at the top and the second index to the wave system at the bottom. The cross spectrum Φ^{prior} simulated from the prior wave spectrum shows good agreement with the observation in the real part, however strong deviations in the imaginary part. It is clear, that if there was no complex information available as in the case of conventional variance spectra, there would be no reason to modify the prior wave spectrum other than small changes in energy and wavelength. However, the retrieved spectrum calculated with the PARSa scheme within $N_{iter}=14$ iteration steps shows that the information in the imaginary part helps to apply more significant corrections, rotating both wave systems correctly by almost 40° . The inversion example demonstrates that, although the overall shape of the wave spectrum is taken from the wave model and thus most ambiguities in wave propagation direction are resolved by prior knowledge, the imaginary part adds valuable information in multi-system cases.

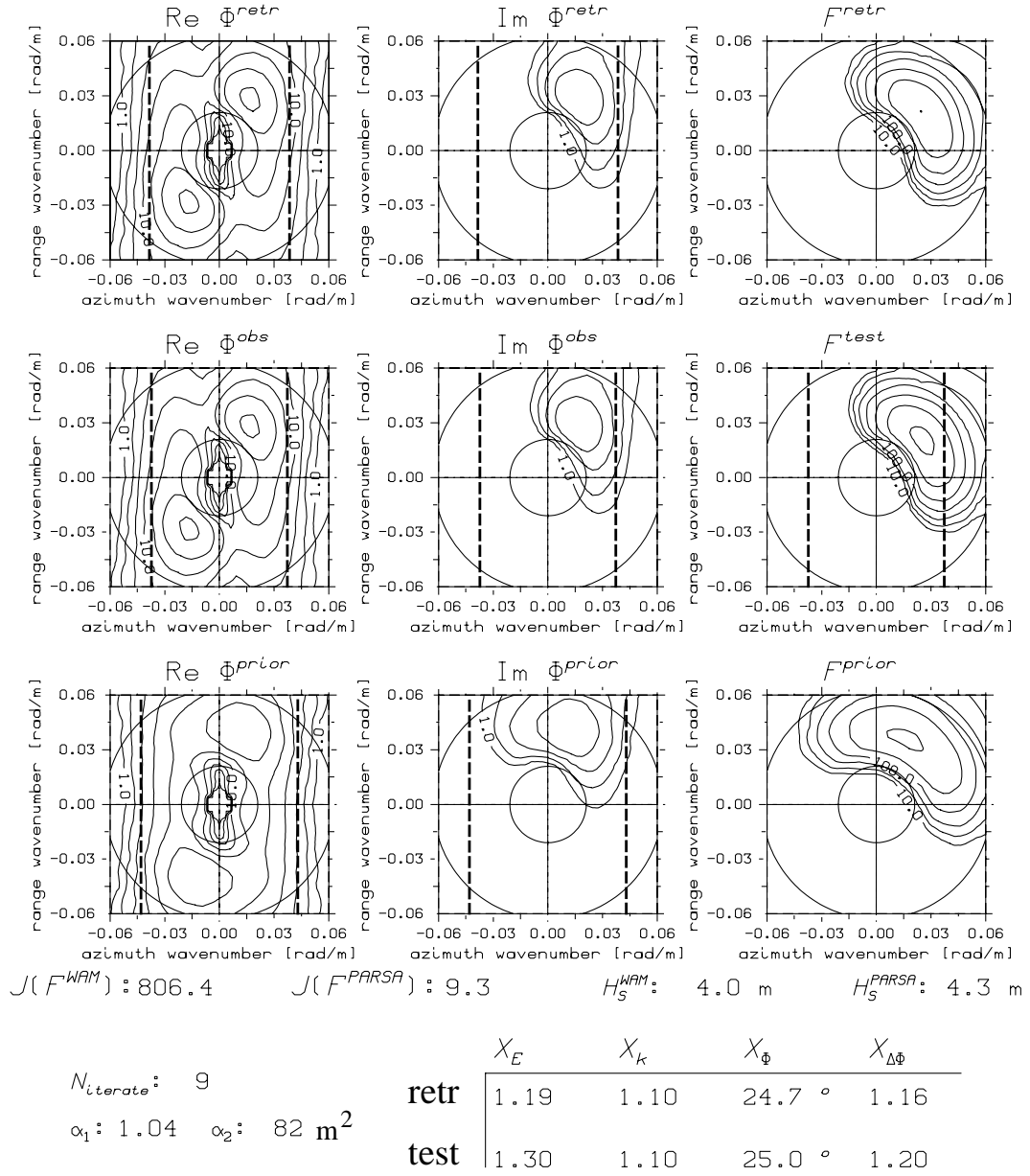
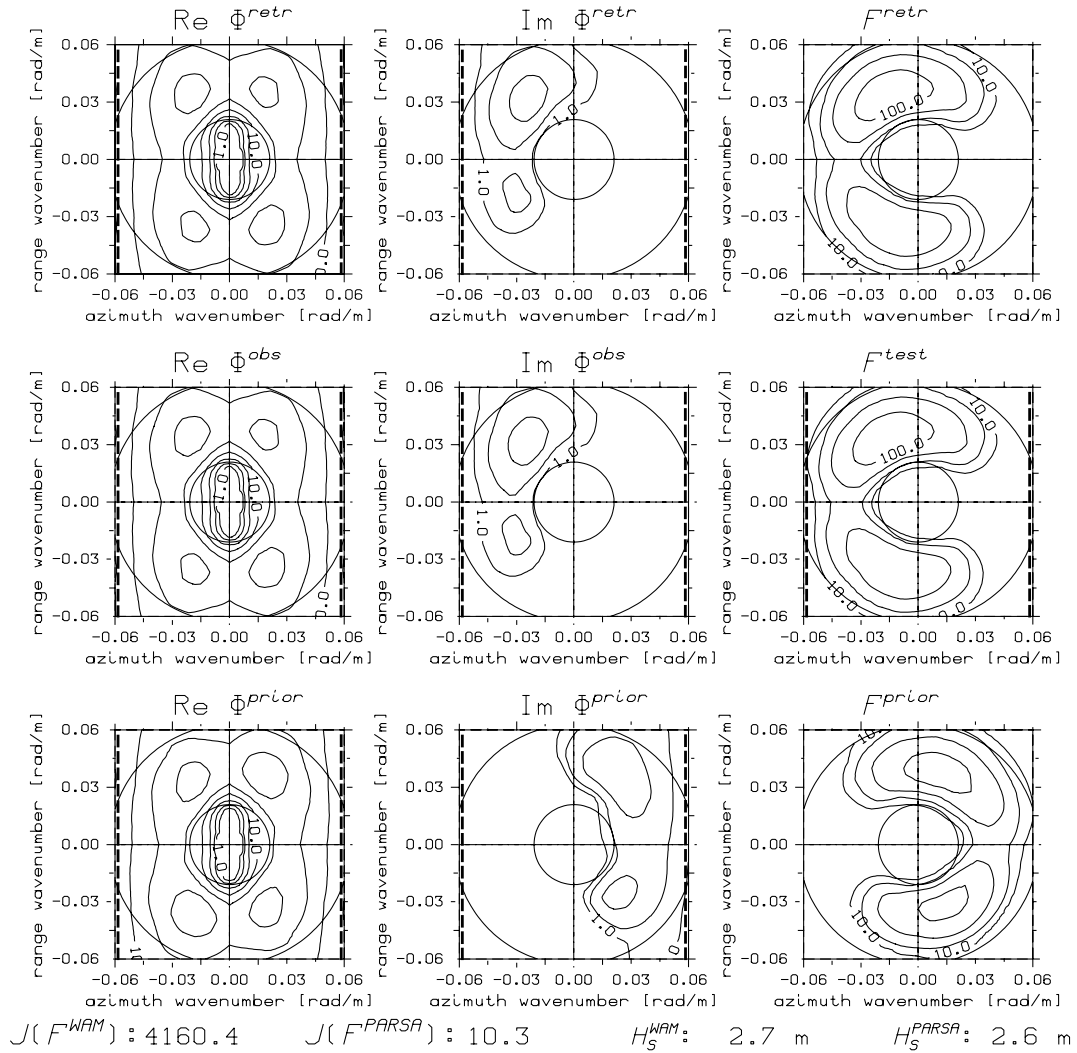


Fig. 9.5: Retrieval example using simulated data with prior spectrum F^{prior} (bottom right), observed cross spectrum Φ^{obs} (centre left), and retrieved wave spectrum F^{retr} . The cross spectra Φ^{prior} and Φ^{retr} simulated from the prior wave spectrum and the retrieved spectrum are shown one the lower left and upper left respectively. The spectrum F^{test} on the centre right was used to simulate the observed cross spectrum (for details see text).



		X_E	X_k	X_Φ	$X_{\Delta\Phi}$
$N_{iterate} : 14$	$\alpha_1 : 1.01$ $\alpha_2 : 12 \text{ m}^2$	1st	1.07	1.03	-38.9° 1.02
		2nd	0.90	0.97	39.6° 0.99
retr	test	1st	1.10	1.03	-40.0° 1.00
		2nd	0.90	0.97	40.0° 1.00

Fig. 9.6: Retrieval example using simulated data with prior spectrum F^{prior} (bottom right), observed cross spectrum Φ^{obs} (centre left), and retrieved wave spectrum F^{retr} . The cross spectra Φ^{prior} and Φ^{retr} simulated from the prior wave spectrum and the retrieved spectrum are shown one the lower left and upper left respectively. The spectrum F^{test} on the centre right was used to simulate the observed cross spectrum (for details see text).

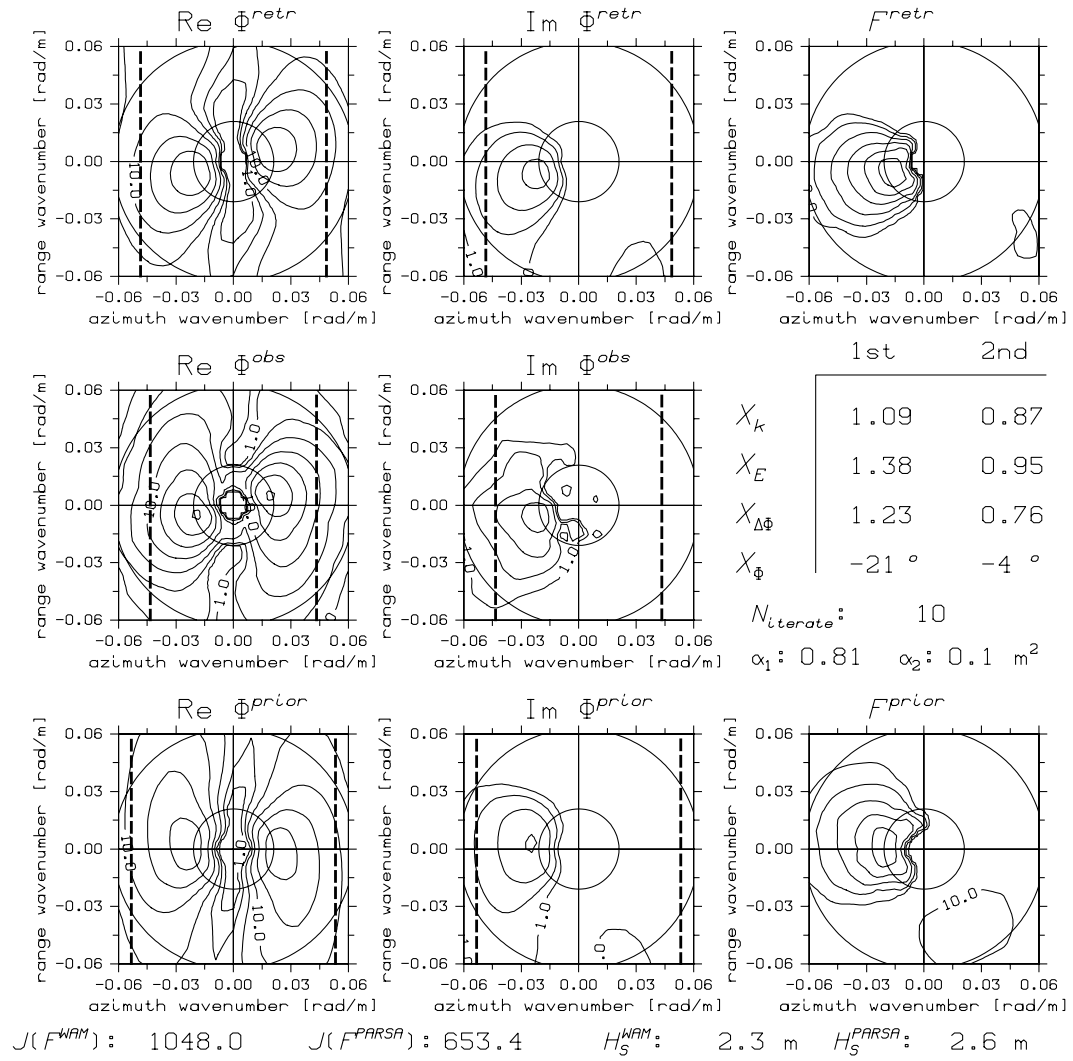


Fig. 9.7: PARSA retrieval for an ERS-2 cross spectrum acquired in the Indian Ocean at 23.46°S 64.36°E on Sep 5, 1996, 5:46 UTC. The satellite heading is 192.94°. The dashed vertical lines indicate the azimuthal cut-off wavelength as defined in Section 7.3.

9.5 Application to reprocessed ERS-2 data

In a second step, the retrieval scheme was applied to the global data set of reprocessed ERS-2 wave mode images introduced in Chapter 5. To make sure that the results are consistent with the retrievals to be carried out with ENVISAT data, the ERS-2 cross spectra were transformed to the standard ENVISAT polar grid as shown in Fig. 5.5.

Figs. 9.7 - 9.8 show two inversion examples calculated with the PARSA scheme. The first case presented in Fig. 9.7 is a swell dominated situation in the Indian Ocean with a wave system of about 300 m wavelength propagating in the azimuth direction and an old wind sea system of about 150 m wavelength in the range direction. The

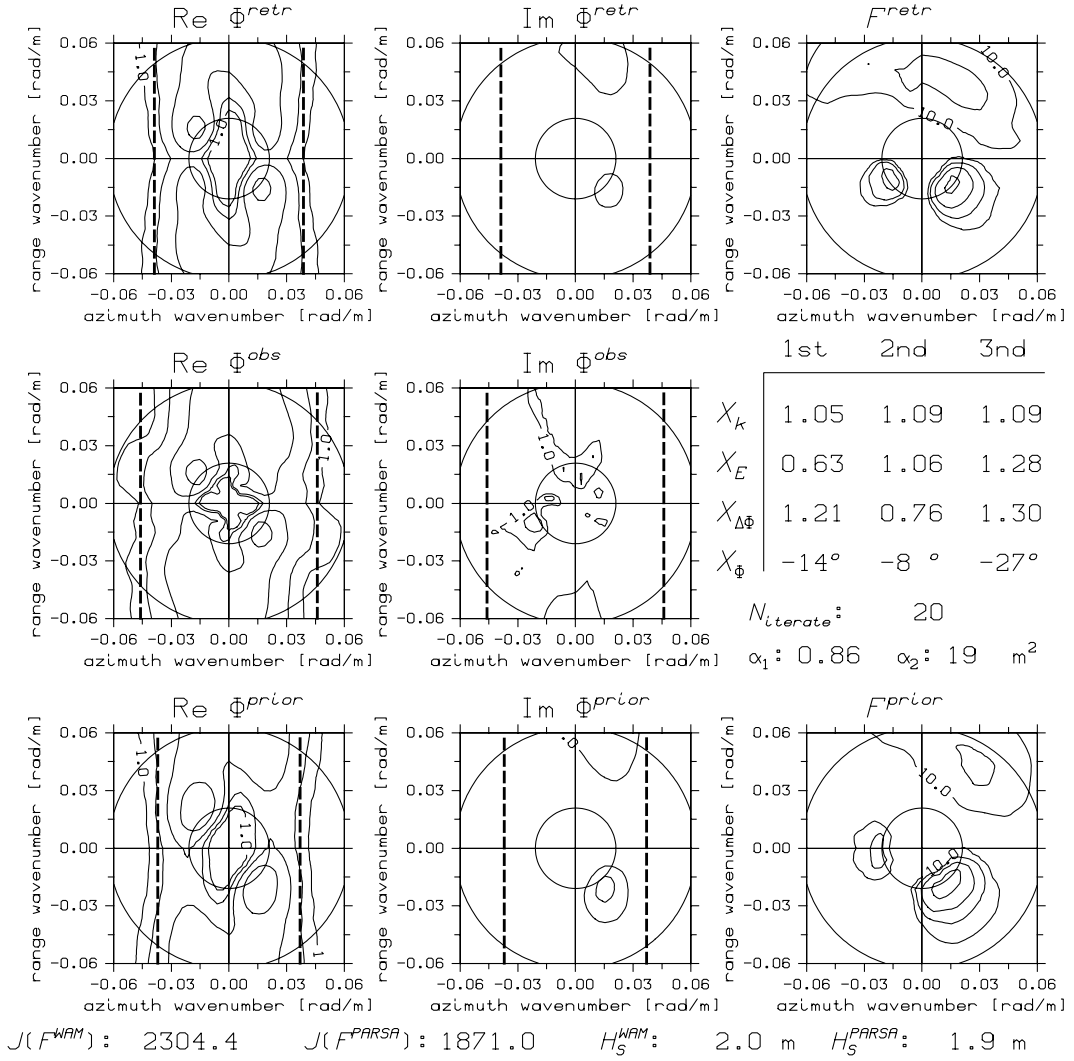


Fig. 9.8: PARSA retrieval for an ERS-2 cross spectrum acquired in the Pacific at 12.46°S 139.45°W on Sep 5, 1996, 8:06 UTC. The heading of the satellite is 347°.

wind speed according to the ECMWF model was 3.2 ms^{-1} explaining the relatively short cut-off wavelength of about 135 m in the observed cross spectrum. The PARSA scheme retrieved the wave spectrum shown on the upper right within 12 iteration steps reducing the cost function value by about 40%. It can be clearly seen that the retrieval scheme improves the agreement between the simulated and the observed cross spectrum including the azimuthal cut-off wavelength. This is mainly achieved by rotating the swell system by about 21° in the anti-clockwise direction. At the same time, the directional spreading is reduced and the wavelength increased to about 330 m. The energy of the swell system is increased by 38%. One can see that the second system is turned in the azimuth direction, scaled down in energy and reduced in wavelength. The rescaling of the two wave system results in a slight increase of the significant wave height from 2.3 m to 2.6 m.

The second retrieval shown in Fig. 9.8 is an example for a more complicated

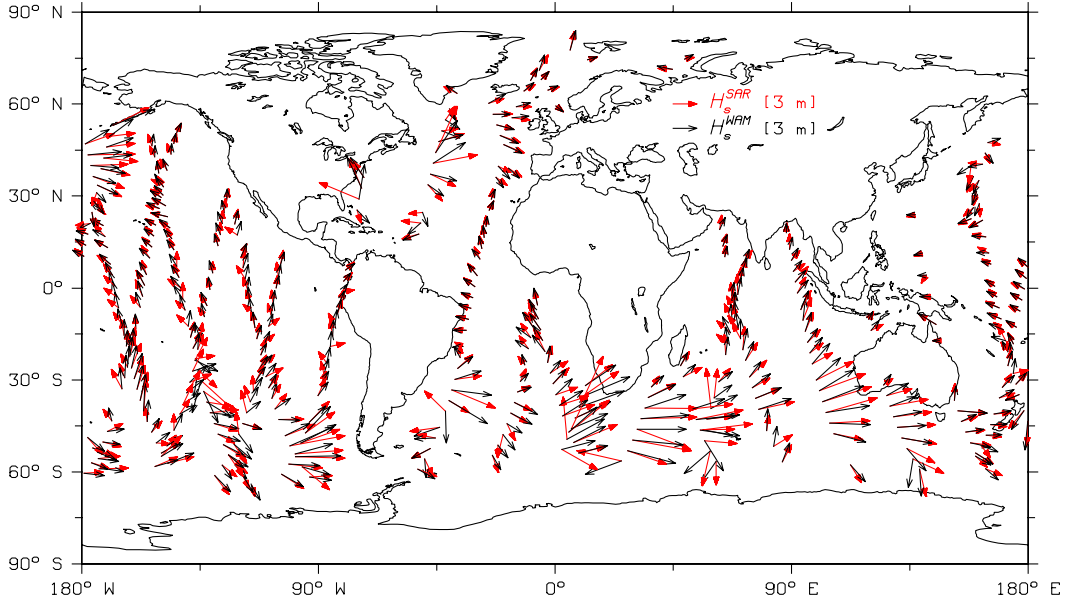


Fig. 9.9: Comparison of significant wave height and mean direction of two-dimensional wave spectra computed with the WAM model (black) and respective PARSA retrievals (red) using ERS-2 cross spectra acquired on Sep 5, 1996.

situation in the Pacific with two swell systems of about 300 m wavelength coming from the south (left system) and the north east (lower right system) and an additional wind sea system with about 150 m wavelength. The PARSA retrieves a wave spectrum after 28 iterations reducing the cost function by about 20%. Again the agreement between simulated and observed cross spectrum is significantly improved by the retrieval. It is interesting to note in this case that the swell system propagating to the left is not visible in the observed real part of the cross spectrum, but shows up in the respective imaginary part. As can be seen this information is taken from the PARSA scheme and used to rotate the prior system in anti-clockwise direction. The example is thus another demonstration, that the complex information provided by the cross spectrum is actually used in the retrieval.

A statistical comparison of prior wave spectra and retrieved spectra was carried out in terms of the significant wave height H_s , the low frequency wave height H_s^{12} (defined analogue to eq. 8.4), as well as the mean wave vector \bar{k}

$$\bar{k} = \frac{1}{16 H_s^2} \int \mathbf{k} F_k d^2 k . \quad (9.40)$$

Fig. 9.9 shows a global map with mean directions and wave heights derived from ECMWF spectra (black arrows) and corresponding PARSA retrievals (red arrows) for ERS-2 wave mode data acquired on Sep 5, 1996. One can see that although the general agreement is good, differences in wave height and direction occur in particular in the areas of high sea states on the Southern hemisphere. For instance, there is a tendency of the retrieval to slightly increase the wave height at high sea states. This observation is consistent with earlier studies [Bentamy *et al.*, 1996], which suggest that the model wind speeds on the southern hemisphere are too weak in many cases.

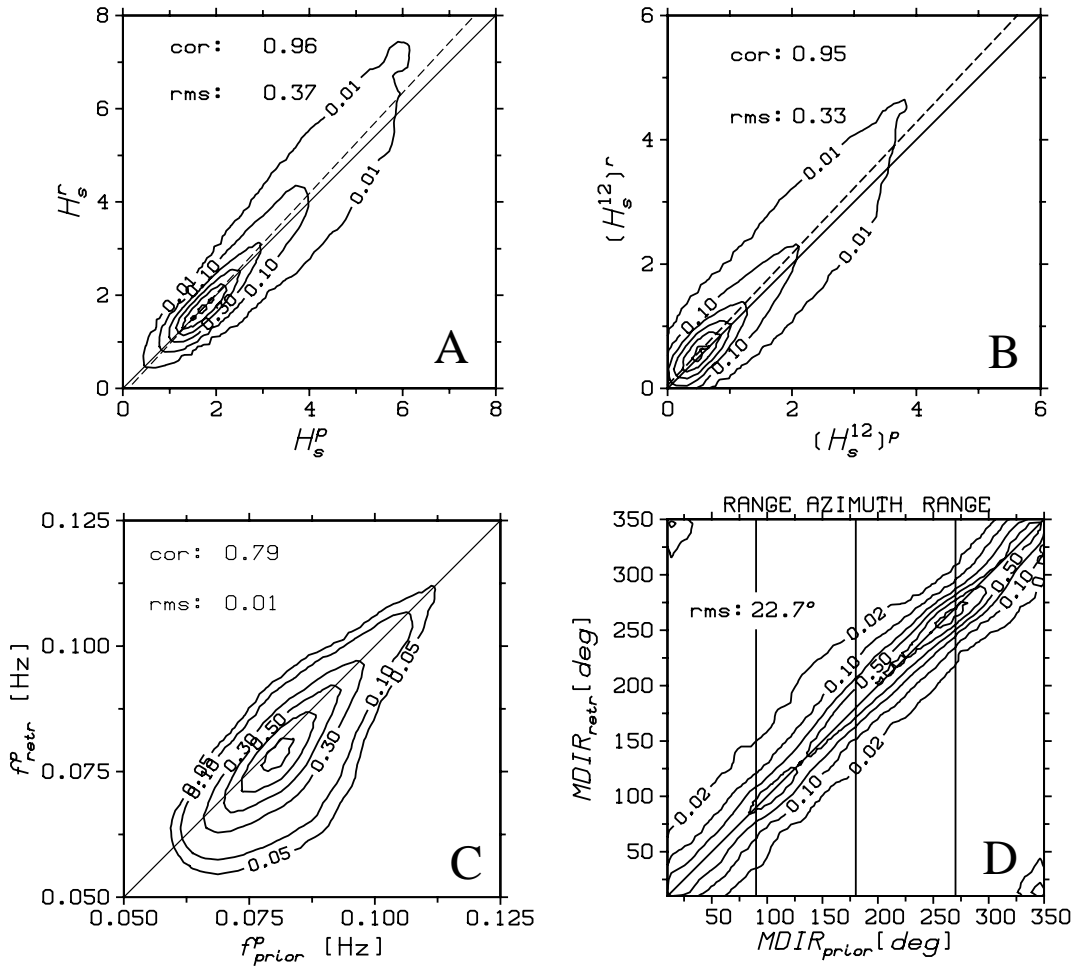


Fig. 9.10: Comparison of integral parameters of ocean wave spectra computed with the WAM model (horizontal axis) and respective PARSA retrievals (vertical axis). (A) Significant wave height. (B) Wave height for periods longer than 12 s. (C) Mean frequency. (D) Mean directions are given in the reference system of the sensor with range and azimuth directions corresponding to 90° and 0° respectively.

It is also interesting to note that the observed corrections of the mean direction look reasonable in the way that the rotations are changing smoothly going from one imagette to the next one along the track. This observation gives some confidence that the corrections are in fact due to large scale errors in the driving wind field. A good example is the North Atlantic where waves of up to 5 m height are seen propagating in easterly direction. These waves were generated by a cyclone, which propagated along the North American east coast (Edward). It can be seen that the retrieval scheme rotates the mean direction in the clockwise direction over a distance of about 1500 km. It can also be seen that the rotation is not always towards the range axis of the sensor as one might suspect due to the velocity bunching effect.

The general findings visible on the global map can be confirmed looking at the respective scatter plots shown in Fig. 9.10. The plots are based on 15000 retrievals, with SAR data acquired in Aug/Sep 1996, i.e. in late Australian winter, with strong

storms in the Southern Atlantic, Pacific and Indian Ocean and a couple of Hurricanes in the North Atlantic.

First of all, one can see that the agreement of model wave height and retrieved wave height shown in Fig. 9.10 (A) is very good with a correlation of 0.96 and a rms of 0.37 m. This high correlation has two main reasons:

- Due to the fact that strong errors in the energy level of the simulated cross spectra are assumed (compare eq. 9.5) the retrieval takes a lot of wave height information from the model.
- Only cases, which failed the inhomogeneity test (compare Section 8.1) were disregarded as input for the retrieval, i.e. the data set contains a significant number of spectra with low signal to noise ratios, in which case the inversion scheme tends to stay close to the prior spectrum.

However, one can see that despite the lack of trust in the simulated energy levels the PARSA scheme still indicates an underprediction of wave heights at high sea states in the order of 0.5 - 1 m for wave heights above 8 m. As pointed out above, this observation is consistent with the general opinion that the driving model wind fields in the “rolling forties” and “fighting fifties” are too low.

The comparison of the mean frequencies in the model and the retrieval shown in Fig. 9.10 (C) indicates an underprediction of wavelength in the wave model in particular for longer waves. This observation again makes sense taking into account the following points:

- The wave height underprediction for the high wind seas discussed above is consistent with a wavelength underprediction, using the general theory on wind sea dynamics introduced in Chapter 2.
- An underprediction of swell wavelength in the model has also been mentioned in *Heimbach* [1998], who attributed the effect to the swell dissipation in the WAM model, which is probably too strong.

The comparison of mean directions shown in Fig. 9.10 (D) exhibits a homogeneous behaviour, i.e. there are no pronounced imaging artefacts or asymmetries visible.

In conclusion one can say, that the PARSA scheme has shown its ability to exploit the information contained in SAR cross spectra, at the same time keeping consistent with the prior wave model spectra. The statistical analysis has shown results, which are consistent with other studies, e.g. on wind fields on the Southern hemisphere.

The scheme is currently tested in more detail using a collocated data set of buoys and ENVISAT ASAR cross spectra, which were collected in the framework of the ENVISAT calibration and validation activities. The data will be used to fine tune the SAR imaging model, which is straightforward, because the parameters α_1, α_2 describing errors in the forward model are part of the PARSA retrieval results. The PARSA scheme will be used at the UK Met Office for the assimilation of ENVISAT ASAR cross spectra into an numerical ocean wave model.

Chapter 10

SUMMARY AND CONCLUSIONS

The thesis has shown both the potential as well as the limitations of different techniques for the retrieval of ocean wave parameters from complex SAR data. The study contains theoretical investigations as well as statistical analysis of data. The different parts will be summarized separately in the following sections.

10.1 Theoretical investigations

The first theoretical aspect discussed was a modification of the existing SAR cross spectra integral transform proposed by *Engen and Johnson* [1995], introducing a nonlinear formulation of the RAR modulation in order to avoid negative radar cross sections occurring in the existing linear model. The presented analysis is the first systematic investigation of this phenomenon. It was shown that for the ERS and ENVISAT configuration the effect is tolerable with less than 10% of meaningless cross sections. However, for future spaceborne systems with higher range resolution of up to 2 m, like TerraSAR, or for airborne SAR the effect becomes significant. For the TerraSAR configuration more than 20% of the predicted cross sections are outside the feasible range, if the linear model is used. To solve the problem, an exponential model for the SAR image intensity was proposed, which predicts positive cross sections under all configurations. The model is consistent with the former linear model in so far as both mean and variance of the RAR image are maintained. Based on the new RAR model, an integral transform was derived, which maps an ocean wave spectrum into the corresponding SAR look cross spectrum. Comparisons with the transform introduced in *Engen and Johnson* [1995] showed that the exponential RAR model leads to changes in the fine structure of the simulated cross spectrum, while overall shape and energy levels are maintained.

The second theoretical part was concerned with a first systematic analysis of the distribution of the phase, as well as the real and the imaginary part, of estimated SAR look cross spectra acquired over the ocean. The study was mainly motivated by the need of noise information in the SAR retrieval of ocean wave spectra. The main results of the investigation are:

- A model was proposed for the distribution of the estimated look cross spectrum, which has the coherence as a key parameter. The model provides pdfs for the phase, magnitude as well as the real and imaginary part of the cross spectrum depending on the amount of smoothing applied in the estimation.
- The coherence was factored into two components with the first one describing

decorrelation due to SAR data noise, which is dominated by speckle, and the second one representing loss of coherence due to the motion of the sea surface.

- The noise model was applied to optimise the look separation time. It was shown that splitting the total bandwidth into two equal parts is a good choice, if the objective is to maximise the signal to noise ratio of the cross spectrum phase.

Combining the existing integral transforms for the SAR image variance spectrum [Hasselmann and Hasselmann, 1991] and the look cross spectrum [Engen and Johnson, 1995], a nonlinear model for the cross spectrum coherence was derived, which predicts the coherence of each spectral bin, given a two-dimensional wave spectrum. It was shown that in the linear approximation, decorrelation is due to waves propagating in opposite directions. In the general nonlinear case loss of coherence is caused by the coupling of wave components with different phase speeds in the SAR image formation process.

10.2 Ocean wave damping by sea ice

Damping of ocean waves travelling into sea ice was studied using spaceborne SAR data acquired over the MIZ. Typical imaging artefacts like spiky wave crests and wave refraction were analysed theoretically. It was shown that the observed effects can be explained by damping of the high frequency part of the ocean wave spectrum. A possible increase of the coherence time of the complex reflectivity within sea ice, was shown to have a minor impact for ERS SAR data.

A simple and robust method based on complex SAR data originally developed for wind speed measurements [Kerbaol *et al.*, 1998] was applied to estimate the orbital velocity variance of the sea surface in the open water as well as in the sea ice. The method has the advantage to be relatively insensitive to the RAR modulation, which is in general not accurately known for sea ice. An azimuthal cut-off wavelength estimated from the SAR look cross-correlation function was related to the orbital velocity variance by regression. A linear model was fitted based on simulation of the azimuthal image auto-correlation function using a global data set of two-dimensional ocean wave model spectra.

The orbital velocity variance was used as a parameter to estimate ocean wave damping. A sensitivity analysis for this parameter was carried out using parametric models for wind sea and swell systems. Simple analytical expressions were derived for the contribution of swell and wind sea to the orbital velocity variance depending on wind speed, swell wave height and wavelength.

The method was applied to ERS SAR scenes acquired over the Weddell and the Greenland Sea. It was shown that the estimated attenuation rates are consistent with measurements obtained in earlier field campaigns in the Greenland and Bering Sea.

In a second step a more sophisticated SAR inversion scheme for the MIZ was presented, which yields estimates for the two-dimensional ocean wave spectrum in front of, and behind the sea ice boundary, as well as a two-dimensional filter function characterising the sea ice impact on the ocean waves. The scheme makes use of first guess information taken from an ocean wave model. It was shown that the method provides results consistent with the cut-off estimation technique.

10.3 Statistical analysis of complex imageries

A global data set of reprocessed ERS-2 wave mode raw data enabled the application of the cross spectrum technique on a statistical basis for the first time. A comparison with two-dimensional wave spectra computed with the WAM model run at the ECMWF showed good agreement of wave propagation directions, except for cases with very low signal to noise ratios. The analysis confirmed the theoretical finding, that the cross spectrum phase noise is increasing with decreasing spectral energy in the respective image variance spectrum.

The distribution of the cross spectrum phase showed a good agreement with the ocean wave phase speeds expected within the linear wave theory. Explanations for the small deviations observed were given.

Apart from the new phase information contained in the cross spectra, the reprocessed data allowed to make use of the full image information, which was not possible with the former standard wave mode product available from ESA. To detect image patterns associated with phenomena like wind rolls, rain cells, biological or anthropogenic surface films or sea ice, which spoil SAR wave measurements, an inhomogeneity test was proposed. The test checks the shift invariance of the image spectrum and is thus able to detect phenomena not associated with ocean waves, as well as strongly inhomogeneous ocean wave fields, which should not be used for wave spectra estimation. It was shown that the majority of inhomogeneous cases occurring in the open ocean is associated with very low wind speeds.

10.4 PARSA wave retrieval scheme

A new scheme for the retrieval of two-dimensional wave spectra from complex SAR data was presented. The partition rescale and shift algorithm (PARSA), which extends the MPI retrieval scheme [Hasselmann *et al.*, 1996], has the SAR cross spectrum and some prior ocean wave spectrum, e.g. taken from a numerical wave model, as input.

The scheme is based on explicit models for measurement errors, uncertainties in the forward model and errors in the prior spectrum. The model for measurement errors is based on the noise analysis performed in the theoretical part. It was shown that in the case of ERS or ENVISAT wave mode data, errors occurring in the estimation of the cross spectrum are relevant mainly for longer swell. To take into account errors in the SAR imaging model, two parameters describing uncertainties in the overall energy level and the cut-off wavelength of the simulated cross spectra were introduced as additional optimisation variables.

The PARSA scheme was tested using synthetic data. The test proved the ability of the method to measure wave spectra under the presence of different error sources, and to provide the respective error statistics of the retrieved parameters. Furthermore, the explicit use of the phase information provided by cross spectra was demonstrated.

The PARSA scheme was applied to a data set of 15000 reprocessed complex ERS-2 cross spectra acquired in August and September 1996. The main conclusions to be drawn from the retrievals are as follows:

- The WAM model tends to have lower wave heights for strong wind seas than

the PARSA retrieval. There is some indication that this observation has to do with a possible underestimation of wind speeds on the southern hemisphere by the numerical model.

- For longer waves the WAM model tends to predict slightly shorter mean wavelength than measured by the PARSA retrieval.
- In particular for spectra with several swell systems like, e.g. frequently observed in the central Pacific, the imaginary part of the cross spectrum helps to resolve ambiguities in the wave propagation direction.

The PARSA scheme has thus shown its ability to make use of the additional information contained in SAR cross spectra, at the same time keeping consistent with the prior wave model spectra. It is therefore regarded as an ideal tool for wave model assimilation using the new ENVISAT ASAR wave mode data.

Chapter 11

OUTLOOK

The investigations and algorithms presented in this thesis have a lot of future applications. This is mainly because complex SAR data are just now becoming available from the ENVISAT satellite on a global and operational basis. The PARSA retrieval scheme will be fine tuned using the ENVISAT calibration and validation data set and will then be used for wave model assimilation at the UK Met office. The theoretical analysis of cross spectra coherence will be used for further optimisations of look separation times and look extraction procedures. The analysis of the cross spectrum coherence will be continued with the objective to extract new information on geophysical processes, like e.g. wind turbulence. The availability of ENVISAT ASAR imageries every 100 km along the track will allow to apply the presented analysis on ocean wave damping by sea ice on a statistical basis.

There are plans to reprocess all 10 years of ERS-2 wave mode raw data to complex imageries, which are fully compatible with the new ENVISAT data. The combined ERS and ENVISAT data set would then allow long term statistics of ocean waves and sea ice contributing to a better understanding of processes related to climate change.

Compared to the ERS satellites the ENVISAT ASAR has several advanced features, which will play an important role in future wind and ocean wave measurements. For example, ASAR is able to operate in dual polarisation mode, i.e. two images with, e.g. VV and HH polarisation, are acquired simultaneously. It has been shown [Engen *et al.*, 2000], that such data can for example be used to obtain information on the modulation transfer functions. An extension of the PARSA scheme for these kind of data is planned.

Another interesting point is the fact that ENVISAT has both radar and optical instruments onboard. It will therefore be possible to use these data in synergy. This is for example helpful for studying phenomena in SAR imagery associated with atmospheric effects or surface films.

It should be noted as well, that other approaches for the use of the new phase information contained in the reprocessed ERS data or the standard ENVISAT data exist, which were not discussed in this study. One approach first introduced in Milman *et al.* [1993] is based on the ambiguity function of the complex image, which tries to provide more detailed information about the space time structure of the wave field than cross spectra. At least for airborne data with integration times of several seconds, the applicability of the method was demonstrated. The availability of complex SAR data on a global scale will certainly be an important driver for the development of more sophisticated techniques for the extraction of sea state parameters from complex data.

Another approach to make more use of the full image information provided by wave mode imagerettes was presented in *Schulz-Stellenfleth and Lehner* [2003]. The idea is to retrieve the two-dimensional ocean wave field, as imaged by the SAR, in the spatial domain. With certain restrictions regarding the nonlinearity of the imaging process, the method enables the analysis of wave parameters like maximum wave height, which are not provided by the standard spectral retrieval methods used so far. The technique has the potential to give new insight in both the SAR ocean wave imaging process as well as ocean wave dynamics, e.g. wave breaking.

Furthermore, it is quite obvious, that the potential of SAR to provide simultaneous information on the wind field and ocean waves has not yet been fully exploited. The analysis of the impact of wind and waves on the gas exchange between atmosphere and ocean is only one example of a possible future application of SAR data.

Chapter 12

APPENDIX

A.1 Distribution of cross spectrum phase and magnitude

The probability density function of the estimated cross spectrum phase

$$\varphi = \text{Arg}(\Phi^{I^1 I^2}) \quad (12.1)$$

calculated by averaging N cross periodograms is given by [Tough et al., 1995]:

$$\begin{aligned} \text{pdf}(\varphi) = & \frac{(1 - |\gamma|^2)^N}{2\pi} \left[\frac{(2N - 2)!}{[(N - 1)!]^2 2^{2(N-1)}} \right. \\ & \cdot \left[\frac{(2N - 1)\beta}{(1 - \beta^2)^{N+0.5}} \left(\frac{\pi}{2} + \arcsin \beta \right) + \frac{1}{(1 - \beta^2)^N} \right] \\ & \left. + \frac{1}{2(N - 1)} \sum_{r=0}^{N-2} \frac{\Gamma(N - 0.5)}{\Gamma(N - 0.5 - r)} \frac{\Gamma(N - 1 - r)}{\Gamma(N - 1)} \frac{1 + (2r + 1)\beta^2}{(1 - \beta^2)^{r+2}} \right] \quad (12.2) \end{aligned}$$

Here, it is assumed that each cross periodogram distributed according to eq. 6.1 and β is defined as

$$\beta = |\gamma| \cos(\varphi - \varphi_0), \quad (12.3)$$

with φ_0 denoting the expectation value of the phase.

The pdf of the cross spectrum magnitude calculated by averaging N periodograms is given by [Tough et al., 1995]:

$$\begin{aligned} \text{pdf}(|\Phi^{I^1 I^2}|) = & \frac{4N(N|\Phi^{I^1 I^2}|)^N}{\langle \Phi^{I^1 I^2} |^2 \rangle^{N+1} (1 - |\gamma|^2) \Gamma(N)} I_0 \left(\frac{2|\gamma|N|\Phi^{I^1 I^2}|}{\langle \Phi^{I^1 I^2} |^2 \rangle (1 - |\gamma|^2)} \right) \\ & K_{N-1} \left(\frac{2N|\Phi^{I^1 I^2}|}{\langle \Phi^{I^1 I^2} |^2 \rangle (1 - |\gamma|^2)} \right), \quad (12.4) \end{aligned}$$

where I_0 and K_{N-1} are modified Bessel functions of the first kind and third kind respectively.

A.2 Posterior distribution in the linear case

Let \mathbf{X} be a Gaussian distributed state vector with mean \mathbf{X}^a and covariance matrix S_a . Furthermore, a measurement vector \mathbf{Y} is given, which is affected by additive zero mean Gaussian noise with covariance matrix S_ϵ . Assuming that the forward model, describing the mapping of a state vector into the respective measurement space, is linear with Jacobian matrix D , the conditional probability density of the state vector \mathbf{X} given the measurement \mathbf{Y} can be written as [Rodgers, 2001]

$$\text{pdf}(\mathbf{X}|\mathbf{Y}) \sim \exp\left[-\frac{1}{2}(\mathbf{X} - \hat{\mathbf{X}})^T C_X^{-1} (\mathbf{X} - \hat{\mathbf{X}})\right], \quad (12.5)$$

with covariance matrix C_X given

$$C_X = \left(D^T S_\epsilon^{-1} D + S_a^{-1}\right)^{-1}, \quad (12.6)$$

and mean state vector calculated as

$$\hat{\mathbf{X}} = C_X (D^T S_\epsilon^{-1} \mathbf{Y} + S_a^{-1} \mathbf{X}^a). \quad (12.7)$$

The expression in eq. 12.5 is referred to as posterior pdf.

B.1 List of Symbols

Symbol	Description	Unit
α	Phillips constant	1
β	Ratio of slant range R and platform velocity V	s
β_f	Frequency modulation rate	Hz s ⁻¹
c	Complex SAR image	(1,1)
c_I	Ice concentration	1
c_L	Speed of light	ms ⁻¹
c_g	Group velocity	ms ⁻¹
c_{ph}	Ocean wave phase speed	ms ⁻¹
f_{dc}	Doppler centroid frequency	Hz
$F_{\mathbf{k}}$	Ocean wave spectrum in 2d wavenumber space	m ⁴
g	Gravitational acceleration	9.81 ms ⁻²
γ	Coherence	1
Δt	Look separation time	s
H_s	Significant wave height	m
I_σ	Calibrated SAR intensity image	1
I	Normalised SAR image intensity	1
I_1, I_2	Normalised looks	1
I_k^1, I_k^2	Complex spectrum of looks I_1, I_2	m
k	Wavenumber	rad m ⁻¹
k_E	Electromagnetic wavenumber	rad m ⁻¹
k_x	Azimuth wavenumber	rad m ⁻¹
k_y	Ground range wavenumber	rad m ⁻¹
k_W	Ocean wavenumber in open water	rad m ⁻¹
k_I	Ocean wavenumber in sea ice	rad m ⁻¹
k_W^\perp	Wavenumber component perpendicular to ice boundary in open water	rad m ⁻¹
k_I^\perp	Wavenumber component perpendicular to ice boundary in sea ice	rad m ⁻¹
L	Length of antenna	m
φ	Phase of cross spectrum	rad
Φ_k^{II}	SAR image variance spectrum	m ²
$\Phi_k^{I^1 I^2}$	Look cross spectrum	m ²
Φ	Angle used for polar grid	rad
$\rho^{I^1 I^2}$	Look cross-correlation function	1
r	Complex radar reflectivity	1
R	Slant range	m
T_0	SAR integration time	s
T^R	Real aperture radar transfer function	m ⁻¹
T^S	SAR transfer function	m ⁻¹
T^u	Orbital velocity transfer function	s ⁻¹
T_W	Wave period	s

Tab. 12.1: List of symbols

Symbol	Description	unit
τ_s	Coherence time	s
η	Sea surface elevation	m
ρ_a	Azimuth resolution	m
ρ_D	Damping rate	m^{-1}
ρ_{sr}	Slant range resolution	m
ρ_r	Range resolution	m
ρ_W	Density of water	kg m^{-3}
ρ_I	Density of ice	kg m^{-3}
σ_0	Normalised radar cross section (NRCS)	1
σ	Radar cross section (NRCS)	1
θ	Incidence angle	rad
u_r	Slant range component of orbital velocity	ms^{-1}
U_{10}	Wind speed in 10 m height	ms^{-1}
V	Platform velocity	ms^{-1}
ξ_H	Inhomogeneity parameter	1
x	Coordinate in azimuth direction	m
x_f	Wind fetch distance	m
x_\perp	Perpendicular distance from ice boundary	m
y	Coordinate in ground range direction	m

Tab. 12.2: List of symbols (continued)

B.2 List of acronyms

Acronym	Description
ASAR	Advanced Synthetic Aperture Radar onboard ENVISAT
BSAR	SAR processor developed at the IMF
ENVISAT	Environmental satellite launched by ESA
ECMWF	European Centre for Medium-Range Weather Forecast
ERS	European Remote Sensing Satellite
ESA	European Space Agency
FFT	Fast Fourier Transform
FM	Frequency modulation
IMF	Remote Sensing Technology Institute
InSAR	Interferometric SAR
JONSWAP	Joint North Sea Wave Project
MIZ	Marginal Ice Zone
MTF	Modulation Transfer Function
NRCS	Normalized Radar Cross Section
pdf	Probability density function
RCS	Radar Cross Section
rms	Root mean square error
RAR	Real Aperture Radar
SAR	Synthetic Aperture Radar
SCAT	Scatterometer
SLC	Single Look Complex SAR image
SRTM	Shuttle Radar Topography Mission
UTC	Universal Time coordinated
WAM	Third generation Wave Model

Tab. 12.3: List of acronyms

Chapter 13

DANKSAGUNG

Die Arbeit wurde am Institut für Methodik der Fernerkundung (IMF) des Deutschen Zentrums für Luft- und Raumfahrt (DLR) angefertigt. Ich bedanke mich bei allen Kollegen, die mir die Arbeit durch das angenehme Arbeitsklima erleichtert haben.

Ich bedanke mich bei Prof. Hasselmann für die Überlassung des Themas und die Betreuung der Arbeit. Weiterhin danke ich Susanne Lehner für die Unterstützung, hilfreiche Ideen und konstruktive Kritik.

Dr. Richard Bamler bin ich für einige erhellende Diskussionen insbesondere zu Fragen der Signalverarbeitung dankbar, sowie für seine Bereitschaft das Zweitgutachten zu schreiben.

Birgitt Schättler und Helko Breit danke ich für das Prozessieren der komplexen ERS-2 Wave-Mode-Daten.

Für ihre Unterstützung bedanke ich mich weiterhin bei den restlichen Mitgliedern der Gruppe "SAR Ozeanographie" (Danielle Hoja, José Carlos Nieto Borge, Anderl Niedermeier, Thomas König, Tobias Schneiderhan), sowie bei Jochen Horstmann und Wolfgang Rosenthal von der GKSS.

Die Arbeit wurde finanziell im Rahmen des Projektes FEME (Fernerkundung Meereis) durch das Bundesministerium für Bildung und Forschung (BMBF) unterstützt. Die ERS-2- Daten wurden von der Europäischen Raumfahrtagentur (ESA) im Rahmen der ERS-AO2-Projekte FEME (A02-D-14/5) und des ERS-AO3-Projektes COMPLEX (ID 999192) zur Verfügung gestellt.

BIBLIOGRAPHY

- Alpers, W., Monte Carlo simulations for studying the relationship between ocean wave and synthetic aperture radar image spectra, *J. Geophys. Res.*, *88*, 1745–1759, 1983.
- Alpers, W. and B. Brümmer, Atmospheric boundary layer rolls observed by the synthetic aperture radar aboard the ERS-1 satellite, *J. Geophys. Res.*, *99*, 12613–12621, 1994.
- Alpers, W. and K. Hasselmann, Spectral signal to clutter and thermal noise properties of ocean wave imaging synthetic aperture radars, *Int. J. Rem. Sens.*, *3*, 423–446, 1982.
- Alpers, W. R. and C. Brüning, On the relative importance of motion-related contributions to the SAR imaging mechanism of ocean surface waves, *IEEE Trans. on Geosci. and Rem. Sens.*, *24*, 873–885, 1986.
- Alpers, W. R., D. B. Ross, and C. L. Rufenach, On the detectability of ocean surface waves by real and synthetic aperture radar, *J. Geophys. Res.*, *86*, 6481–6498, 1981.
- Alpers, W. R. and C. L. Rufenach, The effect of orbital motions on synthetic aperture radar imagery of ocean waves, *IEEE Trans. Antennas Propag.*, *27*, 685–690, 1979.
- Apel, J. R., *Principles of ocean physics*, Academic Press Inc., 1995.
- Bamler, R., PRF-ambiguity resolving by wavelength diversity, *IEEE Trans. Geosci. and Rem. Sens.*, *29*, 997–1001, 1991.
- Bamler, R., Wavelength diversity PRF ambiguity resolver; calibration and test results for ERS-1 SAR, In *Proceedings of the IGARSS'93 conference, Tokyo*, 1993.
- Bamler, R. and P. Hartl, Synthetic aperture radar interferometry, *Inverse Problems*, *14*, R1–R54, 1998.
- Bamler, R. and B. Schättler, *SAR Geocoding: Data and systems*, Chapter SAR data acquisition and image formation, Wichman, 1993.
- Bao, M. and W. Alpers, On the cross spectrum between individual-look synthetic aperture radar images of ocean waves, *IEEE Trans. on Geosci. and Remote Sens.*, *3*, 922 – 932, 1998.
- Bao, M., C. Brüning, and W. Alpers, A generalized nonlinear ocean wave SAR spectral integral transform and its application to ERS-1 SAR ocean wave imaging, In *Proceedings of the Second ERS1 Symp. on Space at the Service of our Environment, Hamburg, ESA SP-361*, 1993.

- Bao, M., C. Brüning, and W. Alpers, Simulation of ocean waves imaging by an along-track interferometric synthetic aperture radar, *IEEE Trans. on Geosci. and Remote Sens.*, *35*, 618–631, 1997.
- Bentamy, A., N. Grima, Y. Quilfen, V. Harscoat, C. Maroni, and S. Pouliquen, An atlas of surface wind from ERS-2 scatterometer measurements 1991-1996, Technical report, IFREMER, France, 1996.
- Bjorgo, E., O. M. Johannessen, and M. W. Miles, Analysis of merged SMMR-SSMI time series of Arctic and Antarctic sea ice parameters 1978–1995, *Geophysical Research letters*, *24*, 413–416, 1997.
- Breit, H., B. Schättler, and U. Steinbrecher, A high precision workstation-based chirp scaling SAR processor, In *Proceedings of the IGARSS97 conference, Singapore*, 1997.
- Breivik, L. A., M. Reistad, H. Schyberg, J. Sunde, H. E. Krogstad, and H. Johnson, Assimilation of ERS SAR wave spectra in an operational wave model, *J. Geophys. Res.*, *103*, 7887–7900, 1998.
- Brüning, C., W. Alpers, and K. Hasselmann, Monte-Carlo simulation studies of the nonlinear imaging of a two dimensional surface wave field by a synthetic aperture radar, *Int. J. Rem. Sens.*, *11*, 1695–1727, 1990.
- Brüning, C., R. Schmidt, and W. Alpers, Estimation of the ocean wave-radar modulation transfer function from synthetic aperture radar imagery, *J. Geophys. Res.*, *99*, 9803–9815, 1994.
- Curlander, J. C., *Synthetic aperture radar: Systems and Signal Processing*, J. Wiley & Sons, New York, 1991.
- Dowd, M. and P. W. Vachon, Ocean wave extraction from RADARSAT Synthetic Aperture Radar Inter-Look Image Cross Spectra, *IEEE TGARS*, *39*, 21–37, 2001.
- Engen, G. and H. Johnson, SAR-ocean wave inversion using image cross spectra, *IEEE Trans. Geosci. Rem. Sens.*, *33*, 1047–1056, 1995.
- Engen, G., P. W. Vachon, H. Johnson, and F. W. Dobson, Retrieval of ocean wave spectra and RAR MTF's from dual-polarization SAR data, *IEEE Trans. Geosci. Rem. Sens.*, *38*, 391–403, 2000.
- Fung, A. K., *Microwave Scattering and Emission Models and their Applications*, Artech House, Inc., 1994.
- Gade, M., W. Alpers, H. Hühnerfuss, H. Masuko, and T. Kobayashi, Imaging of biogenic and antropogenic ocean surface films by the multifrequency/multipolarization SIR-C/X-SAR, *J. Geophys. Res.*, *103*, 18,851–18,866, 1998.
- Gerling, T. W., Partitioning sequences and arrays of directional ocean wave spectra into component wave systems, *J. Atmos. and Oceanic Technology*, *9*, 444–458, 1992.

- Goodman, J. W., *Statistical optics*, John Wiley & Sons, 1985.
- Hartmann, D., M. G., *Global physical climatology*, Academic Press, San Diego, 1994.
- Hasselmann, K., On the non-linear energy transfer in a gravity wave spectrum, part 1. general theory, *J. of Fluid Mechanics*, 12, 481–500, 1962.
- Hasselmann, K., *Basic developments in fluid dynamics*, Vol.2, Chapter Weak-interaction theory of ocean waves, Academic Press Inc, New York, 1968.
- Hasselmann, K., Directional wave spectra observed during JONSWAP, *J. Phys. Oceanography*, 10, 1264–1280, 1973.
- Hasselmann, K. and S. Hasselmann, On the nonlinear mapping of an ocean wave spectrum into a synthetic aperture radar image spectrum, *J. Geophys. Res.*, 96, 10713–10729, 1991.
- Hasselmann, K., R. K. Raney, W. J. Plant, W. Alpers, R. A. Shuchman, D. R. Lyzenga, C. L. Rufenach, and M. J. Tucker, Theory of synthetic aperture radar ocean wave imaging: A MARSEN view, *J. Geophys. Res.*, 90, 4659–4686, 1985.
- Hasselmann, S., C. Brüning, K. Hasselmann, and P. Heimbach, An improved algorithm for the retrieval of ocean wave spectra from synthetic aperture radar image spectra, *J. Geophys. Res.*, 101, 16615–16629, 1996.
- Heimbach, P., *Use of ocean wave spectra retrieved from ERS-1 SAR wave mode data for global wave modelling*, Ph. D. thesis, Universität Hamburg, 1998.
- Heimbach, P., S. Hasselmann, and K. Hasselmann, Statistical analysis and inter-comparison with WAM model data of three years of global ERS-1 SAR wave mode spectral retrievals, *J. Geophys. Res.*, 103, 7931–7977, 1998.
- Honerkamp, J., *Stochastic dynamical systems*, VCH Verlagsgesellschaft mbH, 1993.
- Horstmann, J., S. Lehner, W. Koch, and R. Tonboe, Computation of wind vectors over the ocean using spaceborne synthetic aperture radar, *John Hopkins APL Technical Digest* 21(1), 100–107, 2000.
- Horstmann, J., H. Schiller, J. Schulz-Stellenfleth, and S. Lehner, Global wind speed retrieval from SAR, *IEEE Trans. Geosci. Remote Sens.*, in press, 2003.
- Johannessen, O. M., S. Sandven, K. Kloster, M. Miles, V. Melentyev, and L. Bobylev, A sea ice monitoring system for the northern sea route using ERS-1 SAR data, Technical report, Nansen Environmental and Remote Sensing Center, Tech. Rep. 103, 1995.
- Kasilingam, D. P. and O. H. Shemdin, Models for synthetic aperture radar imaging of the ocean: A comparison, *Journal of Geophys. Res.*, 95, 16263–16276, 1990.
- Kerbaol, V., B. Chapron, and P. W. Vachon, Analysis of ERS-1/2 synthetic aperture radar wave mode images, *J. Geophys. Res.*, 103, 7833–7846, 1998.

- Komen, G. J., L. Cavaleri, M. Donelan, K. Hasselmann, S. Hasselmann, and P. Janssen, *Dynamics and modelling of ocean waves*, Cambridge University Press, 1994.
- Krogstad, H., A simple derivation of Hasselmann's nonlinear ocean-synthetic aperture radar transform, *J. Geophys. Res.*, *97*, 873–885, 1992.
- Krogstad, H., O. Samset, and P. W. Vachon, Generalizations of the nonlinear ocean-SAR transformation and a simplified SAR inversion algorithm, *Atmos. Ocean*, *32*, 61–82, 1994.
- Lehner, S., J. Horstmann, W. Koch, and W. Rosenthal, Mesoscale wind measurements using recalibrated ERS SAR images, *J. Geophys. Res.*, *103*, 7847–7856, 1998.
- Lehner, S., J. Schulz-Stellenfleth, B. Schättler, H. Breit, and J. Horstmann, Wind and wave measurements using complex ERS-2 SAR wave mode data, *IEEE Trans. Geosci. and Rem. Sens.*, *38*, 2246–2257, 2000.
- Liu, A. K., B. Holt, and P. W. Vachon, Wave propagation in the marginal ice zone: Model predictions and comparisons with buoy and synthetic aperture radar, *J. Geophys. Res.*, 4605–4621, 1991a.
- Liu, A. K., P. W. Vachon, and C. Y. Peng, Observation of wave refraction at the ice edge by synthetic aperture radar, *J. Geophys. Res.*, *96*, 4803–4808, 1991b.
- Lyzenga, D. R., Numerical simulation of synthetic aperture radar image spectra for ocean waves, *IEEE Trans. Geosci. and Rem. Sens.*, *24*, 863–872, 1986.
- Lyzenga, D. R., An analytic representation of the synthetic aperture radar image spectrum for ocean waves, *J. Geophys. Res.*, *93*, 13859–13865, 1988.
- Lyzenga, D. R., Unconstrained inversion of waveheight spectra from SAR images, *IEEE Trans. Geosci. and Rem. Sens.*, *40*, 261–270, 2002.
- Lyzenga, D. R., R. A. Shuchman, and J. D. Lyden, SAR imaging of waves in water and ice: evidence for velocity bunching, *J. Geophys. Res.*, *90*, 1031–1036, 1985.
- Mastenbroek, C., *Wind-wave interaction*, Ph. D. thesis, Technische Universiteit Delft, 1996.
- Mastenbroek, C. and C. F. de Valk, A semi-parametric algorithm to retrieve ocean wave spectra from synthetic aperture radar, *J. Geophys. Res.*, *105*, 3497–3516, 2000.
- Melsheimer, C., W. Alpers, and M. Gade, Investigation of multifrequency/multipolarization radar signatures of rain cells over the ocean using SIR-C/X-SAR data, *J. Geophys. Res.*, *103*, 18,851–18,866, 1998.
- Miles, J. W., On the generation of surface waves by shear flows, *J. Fluid Mech.*, *3*, 185–204, 1957.
- Milman, A. S., A. O. Scheffler, and J. R. Bennet, A theory of the synthetic aperture radar images of time dependent scenes, *J. Geophys. Res.*, *98*, 911–925, 1993.

- Mittermayer, J., V. Alberga, S. Buckreu, and S. Rieger, TerraSAR-X: Predicted performance, In *Proceedings of the SPIE 2002 conference, San Jose, USA*, 2002.
- Oliver, C. and S. Quegan, *Understanding Synthetic Aperture Radar Images*, Artech House, 1998.
- Phillips, O. M., On the generation of waves by turbulent wind, *J. Fluid Mech.*, 2, 417–445, 1957.
- Phillips, O. M., *Dynamics of the upper ocean*, Cambridge University Press, 1977.
- Phillips, O. M., Spectral and statistical properties of the equilibrium range in wind-generated gravity waves, *J. Fluid Mech.*, 156, 505–531, 1985.
- Raney, R. K., H. Runge, R. Bamler, I. G. Cumming, and F. H. Wong, Precision SAR processing using chirp scaling, *IEEE Trans. Geosci. and Rem. Sens.*, 32, 786–799, 1994.
- Rodgers, C. D., *Inverse Methods for Atmospheric Sounding: Theory and Practice*, Series on Atmospheric, Oceanic and Planetary Physics, 2001.
- Romeiser, R. and D. R. Thompson, Numerical study on the along-track interferometric radar imaging mechanism of oceanic surface currents, *IEEE Trans. on Geosc. and Rem. Sensing*, 38, 446–458, 2000.
- Schmidt, R., *Bestimmung der Ozeanwellen-Radar-Modulations-Übertragungsfunktion aus der Abbildung des Ozeanwellenfeldes durch flugzeuggetragene Radarsysteme mit synthetischer Apertur*, Ph. D. thesis, Universität Hamburg, 1995.
- Schulz-Stellenfleth, J., J. Horstmann, S. Lehner, and W. Rosenthal, Sea surface imaging with an across track interferometric synthetic aperture radar (InSAR) - the SINEWAVE experiment, *IEEE Trans. Geosci. and Rem. Sens.* 39(9), 2017–2028, 2001.
- Schulz-Stellenfleth, J. and S. Lehner, SAR ocean wave inversion - a hierarchic approach, In *Proceedings of the ERS - ENVISAT symposium, Gothenburg, Sweden*, 2000.
- Schulz-Stellenfleth, J. and S. Lehner, Ocean wave imaging using an airborne single pass cross track interferometric SAR, *IEEE Trans. Geosci. and Rem. Sens.*, 39, 38–44, 2001.
- Schulz-Stellenfleth, J. and S. Lehner, Spaceborne synthetic aperture radar observations of ocean waves travelling into sea ice, *J. Geophys. Res.* 107(C8), 10.1029–10.1039, 2002.
- Schulz-Stellenfleth, J. and S. Lehner, Derivation of two-dimensional sea surface elevation fields from complex synthetic aperture radar data, *submitted to IEEE*, 2003.

- Schulz-Stellenfleth, J., S. Lehner, R. Bamler, and J. Horstmann, A model for ocean wave imaging by a single pass cross track interferometric SAR (InSAR) – the SINEWAVE experiment, In *IGARSS 98, Seattle*, 1998.
- Schulz-Stellenfleth, J., S. Lehner, and D. Hoja, Use of the coherence of synthetic aperture radar look cross spectra for ocean wave measurements, In *Proc. Int. Geosci. Remote Sens. Symp.*, Toronto, Canada, 2002.
- Shuchman, R. A. and C. L. Rufenach, Extraction of marginal ice zone thickness using gravity wave imagery, *J. Geophys. Res.*, *99*, 901–918, 1994.
- Squire, V. A., J. P. Dugan, P. Wadhams, P. J. Rottier, and A. K. Liu, Of ocean waves and sea ice, *Annu. Rev. Fluid Mech.*, *27*, 115–168, 1995.
- Tough, J., D. Blacknell, and S. Quegan, A statistical description of polarimetric and interferometric synthetic aperture radar data, *Proc. R. Soc. Lond. A*, *449*, 567–589, 1995.
- Vachon, P. W., J. Campbell, C. Bjerkelund, F. Dobson, and M. Rey, Ship detection by the RADARSAT SAR: Validation of detection model predictions, *Canadian J. Rem. Sens.*, *23*, 48–59, 1997.
- Vachon, P. W. and H. E. Krogstad, Airborne and spaceborne synthetic aperture radar observations of ocean waves, *Atmosphere-Ocean*, 83–112, 1994.
- Vachon, P. W., R. B. Olsen, H. E. Krogstad, and A. K. Liu, Airborne synthetic aperture radar observations and simulations for waves in ice, *J. Geophys. Res.*, *98*, 16411–16425, 1993.
- Vachon, P. W. and R. K. Raney, Resolution of the ocean wave propagation direction in SAR imagery, *IEEE Trans. on Geosci. and Rem. Sens.*, *29*, 105–112, 1991.
- Valenzuela, G. R., Theories for the interaction of electromagnetic and oceanic waves - a review, *Boundary Layer Metereol.*, *13*, 61–85, 1978.
- Wadhams, P., *Ice in the ocean*, Gordon and Breach Science Publishers, 2000.
- Wadhams, P. and B. Holt, Waves in frazil and pancake ice and their detection in SEASAT synthetic aperture radar imagery, *J. Geophys. Res.*, *96*, 8835–8852, 1991.
- Wadhams, P., V. A. Squire, D. J. Goodman, A. M. Cowan, and S. C. Moore, The attenuation rates of ocean waves in the marginal ice zone, *J. Geophys. Res.*, *93*, 6799–6818, 1988.
- WAMDI Group, The WAM model—a third generation ocean wave prediction model, *J. Phys. Oceanogr.*, 1775–1810, 1988.
- Wong, F. H. and I. G. Cumming, A combined SAR Doppler centroid estimation scheme based upon signal phase, *IEEE Trans. on Geosc. and Rem. Sens.*, *34*, 696–707, 1996.